MONITORING OF ELECTROPORATION OF CARDIAC CELL LINE H9C2

Relatore: Prof. Paolo Sgarbossa

Laureando: Davide Menegazzo
Matricola: 2089753

Correlatore: Prof. Lea Rems

INDEX

TABLE OF ABBREVIATIONS

RTV resting transmembrane voltage

ITV induced transmembrane voltage

IRE Irreversible electroporation

PEF High voltage pulsed electric fields

PFA Pulse field ablation

PVI Pulmonary vein isolation

CHO Chinese hamster ovary cells

ROI Region of interest

DMEM Dulbecco's Modified Eagle's Medium

SOMMARIO

L'elettroporazione è una tecnica fondamentale utilizzata per aumentare transitoriamente la permeabilità della membrana cellulare applicando brevi impulsi elettrici ad alto voltaggio. Questo metodo facilita l'introduzione di varie molecole, compreso il materiale genetico, nelle cellule. Questa tesi studia l'elettroporazione della linea cellulare cardiaca H9C2, con l'obiettivo di migliorare la comprensione e il monitoraggio del processo per potenziali applicazioni nella terapia cardiaca e nella ricerca.

Lo studio inizia con un'esplorazione dettagliata delle strutture cellulari, concentrandosi sulle proprietà elettriche della membrana cellulare e sul suo comportamento in un campo elettrico. Il fenomeno dell'elettroporazione viene definito e contestualizzato nell'ambito del suo sviluppo storico e delle sue applicazioni cliniche, in particolare nell'ablazione del tessuto cardiaco e nella terapia genica.

La fase sperimentale prevede la progettazione e la creazione di elettrodi con la stampa 3D, la selezione di linee cellulari e fluorofori appropriati e l'utilizzo di apparecchiature e software avanzati per l'acquisizione e l'analisi dei dati. La metodologia comprende protocolli per la coltura cellulare, la colorazione e l'acquisizione di immagini, con successiva analisi dell'intensità della fluorescenza e delle caratteristiche di granularità.

I risultati mostrano variazioni nell'intensità media della fluorescenza e nella granulazione tra i campioni esposti a diversi livelli di tensione, fornendo indicazioni sull'efficienza e sugli effetti del processo di elettroporazione.

I risultati mostrano variazioni nell'intensità media della fluorescenza e nella granulazione tra i campioni esposti a diversi livelli di tensione, fornendo indicazioni sull'efficienza e sugli effetti del processo di elettroporazione. I risultati suggeriscono soglie di tensione specifiche che ottimizzano la permeabilità della membrana riducendo al minimo i danni irreversibili.

La tesi si conclude con raccomandazioni per ulteriori esperimenti, tra cui l'uso della microscopia ad alta risoluzione per affinare la comprensione delle dinamiche di elettroporazione nelle cellule cardiache. I risultati contribuiscono al campo più ampio della bioingegneria, offrendo dati preziosi per migliorare i protocolli di elettroporazione e le applicazioni nelle terapie cardiache.

ABSTRACT

Electroporation is a critical technique used to transiently increase cell membrane permeability by applying short, high-voltage electric pulses. This method facilitates the introduction of various molecules, including genetic material, into cells. This thesis investigates the electroporation of the H9c2 cardiac cell line, aiming to enhance the understanding and monitoring of the process for potential applications in cardiac therapy and research.

The thesis begins with a detailed introduction into cellular structures, focusing on the cell membrane's electrical properties and its behavior in an electric field. The phenomenon of electroporation is defined and contextualized within its historical development and clinical applications, particularly in cardiac tissue ablation and gene therapy.

The experimental phase involves designing and creating electrodes using 3D printing, selecting appropriate fluorophore (calcein) for monitoring electroporation, and employing advanced equipment and software for data acquisition and analysis. The methodology includes protocols for cell culture, staining, and image acquisition during exposure to electric pulses using fluorescence microscopy, with subsequent analysis of fluorescence intensity and granularity features.

Results show that electric pulses with 100 µs duration and amplitudes between 200–800 V successfully result in cell membrane electroporation, as demonstrated by the decrease in intracellular calcein fluorescence intensity. As expected, the higher the pulse amplitude, the more profound is the increase in membrane permeability and consequently calcein leakout. Unexpectedly, we observed that the exposure to electric pulses also provokes formation of vesicles, either inside the cells or at the cell membrane, which are observed in fluorescence images as distinct bright spots. These results provide new insights into the electroporation effects that require more investigation on the associated mechanisms.

This thesis concludes with recommendations for further experiments, including the use of super-resolution microscopy to refine the understanding of electroporation dynamics in cardiac cells. The outcomes contribute to the broader field of bioengineering by offering valuable data for better understanding electroporation mechanisms, as well as improving electroporation protocols and applications in cardiac therapies.

CHAPTER 1: INTRODUCTION

1.1. STRUCTURE AND FUNCTION OF A CELL

All living structures are made up of cells, and a cell is the smallest living unit in the human organism. Humans, as well as animals and plants, are composed of eukaryotic cells. There are various types of eukaryotic cells that differ in shape, size, and function performed, but all of them are composed of three main components: a plasma membrane, a cytoplasm, and a nucleus [1]. The plasma membrane, often called the cell membrane, consists of a thin, flexible barrier that separates the inside of the cell from the outside environment and regulates the passage of substances into and out of the cell. Inside, the cell is divided into cytoplasm, where most of the cellular processes and functions are carried out, and the nucleus.

The cytoplasm consists of a gel-like medium cytosol, which is a mixture of macromolecules and ions dissolved in water, and various intracellular organelles. The organelles perform different cellular functions, and most of them are separated from the cytosol by a membrane, which allow the organelles to carry out various chemical reactions and processes in parallel without having any interference with each other. Examples of organelles within a cell are the mitochondria, ribosomes, endoplasmic reticulum, Golgi apparatus, and lysosomes (Figure 1.1).

The nucleus, which is also classified as an organelle, is separated from the cytoplasm by a double membrane and contains deoxyribonucleic acids (DNA) that encode proteins necessary for the cell to function [2].

In general, the internal environment of a cell is called intracellular medium and refers to the cytosol and organelles, while the environment outside the cell is called extracellular medium.
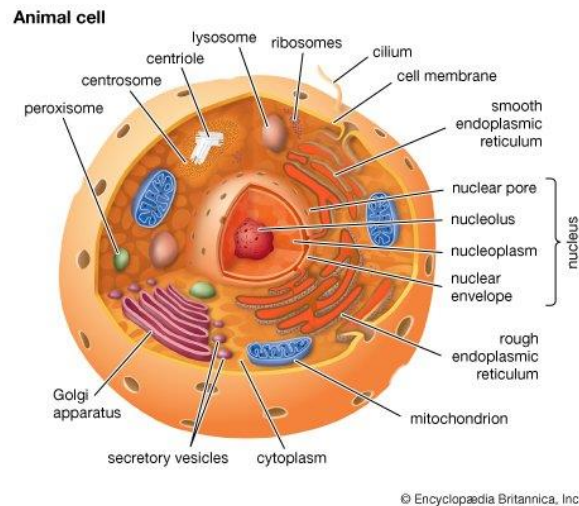
Figure 1.1: The structure of an eukaryotic animal cell [2].

1.1.1. CELL MEMBRANE

The main role of the cell membrane is to separate the inner environment of the cell from the extracellular medium (Figure 1.2). It consists of a phospholipid bilayer (two layers of phospholipid molecules) and other embedded molecules such as cholesterol, glycolipids, proteins, and glycoproteins. Lipid molecules consist of a hydrophilic head (which gives it a polar behavior) and a hydrophobic tail (which gives it a non-polar behavior) [2]. Thus, lipid molecules are amphiphilic. In an aqueous environment, lipids bind in a conformation such that none of the hydrophobic tails are directly exposed to water molecules.

The phospholipid bilayer has a structure that allows it to be completely permeable to small, non-polar molecules such as oxygen (O_2) or carbon dioxide (CO_2), but greatly limits its permeability for small, polar molecules. In fact, small ions, electrically charged molecules and macromolecules practically cannot pass through the lipid bilayer, a condition that allows very efficient and effective control of the passage of substances.

Other molecules in the cell membrane mainly perform structural support functions and functions for transporting substances and communicating with the external environment. Cholesterol, for example, has the function of stiffening the cell membrane.

Proteins inside the cell can be of two types: they can be incorporated into the cell membrane by crossing it (integral proteins) or they can only be found on its surface (peripheral proteins). Integral proteins have the main functions of transport (active transport - pump, passive transport - channel) and of regulating the movement of specific molecules and ions in and out of the cell, while peripheral proteins mainly perform functions of signaling, as they are not permanently embedded in the cell membrane and are easily detached from it [3].
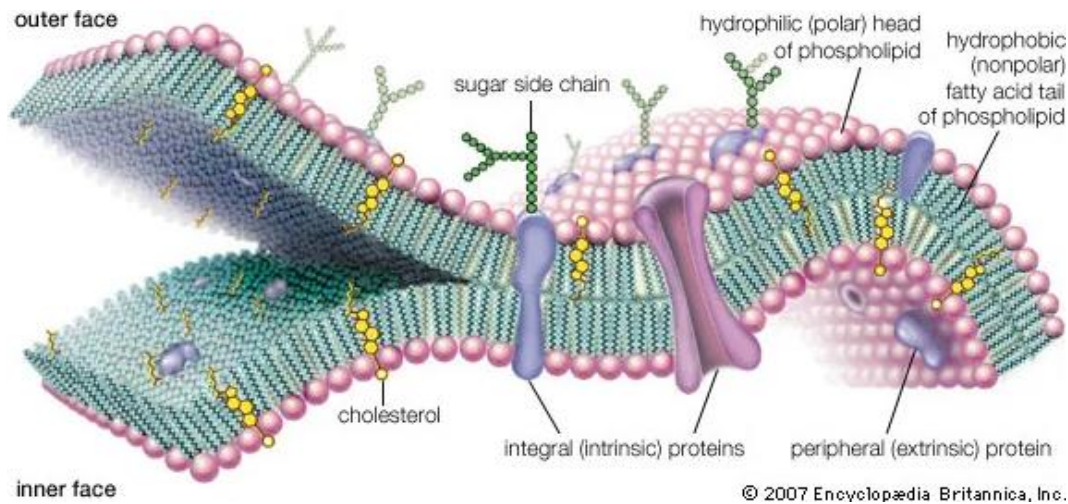
Figure 1.2: Structure of an animal plasma membrane [4].

1.1.2. ELECTRICAL PROPERTIES OF THE CELL MEMBRANE

Electrically, the cell membrane can be regarded as a thin layer with negligible conductivity ($\sim 10^{-7}$ S/m) and low relative dielectric permittivity [5]. In contrast, the intracellular and extracellular medium have much higher conductivity (of the order of 1 S/m), as they contain many ions dissolved in water. Thus, the cell membrane can be represented in simplified form as a thin insulator with a closed surface, surrounded by two conductive media. In other words, the cell behaves electrically as a capacitor, and allows the creation of an excess of electrical charge between the inside and outside of the cell [6].

The ion pumps located in the cell membrane are the fundamental elements that can create a difference in ion concentration between the inside and outside of the cell under physiological conditions. Ion pumps are integral membrane proteins that use metabolic energy to transport ions across the membrane against their electrochemical gradient. The most important ion pump that builds a charge imbalance across the membrane is the sodium/potassium pump, which

transports 3 Na$^+$ ions out of the cells and 2 K$^+$ ions into the cell per one of its transport cycle [7], [8]. As such it creates an excess of negative charge inside the cells and consequently builds a voltage across the membrane. The open potassium channels in the cell membrane additionally enable the leakage of K$^+$ ions along their electrochemical gradient out for the cell and further increase the excess negative charge inside the cell. When the transmembrane potassium flux due to concentration gradient is equal to the opposite electrophoretic flux due to transmembrane voltage, an equilibrium is established. The corresponding equilibrium voltage is called the resting transmembrane voltage ($U_{resting}$). Using a simplification (neglecting the contribution of Cl$^-$ and Ca^{2+} ions), $U_{resting}$ can be estimated from Goldman's equation [9]:

$$U_{resting} = \frac{R \cdot T}{F} \ln \frac{q[Na^+]o + [K^+]o}{q[Na^+]i + [K^+]i}$$

(1)

where R is the gas constant, T is the absolute temperature, F is the Faraday's constant and q represents the ratio of membrane permeability to sodium and potassium. [Na$^+$] and [K$^+$] are the ion concentrations given outside (o-index) and inside (i-index) the cell.

The resting transmembrane voltage is constantly present on the cell membrane and is different depending on the type of cell being considered as well as the phase of the cell cycle [10]. Proliferating cells during division reach around -10 mV, whereas terminally differentiated cells like smooth muscle cells or neurons have a resting transmembrane voltage around -60 mV or -90 mV [11], respectively.
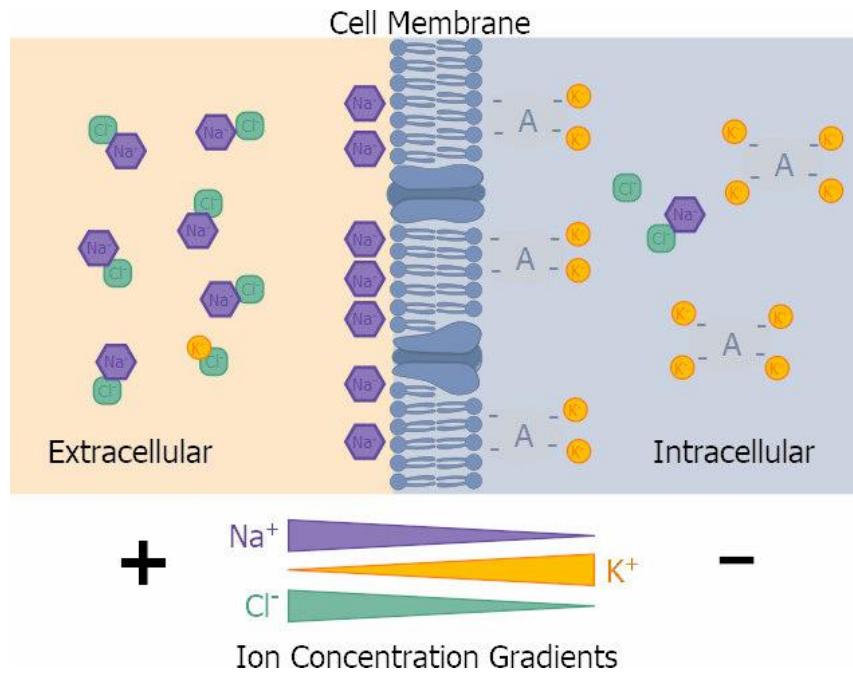
Figure 1.3: Ion concentration gradients across the cell membrane [3].

1.1.3. CELL IN AN ELECTRIC FIELD

If the cell is exposed to an external electric field, forces are exerted on the mobile extracellular and intracellular ions that move them in the direction of the electric field (positively charged ions) or in the opposite direction of the electric field (negatively charged ions). As the ions cannot freely cross the membrane, they concentrate next to it, building an excess charge and consequently increasing the transmembrane voltage. This voltage, which emerges due to the external electric field, is called the induced transmembrane voltage ($U_{induced}$). The steady-state value of $U_{induced}$ for a spherical cell in a homogeneous electric field can be described by Schwan's equation [9], [12]:

$$U_{induced} = \frac{3}{2} \cdot rE \, \cos \varphi$$

(2)

where E is the external electric field strength, r is the radius of the cell and φ is the angle between the direction of the electric field and the outward normal vector at the point of interest on the cell membrane.

Schwan's equation (2) is shown to be valid for a spherical cell, with membrane resistivity much larger than the resistivities of the intracellular and extracellular media, and a membrane thickness much smaller than the radius of the cell itself. In contrast to $U_{resting}$, the $U_{induced}$ is not constant along the entire cell membrane but varies as with cosine function such that its absolute value is the highest in the regions that are closest to the electrodes. In congruence with the capacitive characteristics of the cell membrane, the $U_{induced}$ is not reached immediately, but takes some time to increase and reach its steady-state value. The characteristic and membrane charging time for most cell types under physiological conditions is of the order of 100 ns [9].

For nonspherical cells, the induced transmembrane voltage does not follow a perfect cosine function and it furthermore depends on the orientation of a cell in the electric field. In a study, where experiments on Chinese hamster ovary (CHO) cells were combined with theoretical calculations approximating the cell shape as spheroid, it was shown that the induced transmembrane voltage can be estimated using a generalized Schwan equation [9], [12]:

$$\Delta\phi i = E sin\alpha \frac{1}{1 - L_x} x + E cos\alpha \frac{1}{1 - L_z} z$$

(3)

where L_x and L_z are depolarizing factors that depend on the geometrical properties of the spheroid. The variables x and z are the coordinates of point T on the surface of the spheroid (Figure 1.5a and 1.5c) and E is the strength of the applied electric field. The angle α is the angle between the spheroid's axis of symmetry and the external electric field (Figure 1.5), which defines the orientation of the cell with respect to the electric field.

The transmembrane voltage reaches the highest values when the long axis is parallel to the electric field and the lowest values when the long axis is perpendicular to the electric field.
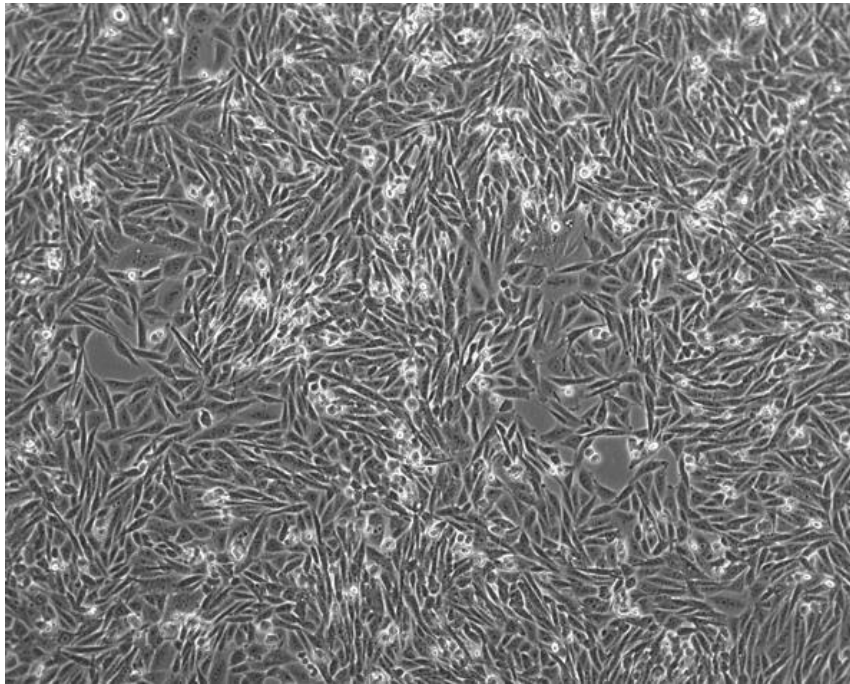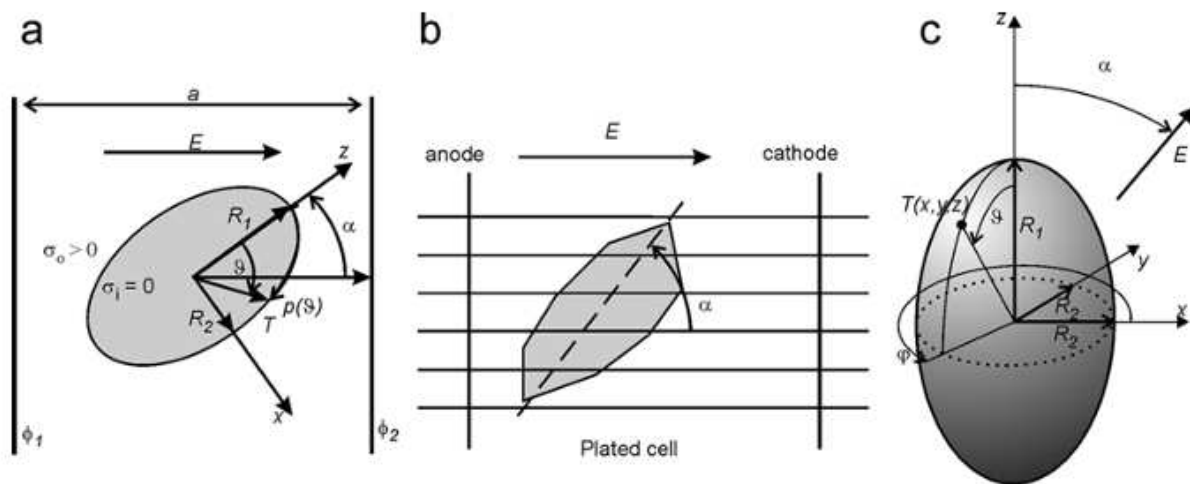

Figure 1.4: Example of a CHO cell line [13].

Figure 1.5: Schematic representation of a spheroid (a) and a CHO plated cell (b) in applied electric field. α is defined as an orientation angle between electric field and symmetry z axis and $p(\theta)$ is the arc of length for a given angle θ. All spheric coordinates are shown in (c)[12].

1.2. ELECTROPORATION

1.2.1 DEFINITION OF ELECTROPORATION

Electroporation, also called electropermeabilization, is a phenomenon that is associated with the transient increase in membrane permeability and is observed when exposing the cell to short high-voltage electrical pulses that induce a transmembrane voltage of at least a few 100 mV. This induced transmembrane voltage promotes creation of transient pores or defects in the membrane that allow substances such as genetic material (DNA and RNA), proteins, drugs, or other molecules to be inserted into the cell. While permeabilization occurs within a few nanoseconds or microseconds of exposure to an electric field (depending on the length and intensity of the electric pulse) [14], membrane permeability slowly returns to baseline values after the exposure ends, which can take several minutes [15].

In situations where cells remain alive after exposure, electroporation is said to be reversible [16]. When cells are exposed to electric pulses of a strength and duration that increase the membrane permeability to such an extent that the cells cannot recover their homeostasis and die, this is described as irreversible electroporation (IRE).
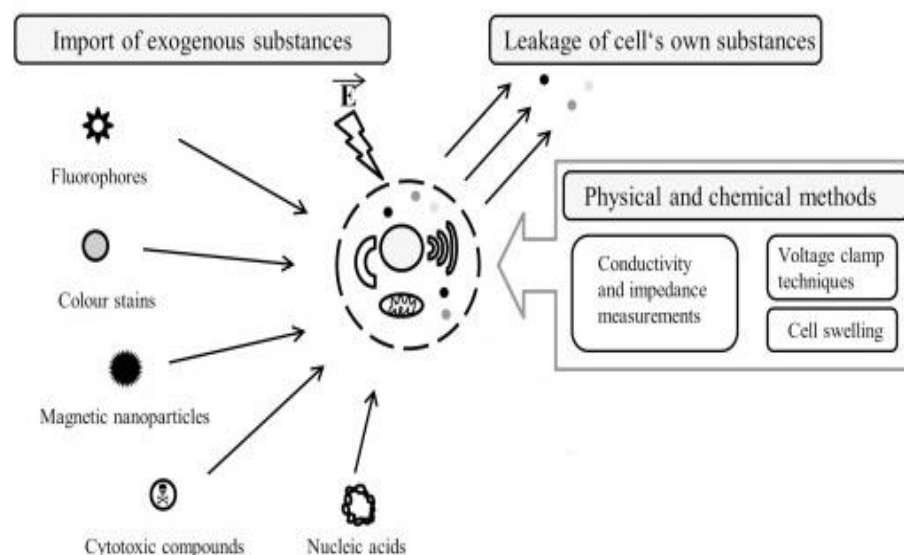

Figure 1.6: Schematic representation of the electropermeabilization mechanism at the single cell level and their way of detection [16].
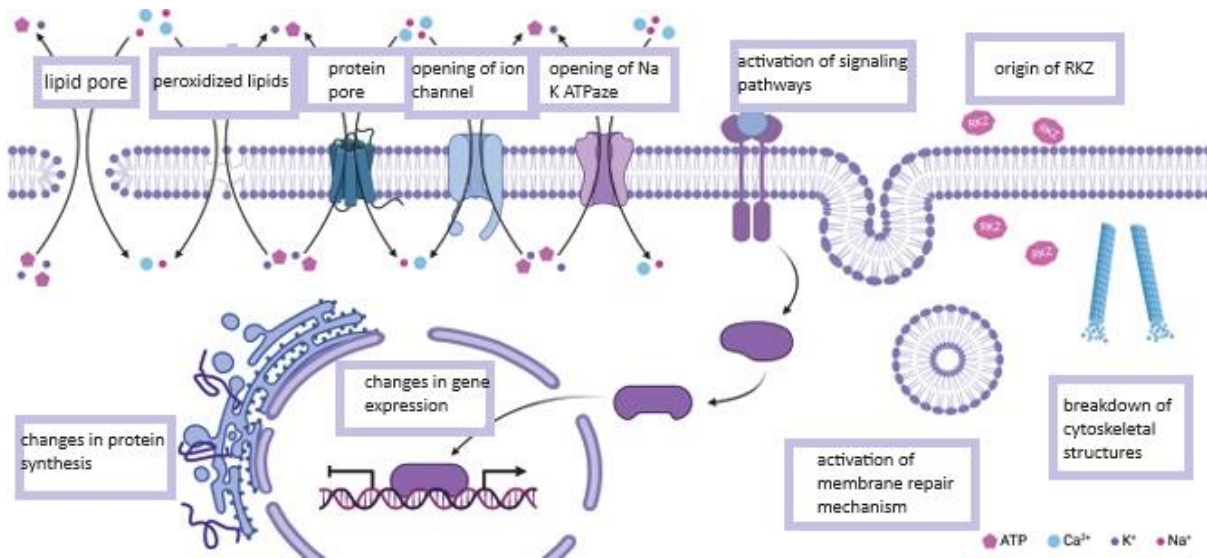
Figure 1.7: Molecular mechanisms participating in electroporation [18].

1.2.2. HISTORY OF ELECTROPORATION

The first studies and observations concerning phenomena resembling electroporation might date back to the mid-1700s; for instance, Jean Antoine Nollet reported the appearance of red spots when subjecting human and animal skin to electric sparks, which might have been partially associated with irreversible electroporation [19]. In the 19th century, there was a considerable growth of interest in the effects that electricity has on biological systems. Experiments using electrical currents that induced contractions and movements in the animal spinal cord were very common at this time [20]. There were also reports on the use of electricity in medicine, including the hemolytic effects of electric pulses [21].

Later in the 1950s and 1960s, researchers including Stämpfli [22], Sale and Hamilton [23], and Zimmermann et al.[24] described the so-called reversible and irreversible electrical breakdown of the membranes of animal, plant, yeast and bacterial cells. In 1982, the increase in membrane permeability caused by exposure to electric pulses was named "electroporation" and was shown to enable transfer of DNA molecules into cells [25].

In the following decades, electroporation became a mainstream technology in the biological sciences and biotechnology for delivery of selected molecules into cells or extraction of valuable compounds from the cells [26].

16

In medicine, electroporation has already been developed for clinical treatment of solid tumors through electrochemotherapy or irreversible electroporation [27] and is being tested for gene therapy and transdermal drug delivery [28], [29].

In recent years, irreversible electroporation, under the name "pulsed field ablation", has shown enormous potential for nonthermal ablation of the cardiac tissue for treatment of cardiac arrhythmias, particularly atrial fibrillation [30].

In addition, reversible electroporation has been proposed as a feasible method for cardiac gene therapy aiming to promote regeneration of the cardiac muscle tissue following myocardial infarction [31]. The following two subsections describe cardiac tissue ablation and gene therapy using electroporation in greater detail.

1.3 CLINICAL APPLICATION OF ELECTROPORATION

1.3.1. CARDIAC TISSUE ABLATION

Atrial fibrillation is the most common arrhythmia in which the heart's upper chambers, called the atria, beat chaotically and irregularly. The cornerstone method for treating atrial fibrillation is pulmonary vein isolation using catheter ablation [32]. This procedure helps isolate atrial fibrillation-sensitive areas located in the pulmonary veins from the rest of the heart. Conventionally, catheter ablation is performed using thermal approaches, either radiofrequency heating or freezing with a cryobaloon. However, this treatment can lead to severe side effects such as pulmonary vein stenosis, phrenic nerve paralysis, esophageal fistulas, and damage to bronchioles [33].

Pulsed field ablation (PFA) emerged as novel nonthermal modality, which is based on irreversible electroporation. PFA uses hundreds to thousands of volts applied to electrodes on a catheter in both monopolar and bipolar modes to induce cell death via electroporation-mediated membrane permeabilization. It has been hypothesized that cardiac cells may be more sensitive to IRE than other cell types such as nerve or smooth muscle cells, and therefore in this case might give fewer side effects (evidence supported by the lack of side effects in preclinical

and clinical studies [34], [35]). For example, a recent preclinical study [36] on PFA reported a significant reduction in the risk of pulmonary vein stenosis in comparison with radiofrequency ablation in a canine model. In this study, radiofrequency ablation resulted in damage to the vagus nerve, esophagus and lung that was not observed with PFA.

In tissue in vivo, irreversible electroporation is inevitable due to nonhomogeneous electric field distribution around the electrodes. Considering that the strength of the electric fields decreases with increasing distance, we can expect the presence of a volume adjacent to the electrodes where the cells will inevitably die. Around the ablated volume, there will be a region of tissue where reversible electroporation will be induced.

Thus, it is important to study not only the irreversible but also the reversible effects of electric pulses on cardiac cells. In addition, since the induced transmembrane voltage depends on the orientation of elongated cells in electric fields, this orientation can play an important role in electroporation of the cardiac tissue, where the orientation of the cardiac muscle cells (cardiomyocytes) varies with location in the heart. To elucidate the effect of cell orientation on electroporation, in vitro studies using cardiomyocytes are of great importance [37].

1.3.2. GENE THERAPY

Gene therapy is based on introducing coding or non-coding nucleic acids (DNA or RNA) into cells with the aim of modifying or regulating gene expression. The nucleic acids must cross the cell membrane and reach the cytoplasm (in case of RNA) or nucleus (in case of DNA) of the target cells, where gene expression or regulation can begin. Due to their size and negative charge, nucleic acids practically do not cross cell membranes spontaneously [28]. For this reason, several methods to transfer nucleic acids across the membrane have been investigated, including viral and non-viral vectors as well as physical approaches.

Viral vectors are based on genetically modified viruses [38], while with non-viral vectors are based on natural or synthetic compounds (e.g. lipid vesicles or synthetic nanoparticles, Figure 1.8) that tend to be less effective but less toxic [39]. Physical methods are based on increasing membrane permeability using external forces, such as mechanical pressure or exposure to an electric field. These physical methods include the introduction of DNA into the tissue by ballistic injection (gene transfer by means of microprojectiles [40]), electroporation [25],

sonoporation (permeabilization of the cell membrane by means of ultrasound [41]) and other methods, which have proven to be effective for localized gene delivery and are simpler than viral and non-viral methods [42].

Electroporation is identified as the most potent nonviral method for nucleic acid delivery into skeletal muscles, tumors, and skin [43], [44], [45]. More than 90 clinical trials use(d) electroporation for nucleic acid delivery in cancer immunotherapies, CAR-T cell engineering, and infectious disease vaccines [46]. Several preclinical studies have provided evidence that electroporation can also be used for intracellular delivery of DNA into cardiac tissue: specifically these studies focused on delivering plasmid DNA molecules coding for vascular endothelial growth factor to promote cardiac revascularization upon myocardial infarction in rat and porcine hearts in vivo [31], [47], [48], [49] [50]. Therefore, studying reversible electroporation of cardiac cells is also interesting for applications of gene therapy.
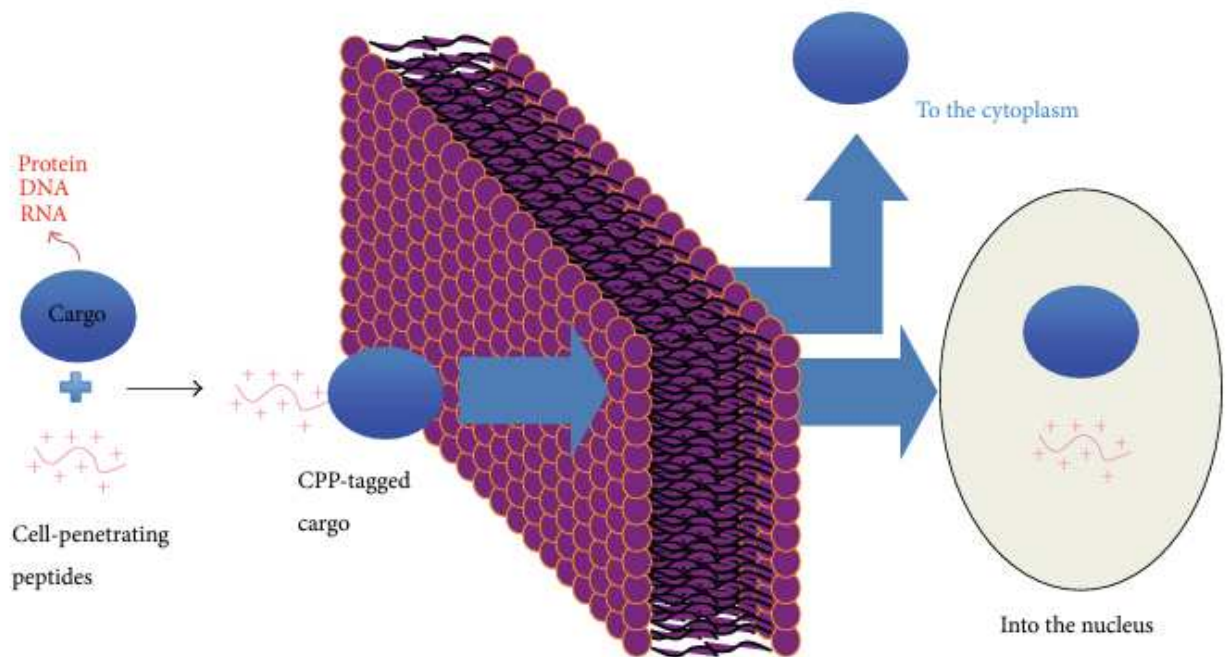

Figure 1.8: Cell-penetrating peptides as non-viral vectors for delivering biologically active molecules [42].

1.4. AIM OF THE THESIS

The objective of this thesis was to investigate the response of the cell line H9c2, derived from rat cardiac muscle tissue to electroporation pulses of different voltages. The study aimed to characterize the electroporation process by monitoring the leak-out of otherwise membrane-impermeable calcein dye from the cells due to electroporation. This was done by acquiring a sequence of fluorescence images using a fluorescence microscope and subsequently analyzing the images by means of a two- and three-dimensional analysis, in order to obtain a complete picture of the cell behavior, both at the macroscopic level and at the level of the individual cell, including the phenomena within the cell.

CHAPTER 2: MATERIALS AND METHODS

This chapter deals with the materials and methodologies used during the days when the experiments were carried out and during the days when the results were extracted and analyzed. The section is divided into four subsections. The first subsection deals with the designing phase, in which all the preliminary investigations concerning the design and creation of the electrodes, the choice of the most suitable cell line and dye to be used are described. The second subsection provides a detailed description of all the equipment and software used for image acquisition, extraction, and analysis. The third subsection describes all the experimental protocols relating to the various stages of the experiments, providing not only a key to understanding but also the possibility of repeating the experiments performed. Finally, the fourth and last subsection briefly illustrates the methodology used for the extraction and analysis of cell features.

2.1. DESIGNING PHASE

2.1.1. NUMERICAL CALCULATIONS USING FINITE ELEMENTS

In the first design phase, the experiment was represented in a digital environment using COMSOL Multiphysics software, performing a finite element analysis of the future experimental configuration. The aim of these calculations was to compute the electric field distribution in the sample between the electrodes and determine the appropriate distance between the electrodes that will enable us to achieve a sufficiently high electric field strength to achieve cell electroporation, keeping in mind the maximum possible voltage and current output of the selected pulse generator.

The geometry of the model consisted of two wire electrodes placed inside a well filled with a liquid medium, as shown in Figures 2.1-2.3. The dimensions of the well corresponded to one well of an Ibidi μ-Plate 96 Well Black, which was selected for experiments. The diameter of the wire electrodes was 0.8 mm and corresponded to platinum/iridium (90/10) wires from which we chose to build the electrodes.

After the geometry was defined, we defined the material properties of the model, specifically the electrical conductivity and relative permittivity of the medium inside the well. The parameters of the model are listed in Table 2.A, as they were entered in the 'Global definitions' section of COMSOL.
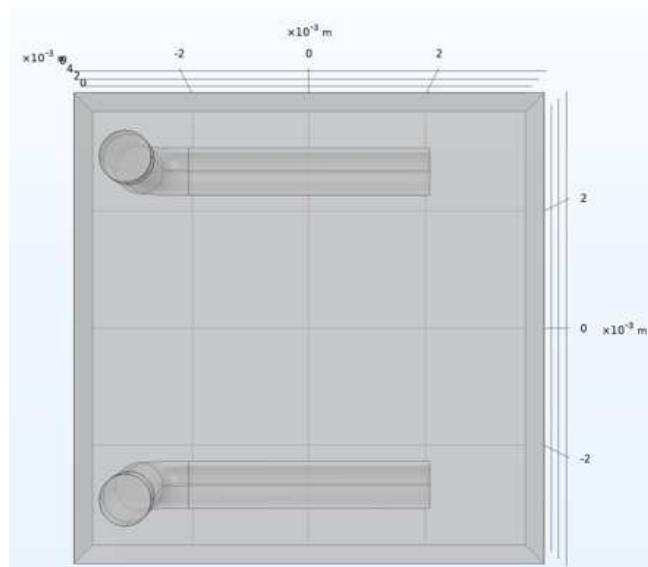
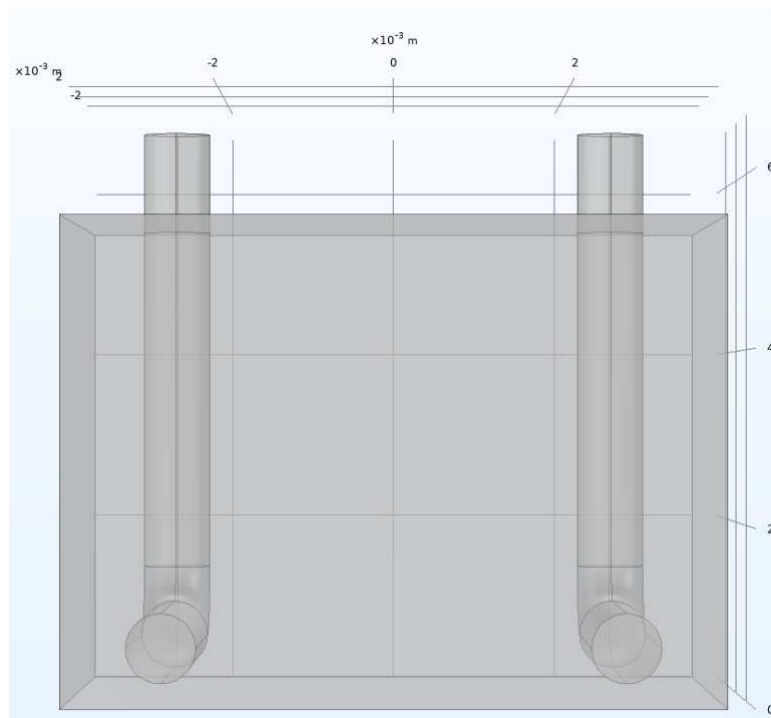

Figure 2.1: Top view of the model geometry (x-y planes).

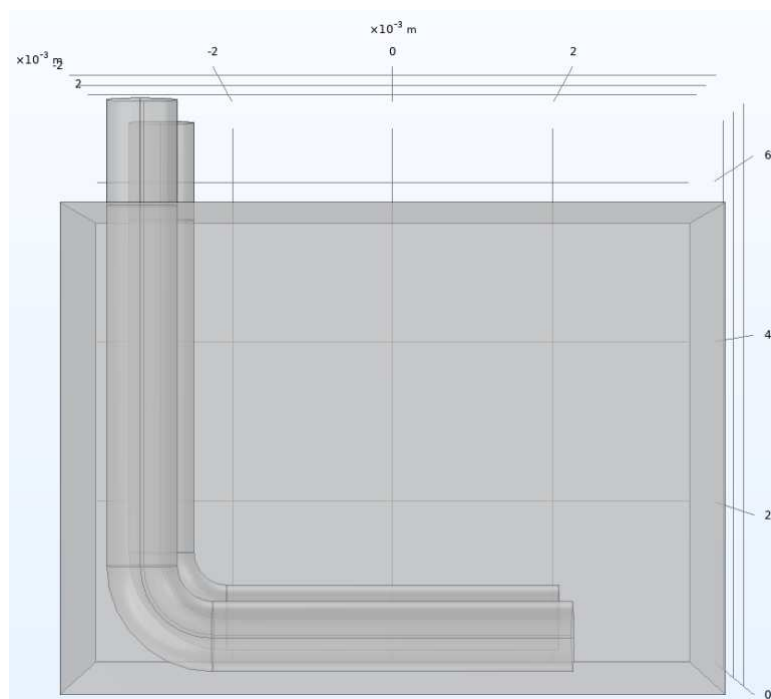**Figure 2.2:** Side view of the model geometry (y-z planes).

Figure 2.3: Side view of the model geometry (x-z planes).

Table 2.A: Parameters used in COMSOL for the virtual analysis of a single well.

Name	Expression/Value	Description
a	7.4 mm	Side 1
b	7.4 mm	Side 2
v	300 µl	Volume of liquid in well
h1	v/(a*b)	Height of the liquid
d	0.8 mm	Electrode diameter
l	0.55*a	Length of the bottom segment of the electrodes
del	4.5 mm	Distance between electrodes
dgap	200 µl	Gap between the bottom of the well and the electrodes
sigma_e	1.5 S/m	Electrical conductivity
epsilon_e	80	Relative permittivity

To compute the electric field distribution in the model, the following steady-state equations were defined in the domain representing the medium using the predefined COMSOL module "Electric Currents":

$$\nabla J = 0$$

(4)

$$J = \sigma E$$

(5)

$$E = -\nabla V$$

(6)

where J is the electric current density, E is the electric field strength, V is the electric potential and σ is the electrical conductivity of the medium.

The boundary conditions were defined as follows: all outside boundaries of the medium within the well were modelled as electrically insulating with the normal component of the electric current density equal to zero, the boundary around one of the electrodes was assigned an electric potential of 1 V, and the boundary around the other electrodes was assigned an electric potential of 0 V. The difference between the electric potentials at the electrodes corresponds to the applied voltage. Since this is a linear time-invariant model, the results can be linearly scaled to any applied voltage.

After defining the model equations, the finite element mesh was defined using the default COMSOL settings.

After launching a steady-state simulation, the following results were obtained: Figure 2.4 shows the distribution of the electric potential, and Figure 2.5 shows the electric field distribution. We can see that the electric field is roughly homogenous in the middle between the electrodes at the bottom of the well, where the cells will be grown. We can further see that the amplitude of the electric field at this location (~250 V/m) is roughly equal to the ratio between the applied voltage (1 V) and the inner distance between the electrodes (4 mm).
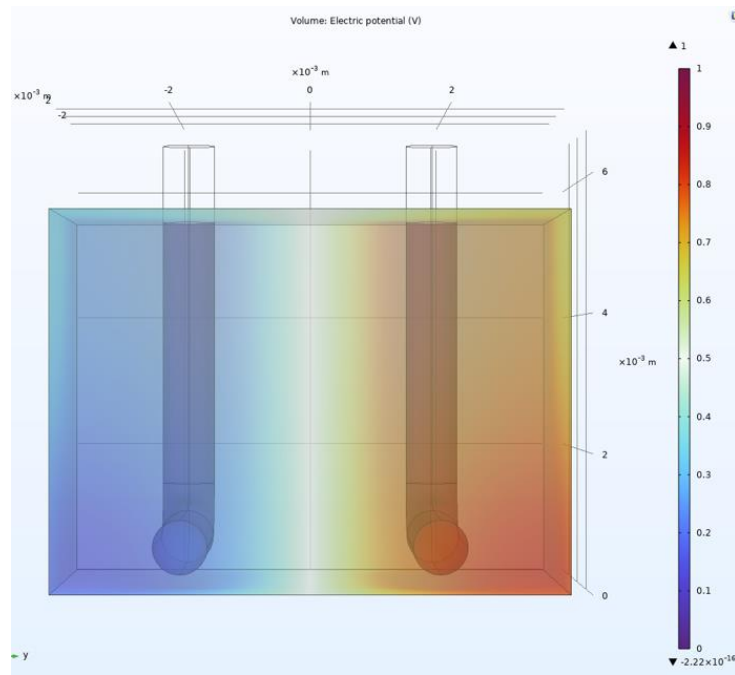
Figure 2.4: Electric potential distribution within the model. The unit of the color legend is V.
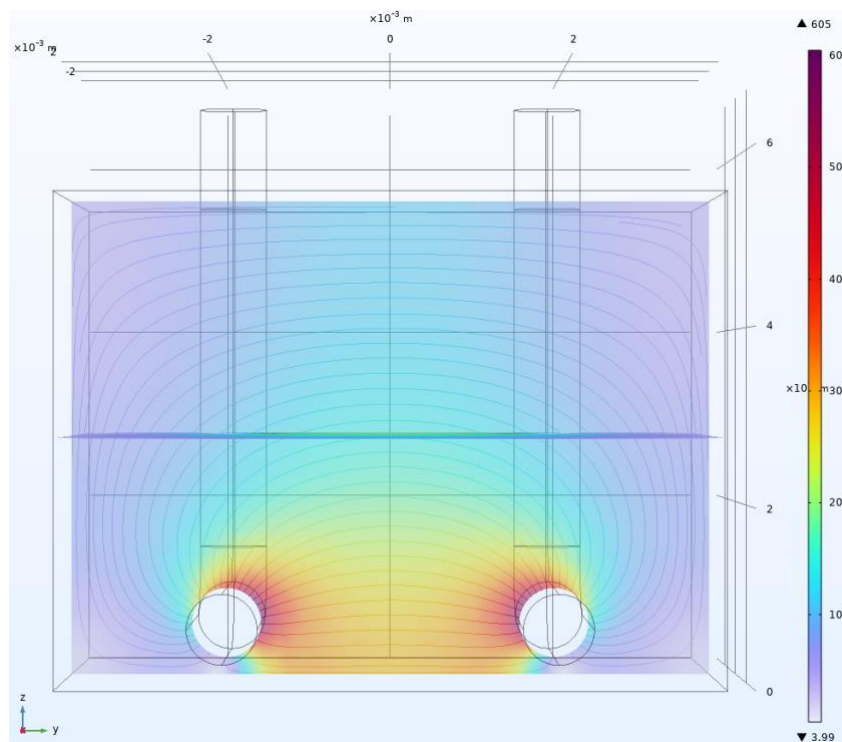

Figure 2.5: Electric field distribution within the model. The unit of the color legend is V/m.

Since the electric field strength is approximately equal to the voltage-to-distance ratio, we can make a simple calculation that will tell us, what should be the maximum distance between the electrodes that will enable us to electroporate the cells, considering the maximum voltage output (1000 V) and maximum current output (6-10 A) of the chosen pulse generator ELECTROcell B10 HVLV (see Section 2.2.2).

The electric field required to electroporate a cell depends on the cell type; based on previous experiments with H9c2 cells [51], we expect that achieving an electric field of 100 V/mm should be sufficient. The maximum possible inner distance between the electrodes, considering the dimensions of the well, is 5 mm, when allowing some additional space between the electrode and the wall of the well to avoid friction. At the maximum output voltage of the pulse generator, we can for this electrode distance an electric field strength of 1000 V / 5 mm = 200 V/mm, which is well above our expected electric field strength sufficient for electroporation.

However, we also need to consider the maximum output current of the pulse generator. To this end, we need the information about the resistance between the electrodes. To compute the resistance from the model, we integrated the electric current density over the boundary of one of the electrodes to obtain the total current, and then calculated the ratio between the applied voltage and this current.

Figure 2.6 shows how the resistance depends on the distance between the electrodes. For the electrode distance of 5 mm, the resistance is 135.98 Ω. If applying 1000 V, the current would be 7.35 A, which is within the output limit of the pulse generator. Since we wanted to electroporate as many cells as possible within the well, we decided to design electrodes with this maximum electrode distance.
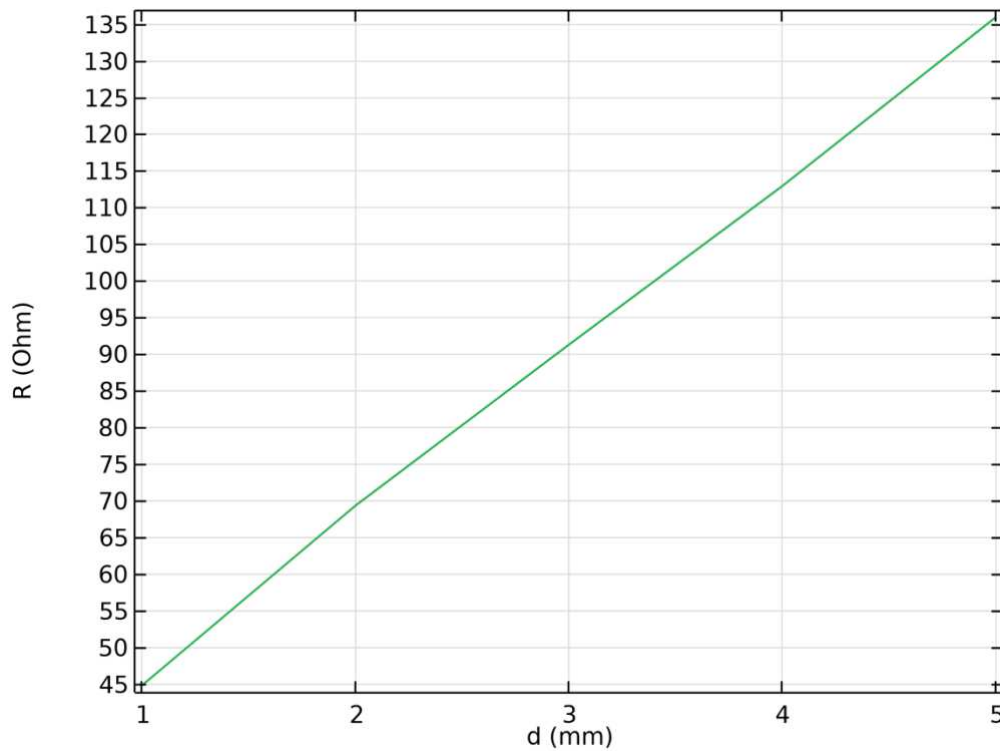
Figure 2.6: Plot of the correlation between the inter-electrode distance *d* and resistance *R* of the sample.

2.1.2. ELECTRODE DESIGN AND CREATION USING 3D PRINTING

After identifying the suitable distance between the electrodes, the next step was to design a holder that would provide sufficient stability inside a μ-Plate 96 Well Black and that would respect the previously established electrode spacing.

As the Laboratory of Biocybernetics at the University of Ljubljana is equipped with a Prusa 3D printer, it was immediately decided to use it to create a fully customized holder that met all the requirements for use in the experimental setup. The holder was designed using Blender 4.0 software.
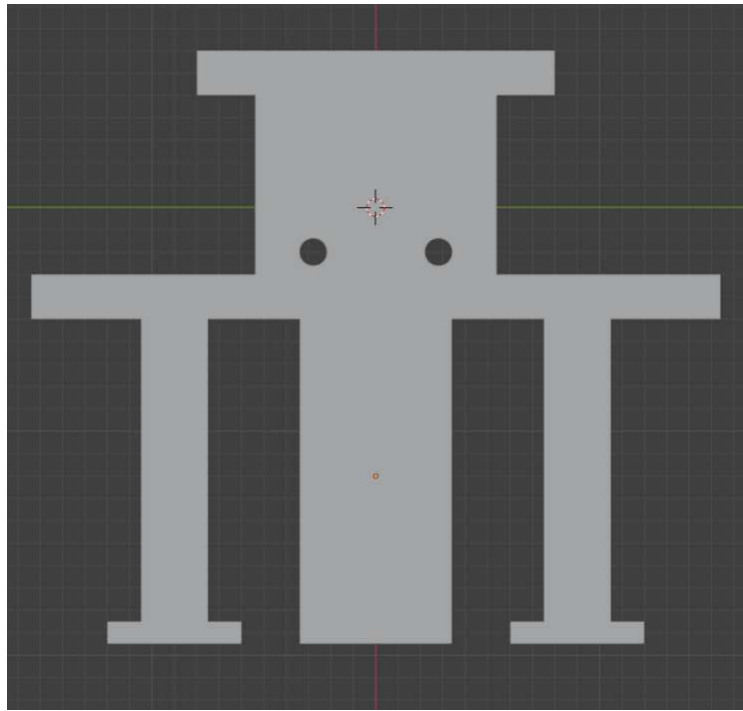
Figure 2.7: Front view of the holder designed in Blender 4.0.

The holder (Figure 2.7) essentially consists of a rectangular parallelepiped with a 7.4 mm square base and a height of 26 mm, to which two further side support arms, also with a 7.4 mm square base, have been added to provide additional stability inside the μ-Plate 96 Well Black, and two ergonomic side protrusions at its top to make it easier to manually insert or remove the holder from a well of the μ-Plate.
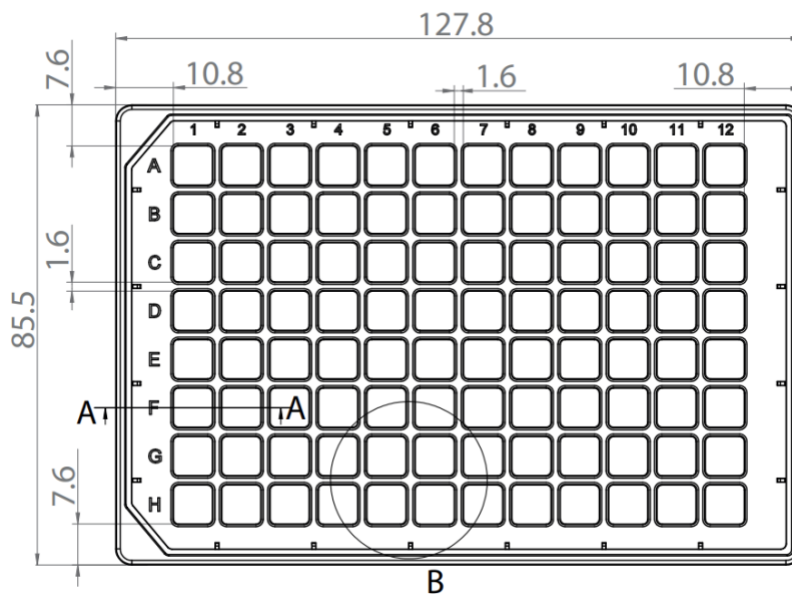

Figure 2.8: Geometry and dimensions of the μ-Plate 96 Well Black made by Ibidi.

For creating the holder using a 3D printer, the 3D model drawn in Blender 4.0 was exported to a .stl format file and then imported into the PrusaSlicer software. PrusaSlicer allows objects to be loaded within an environment that is capable of exporting everything within the Prusa Mk4 platform into G-code. The 0.10 mm FAST DETAIL was used as the print settings, the Prusament PLA material and the MK4 Input Shaper 0.4 nozzle.
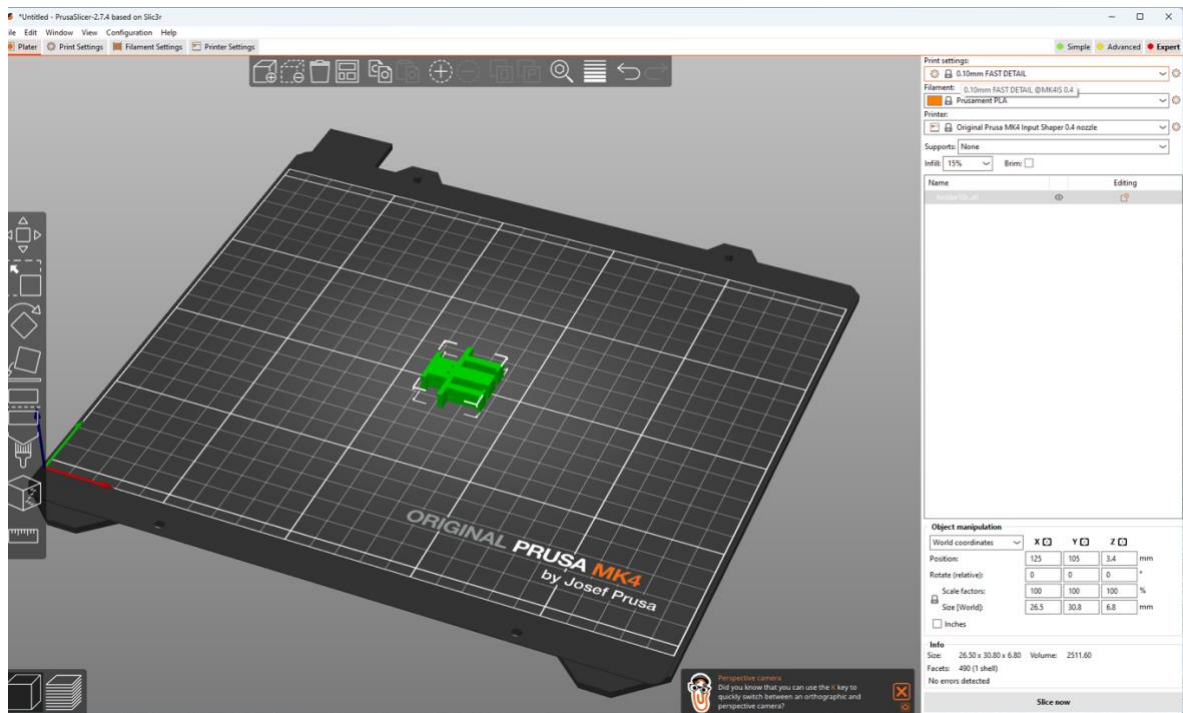

Figure 2.9: Screenshot of the working environment of the PrusaSlicer software.

Following the creation of the holder, we proceeded with the insertion of the electrodes, i.e. the insertion of two platinum/iridium wires with a diameter of 0.8 mm, which were then glued to the holder using two-component glue, putting particular attention to keeping the two electrodes parallel and clean from the glue. The glue acts and an insulating layer and is also toxic to the cells, therefore, we needed to avoid any contamination with the glue of the electrode parts, which will be submersed into the medium with cells, as well as the parts of the electrodes which will be connected to the pulse generator.

The final distance between the electrodes was measured with a caliper and was 4.7 mm, sufficiently close to the desired distance of 5 mm.

2.1.3. SELECTION OF THE CELL LINE AND THE FLUOROPHORE

In order to proceed with the experimental analysis, it was necessary to choose both the type of cells to be used and subjected to electroporation as well as an appropriate fluorescent dye (fluorophore) that will enable visualization of electroporation using fluorescence microscopy. H9c2 cells, a cardiac myoblast cell line derived from BDIX rats, were selected for experiments. Developed in 1982, they have become a widely used cell model for studying cardiac function, hypertrophy, and heart disease [52]. These cells provide many advantages: first, these cells are easy to cultivate, have characteristics similar to primary cardiomyocytes, and have an elongated shape, which makes it possible to study how their geometry and orientation influences the process of electroporation [51].
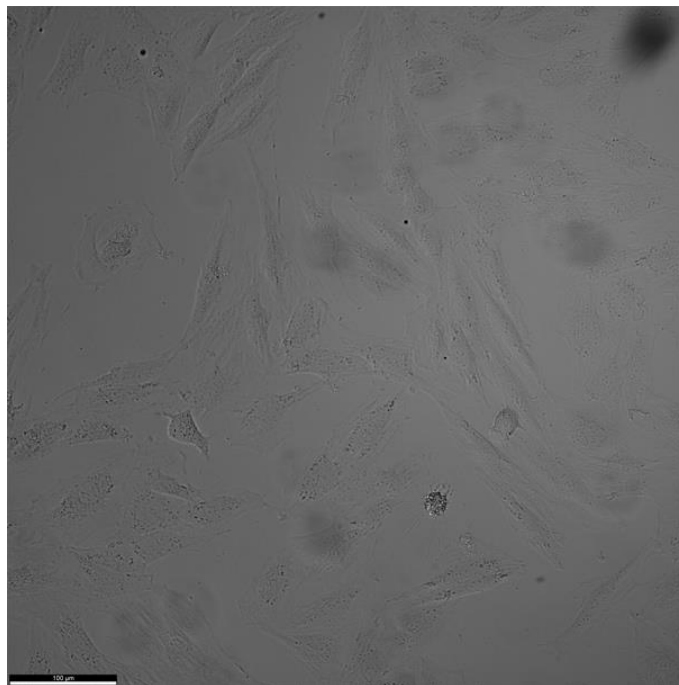

Figure 2.10: Brightfield image of H9c2 cell line acquired using Leica Thunder microscope under 40× objective magnification.
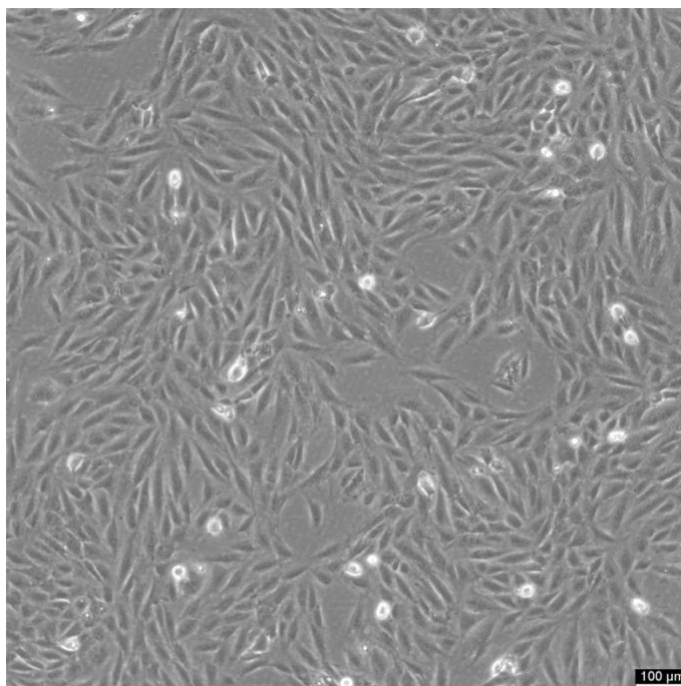
Figure 2.11: Brightfield image of H9c2 cell line acquired under 10x objective magnification.

In the study of the electroporation phenomenon, fluorescent and colorimetric dyes represent an essential tool [53]. Specifically, dyes that cannot freely cross an intact cell membrane but can cross a permeabilized (electroporated) membrane can be used as an indicator of electroporation. On possibility is to add the dye to the extracellular medium; if a cell becomes electroporated, the dye will enter the cell and the cell will become stained. Two examples of dyes that can be used in such way are propidium iodide and trypan blue. These dyes are also often used as indicators of dead cells since cells lose their membrane integrity upon necrotic cell death.

Another possibility is to stain the cells with a dye before electroporation and monitor the leakage of the dye from the cells due to electroporation. A dye that can be used in such way is calcein AM. The advantage of such a dye is that all cells can be clearly seen under a fluorescent microscope before pulse application, which allows automatic detection of cells in the acquired fluorescence images and consequently image segmentation. Thus, calcein AM was selected for our experiments.

Calcein, also known as fluorexon, is a fluorescent dye belonging to the xanthene family. It is characterized by intense green light emission when excited by blue or ultraviolet light and cannot cross an intact cell membrane [54]. When the carboxylic acid groups on calcein are modified with acetomethoxy (AM) groups to obtain calcein AM, this calcein derivative is non-fluorescent and can freely cross the cell membrane. Once inside the cells, the intracellular esterases cleaves the AM groups, converting the calcein AM into its fluorescent form and trapping the calcein inside the cell.

In addition to its use as an electroporation indicator, calcein is also widely used for:

- **Cell viability assays**: Calcein AM can be used to distinguish living from dead cells, since the esterase that cleave the AM group and convert calcein AM into a fluorescent form are active only in living cells. This allows live cells to be visualized and non-viable cells to be identified.

- **Cell tracking:** By staining cells with calcein it is possible to track their movement and migration. Combined with antibodies or other ligands, calcein makes it possible to mark specific cell populations and monitor their path within tissues or organisms.

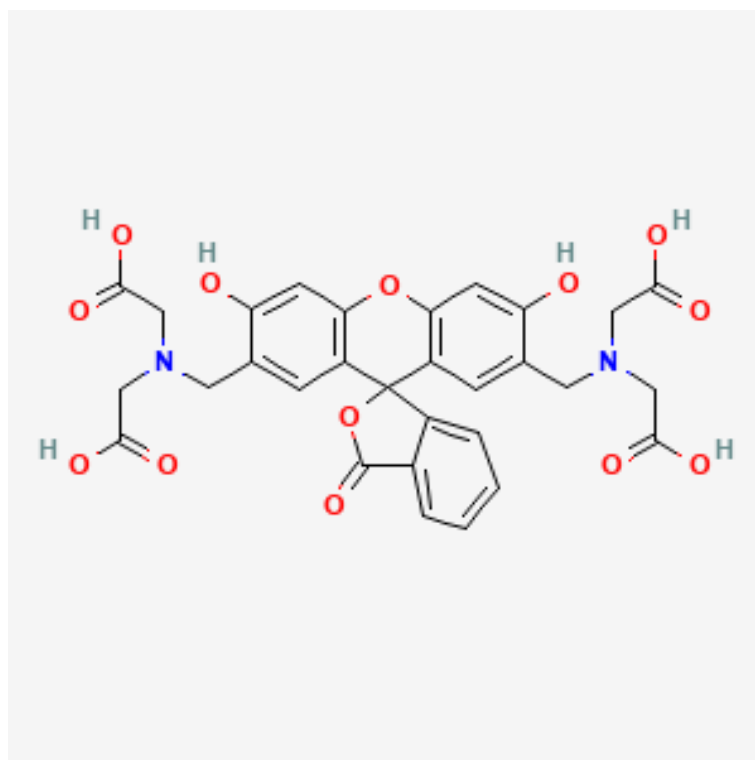**Figure 2.12:** Vial with calcein AM dye used for cell staining [54].

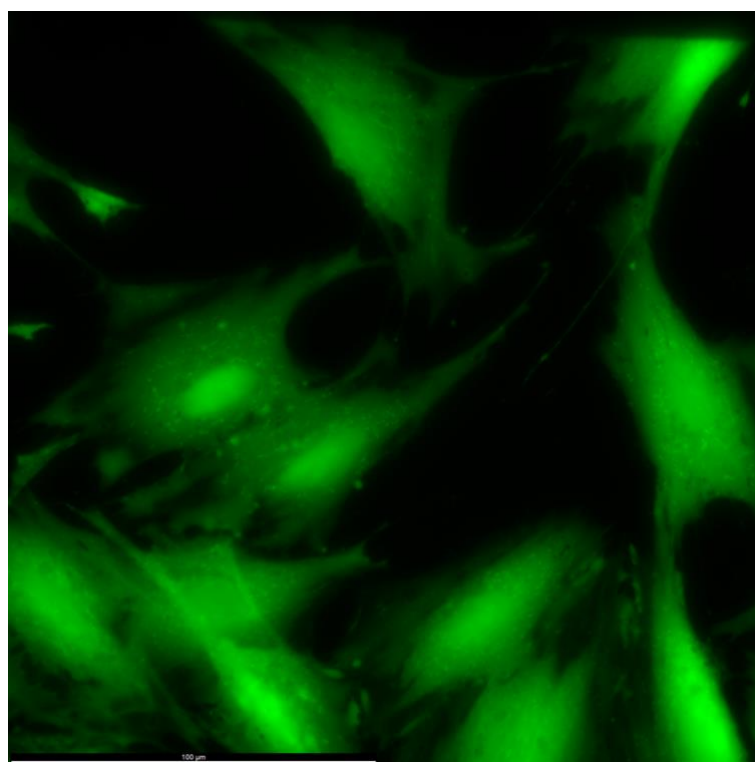**Figure 2.13:** Chemical structure of the calcein compound [55].

Figure 2.14: Fluorescence image of H9c2 cells stained with calcein AM.

2.2. EQUIPMENT AND SOFTWARE USED FOR DATA ACQUISITION AND ANALYSIS

2.2.1. FLUORESCENCE MICROSCOPE

For fluorescence imaging we used the Leica Thunder Imager System (Figure 2.15), which consists of an inverted wide-field microscope DMi8, a LED8 illumination source with 8 LEDs emitting light at different wavelengths, a set of excitation and emission filters, sCMOS camera DFC9000 Gt and 6 objectives with different magnifications (5×, 10×, 20×, 40×, 63×, and 100×), all from Leica Microsystems, Germany. The microscope is surrounded by an incubator that allows the option to control the sample's temperature. The microscope is controlled with the LAS X software.

Figure 2.15: Microscope Leica Thunder Imaging System and representation of working software LAS X [56].

2.2.2. PULSE GENERATOR

The ELECTROcell B10 HVLV from Leroy Biotech, France (Figure 2.16) is a pulse generator capable of generating high-voltage short monopolar and bipolar rectangular pulses used in electroporation treatments. The amplitude and duration of the positive and negative pulse can be controlled separately. This pulse generator was used to apply, via electrodes, a series of monopolar pulses of standard duration 100 μs at different voltages.
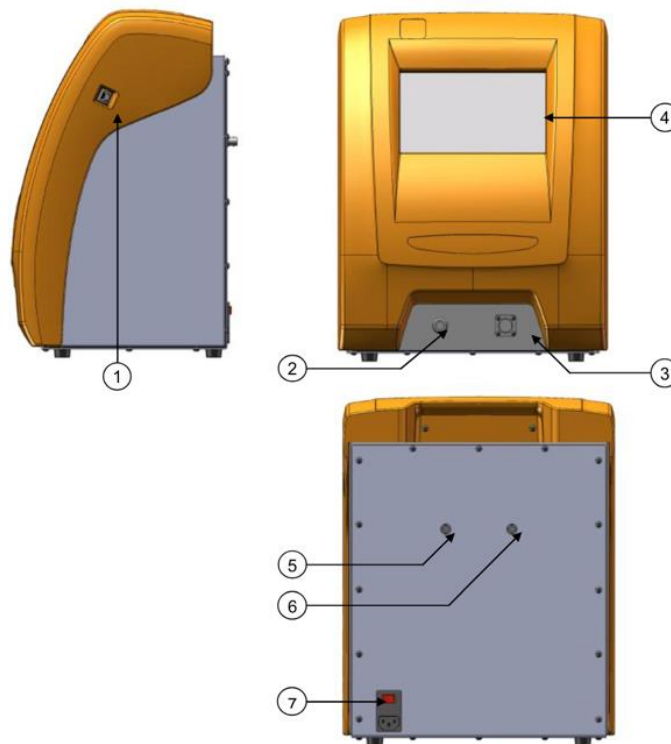

Figure 2.16: Structure of the ELECTROcell B10 HVLV pulse generator [57].

2.2.3. OSCILLOSCOPE AND PROBES

The Lecroy WaveSurfer 422 200Hz oscilloscope (Figure 2.17) was used for routine monitoring the applied pulses using the differential voltage probe Lecroy AP305, and the current passing through the sample using the current probe Lecroy AP015.Figure 2.18 shows the waveform of the delivered pulses.

Since Lecroy WaveSurfer 422 oscilloscope does not allow to acquire high-resolution graphs of multiple applied pulses separated by long inter-pulse intervals, this graph was obtained with oscilloscope Lecroy HDO4104A in sequence mode, using differential voltage probe Lecroy HVD3206A and current probe Lecroy CP031A.

By calculating the ratio between the voltage and current during the applied pulses, we can determine the resistance of the sample between the electrodes. Based measurements of three samples, we found that the resistance is 151 ± 14 Ω (mean ± standard deviation), which just slightly higher than the resistance predicted in our computational simulations (~130 Ω), considering the electrode distance of 4.7 mm.
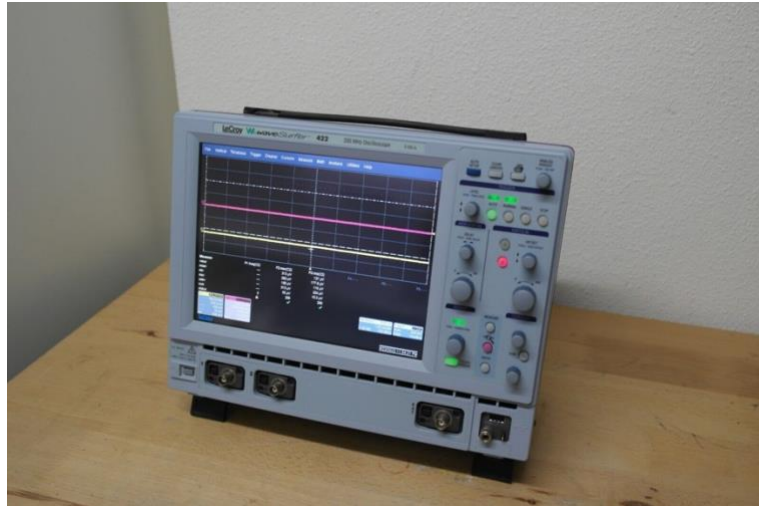

Figure 2.17: Oscilloscope Lecroy WaveSurfer 422 200Hz.
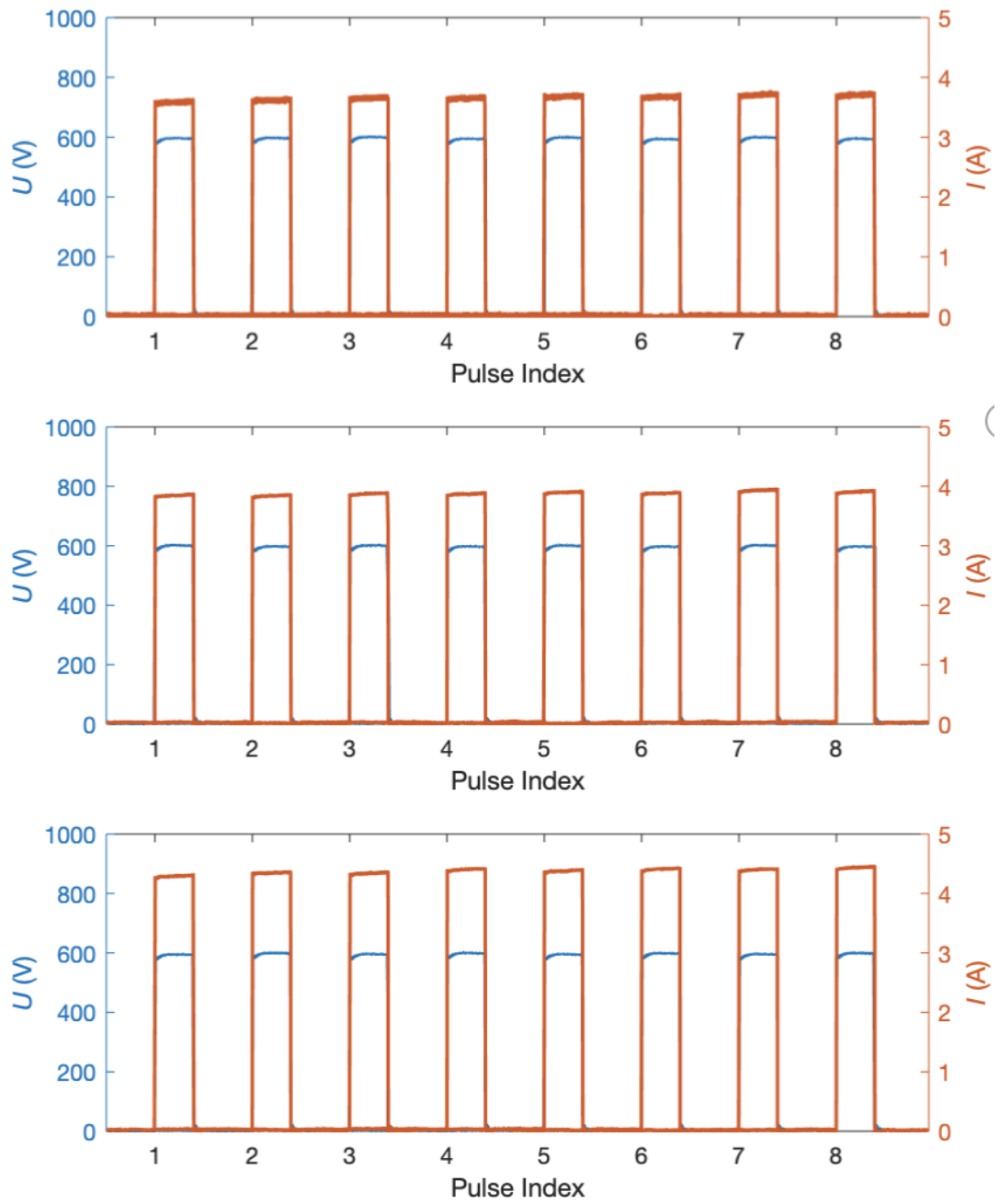
Figure 2.18: Graph of the captured voltage and current when applying pulses with voltage of 600 V.

2.2.4. CELLPROFILER SOFTWARE

CellProfiler, developed by the Broad Institute of MIT and Harvard, is an open-source software for analyzing images of cells and tissues [58]. This versatility makes it an excellent tool that offers a wide range of functions for analyzing very complex images. This software was used for determining the granularity of the acquired fluorescence images.
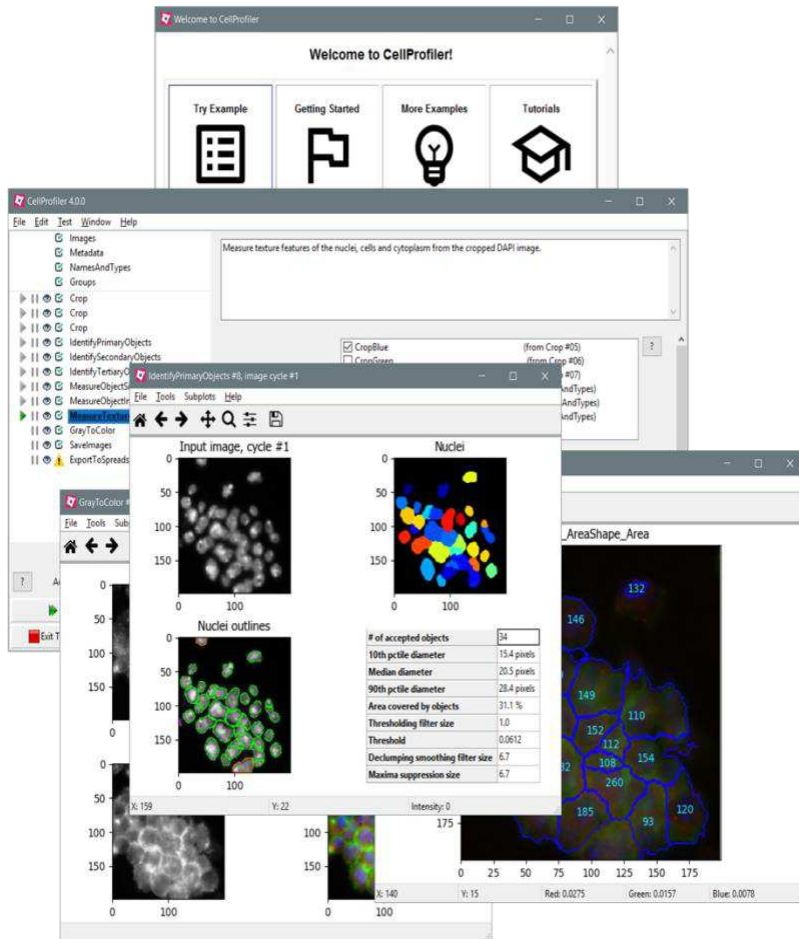
Figure 2.19: Various inputs and outputs of the CellProfiler software.

2.2.5. IMAGEJ FIJI SOFTWARE

ImageJ is an open source software developed by the National Institute of Health (NIH) for analysis and elaboration of images [59]. In this thesis, the "Fiji" distribution of ImageJ [60] was used for analyzing the kinetics of fluorescence change in the acquired timelapse images.
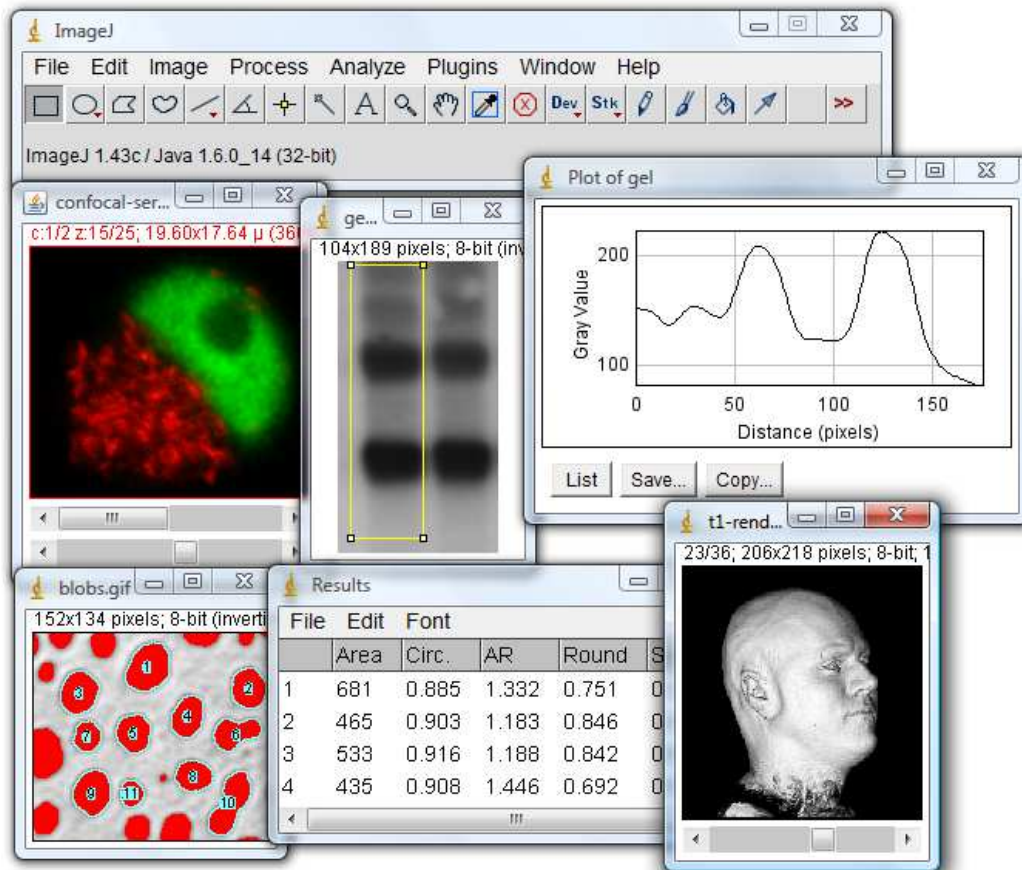

Figure 2.20: Various input and outputs of the ImageJ software [59].

2.3. EXPERIMENTAL PROTOCOLS

2.3.1. CELL CULTURE

The preparation begins with turning on the water bath, set to 37°C and inserting the trypsin solution and the cell culture medium (Dulbecco's Modified Eagle's Medium-High glucose) inside the water bath to warm them up. Meanwhile the laminar flow cabinet is cleaned using a gauze soaked in alcoholic disinfectant (70% ethanol) to ensure a sterile environment.

As the next step, flasks are prepared with different volumes of the cell culture 75 cm² flasks with 10 ml of medium were used. In addition to that, the hemocytometer is prepared for subsequent cell counting.
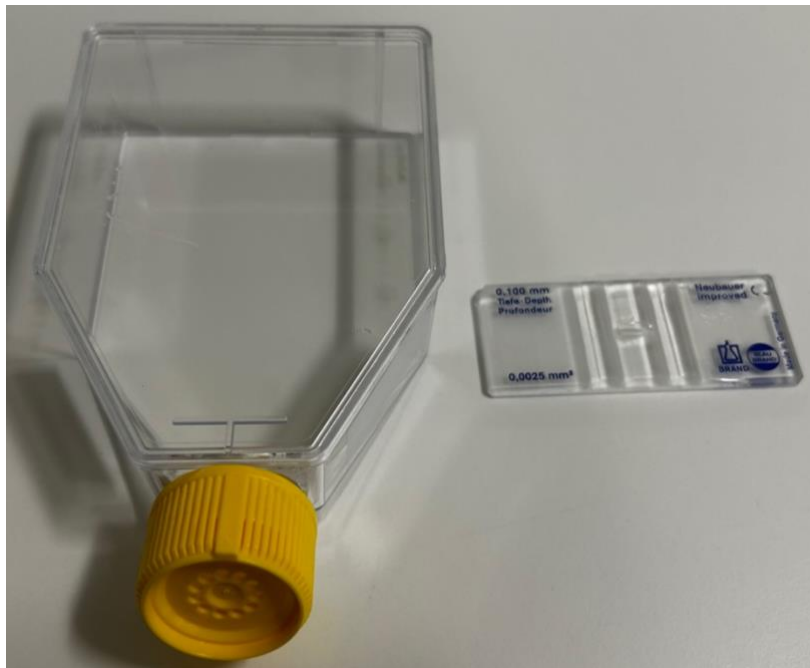
Figure 2.21: Picture of a 75 cm² flask and hemocytometer used for cell culture and cell counting.

The protocol begins with the observation of the cells under a microscope with 4× objective magnification to assess their condition. After that we proceed with the aspiration of the medium from the flask using a sterile glass pipette, followed by the addition of 5 ml of physiological saline solution (0.9% NaCl) to remove any residual cell culture medium. The cell culture medium contains serum, which inhibits the activity of trypsin used for detaching cells from

40

their growth surface. Next, after aspiration of the saline, 5 ml of trypsin is added, and a stopwatch is being used to ensure the right exposure of the cells to trypsin, never more than 3 minutes. The reaction is stopped by adding the remaining half of the volume of the cell culture medium. Finally, the cells are mixed with the pipette and 10 μl of the cell suspension is placed in the hemocytometer for counting.
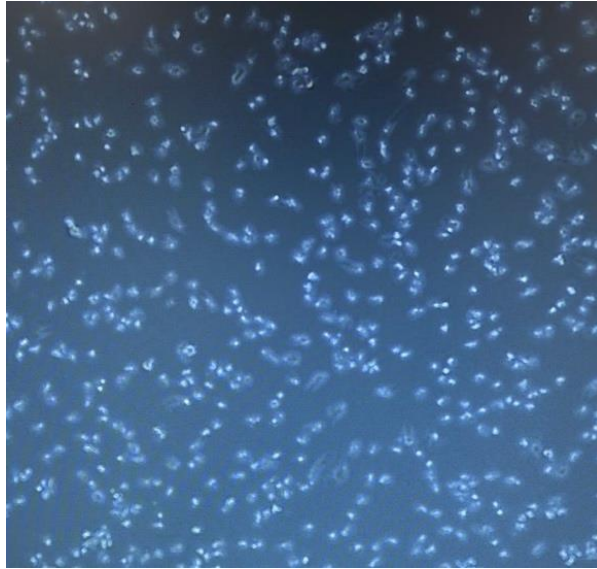
Figure 2.22: H9c2 cells get round and start detaching from the surface under the effect of trypsin.

2.3.2. SEEDING CELLS FOR EXPERIMENTS

After collecting and counting the cells, we proceed with the preparation of the μ-Plate 96 Well Black, in which the cells will be seeded. We start by placing the physiological saline all around the outer wells of the entire plate to minimize evaporation of the medium from the wells with seeded cells. In the wells to which the cells will be seeded, first 200 μl of cell culture medium is pipetted. Next, a selected volume of the cell suspension is added into each well. For easier image analysis it is important not to have cells that are too crowded.

Thus, we opted for 50% confluency of the cell culture (the surface area covered by the cells) on the day of the experiment. The experiments using the Leica Thunder microscope were repeated on 3 different days. To have the appropriate cell density after 1 day, after 2 days, and after 3 days, we seeded different number of cells per well, as indicated in Table 2.B.

Table 2.B: Volume of the cell suspension and the corresponding number of cells seeded per well for experiments carried out on day 1, day 2 and day 3 after seeding.

CELLS DENSITY	DAY 1	DAY 2	DAY 3
$2.1*10^5$ cells/ml	40 µl	20 µl	10 µl

2.3.3. STAINING CELLS WITH CALCEIN

On the day of the experiment, the cells grown in the µ-Plate are stained with calcein. The staining process begins by dissolving 8 µl calcein AM stock solution in 4 ml of Tyrode buffer to obtain a final staining solution with calcein AM concentration of 2 µM. The cell culture medium within the wells of the plate is aspirated, making sure to always place the aspiration pipette in the same place. The staining solution is then introduced into the wells. The plate is then incubated for at least 30 minutes at 37°C with 5% CO_2. After incubation, the staining solution is replaced with 200 µl of DMEM medium to conclude the staining process. Finally, the plate is placed onto the microscope stage and prepared for imaging.

Figure 2.23: μ-Plate 96 Well Black from Ibidi.

2.3.4. PREPARATION OF THE PULSE DELIVERY SYSTEM

To prepare the pulse generator, the oscilloscope, and the electrodes, the following steps are made. The Electrocell B10 generator is switched on and set to the right settings for acquisition, the delivery of 8×100 μs pulses of selected voltage (0 V, 200 V, 400 V, 600 V, or 800 V), applied with a period of 1 s.

Figure 2.24: Setting of the Electrocell B10 pulse generator.

The oscilloscope is also switched on. Channel 1 is connected to the current probe AP015 and set at 5 A/div. The current probe is degaussed and auto zeroed with the oscilloscope's automatic procedure. Channel 2 is connected to the voltage probe AP305 and set at 200 V/div. The voltage probe is auto zeroed with the oscilloscope's automatic procedure.
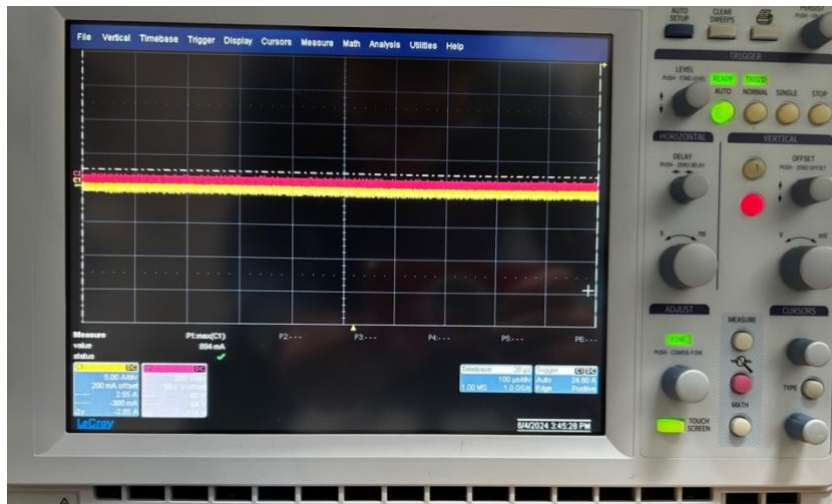
Figure 2.25: Picture of Oscilloscope settings.

Electrodes are then connected to the pulse generator, as shown in Figure 2.26. Cables are immobilized with Patafix to not move and disconnect.

Figure 2.26: The μ-Plate placed on the microscope stage. The electrodes are mounted into one of the wells and connected to the pulse generator.

2.3.5. IMAGE ACQUISITION

After preparing the pulse delivery system, a region of interest with cells located roughly in the middle between the electrodes is focused on the microscope using a 63× objective magnification. Afterwards, the response of cells to an electric pulse is monitored in time-lapse acquisition mode, with one fluorescence image captured every 10 seconds for a total of 15 minutes, resulting in 91 frames per time-lapse. The pulse with selected amplitude is applied 90 s after the start of the time-lapse acquisition. This allows us to capture images before and after pulse delivery. For images of the calcein dye fluorescence, the following settings are used: the dye is excited with 475 nm LED at 5% its maximum power (i.e. at 10 mW) using an exposure time of 10 ms.

The emitted fluorescence is passed through the Leica DFT51010 multipass filter and captured with the camera without any binning of the camera pixels. Finally, we pass on to the 'Calcein Navigator' module. Entering the navigator, a spiral scan is set up and the entire well is acquired (Figure 2.A).

This process is repeated for each well, whereby each well is exposed to a pulse with different amplitude (0 V, 200 V, 400 V, 600 V, 800 V), for a total of 5 acquisitions per day and 15 acquisitions for all three experimental repetitions.
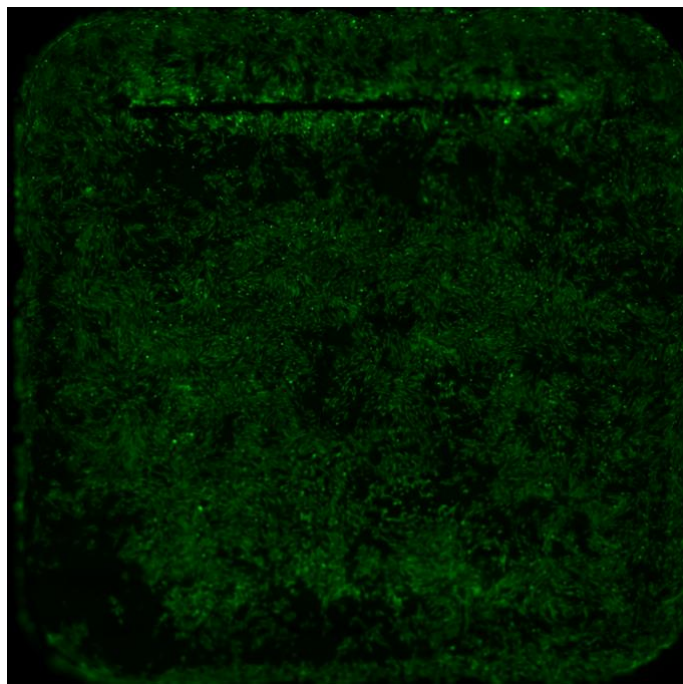

Figure 2.A: Acquisition of an entire well after staining.

2.4. IMAGE ANALYSIS

2.4.1. EXTRACTION OF THE TIME COURSE OF THE AVERAGE CELL FLUORESCENCE INTENSITY IN FIJI

We initially wanted to use CellProfiler to automatically segment each individual cell and track the time course of its fluorescence. However, since the cell fluorescence was decreasing with time due to electroporation, considerably different regions were segmented in each image. In principle it would be possible to overcome this issue by segmenting the cells in only the first acquired image and then projecting these segmentations to all other images in the time-lapse. However, we were unable to create a pipeline in CellProfiler that would enable such an approach of image analysis; the CellProfiler always performed independent segmentation of each image in the time-lapse. Therefore, we resorted to ImageJ Fiji software using a procedure previously established by the colleagues from the Laboratory of Biocybernetics.

First, all time-lapses acquired with the LAS X software were saved in files with the software's default .lif extension. Since Fiji can read .lif files, it was unnecessary convert the data into a different format. Subsequently, each timelapse was loaded into Fiji for analysis. A custom macro, provided in Code 2.A was used for automatic image analysis, ensuring consistency, and avoiding any potential human error or bias.

Code 2.A: macro used to improve analysis of extracted images.

```
// Macro to analyze timelapse of Fluo4 signal
//run("Duplicate...", "duplicate"); // Duplicate the original timelapse - useful when developing the macro,
unnecessary otherwise.

// Preparations to start fresh
close("ROI Manager"); // Close roiManager if opened - this will reset the roiManager
close("Log"); // Close Log if opened - this will reset Log
run("ROI Manager...");

// Determine the threshold for cells ROI
image0 = getImageID(); // Save the ID of the original timelapse (will be used at the end of the macro).
```

```
setSlice(1); // Select the first frame.

run("Duplicate...", "use"); // Duplicate the selected frame only.

//setThreshold(1300, 65000); // Set a fixed value of the threshold.

//setAutoThreshold("Percentile dark"); // Set threshold automatically.

setAutoThreshold("Huang dark"); // Set threshold automatically.

getThreshold(lower,upper); // Get the threshold values.

run("Median...", "radius=5"); // Run median filter to reduce salt&pepper-like noise.


// Create cells ROI

run("Create Mask"); // Create mask from the threshold image.

run("Create Selection"); // Create ROI based on the mask; this ROI represents the cells within the entire field of view.

roiManager("Add"); // Add the ROI representing the cells to roiManager.

makeRectangle(60, 60, 1928, 1928); // Make another rectangular ROI that covers the inner 96% of the field of view.

//makeRectangle(4, 4, 508, 508); // Make another rectangular ROI.

roiManager("Add"); // Add the rectangular ROI to roiManager.

roiManager("AND"); // Perform AND operation on the two ROIs; you end up with the final ROI which selects the cells within the inner 77% of the field of view.

roiManager("Add"); // Add the final ROI to roiManager.


// Get mean intensities within the final ROI in the original timelapse

selectImage(image0); // Select again the original timelapse.

roiManager("Select", 2); // Copy the final ROI to the original timelapse.

roiManager("Multi Measure"); // Measure the average intensity witin the final ROI in all frames of the timelapse.

meanvalues1 = newArray(nResults); // Prepare array for mean values

for(j = 0; j < nResults; j++) {

meanvalues1[j] = getResult("Mean1", j);

}

run("Clear Results"); // Clear results


// Get background

selectImage(image0); // Select again the original timelapse.

setSlice(1); // Select the first frame.

run("Enhance Contrast","saturated=1"); //Improve the constrast

waitForUser("Select ROI for background subtraction");

roiManager("Add"); // Add the rectangular ROI to roiManager.

roiManager("Select", 3); // Copy the final ROI to the original timelapse.

roiManager("Multi Measure"); // Measure the average intensity of the background in all frames of the timelapse.

meanvalues2 = newArray(nResults); // Prepare array for mean values

for(j = 0; j < nResults; j++) {

meanvalues2[j] = getResult("Mean1", j);
```

```
}
// Save data to a text file
imageName = getTitle();
ddir = "C:/Users/davidemene/OneDrive - Università degli Studi di Padova/Desktop/kinetics days light/output avg
fluo intensity/";
//path = ddir + replace(replace(imageName, "/", "_"),".","_") + ".txt";
path = ddir + "fluo1.txt";
f = File.open(path);

for(j = 0; j < nResults; j++) {
print(f,d2s(meanvalues1[j],3) + "\t" + d2s(meanvalues2[j],3));
}
print(f,d2s(lower,0))
File.close(f)
```

The procedure defined in the macro starts by automatically thresholding the first image in the time-lapse using an embedded thresholding method "Percentile". Once the threshold has been determined, an image mask is created (Figure 2.27). This mask serves as the basis for defining the region of interest (ROI), corresponding to the areas that exceed the fluorescence threshold, i.e. the cells stained with calcein.
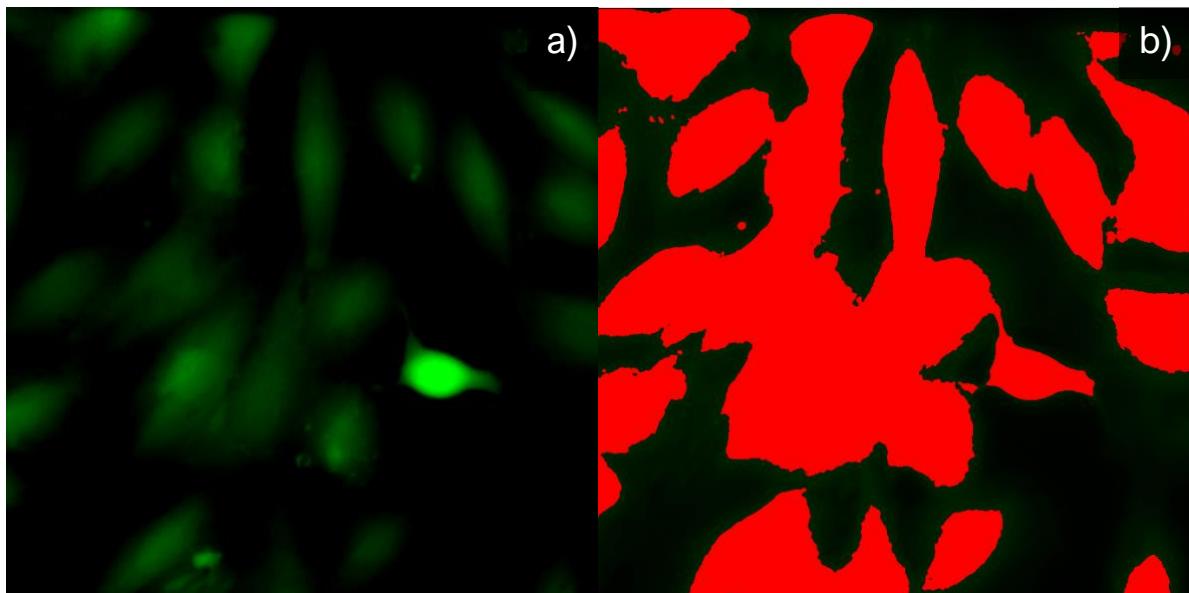

Figure 2.27: Raw fluorescence image (a) and the corresponding mask (b) obtained after automatic thresholding of the fluorescence image.

From the mask, a ROI is generated (Figure 2.28a). Next, a rectangle covering 96% of the field of view is defined (Figure 2.28b). The rectangle is then combined with the original ROI via a Boolean AND operation (Figure 2.28c). This is done to remove areas close to the edges of the image, where the automatic thresholding does not always correctly select the cells, from the image analysis.
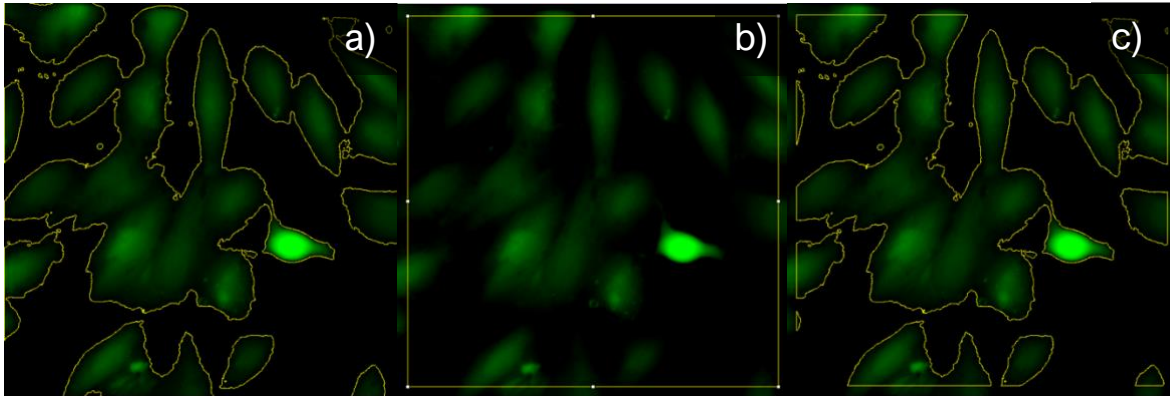

Figure 2.28: The procedure for defining the ROI for analysis. The ROI obtained after automatic thresholding (a) is combined with a rectangular region (b) to obtain the final ROI(c).

After defining the ROI, the algorithm proceeds to extract the average intensity of all pixels within the ROI in each frame of the timelapse. To ensure an accurate analysis, a small region outside the ROI is manually selected to determine the background intensity (Figure 2.29a). The extracted values are then saved in a text file (Figure 2.29b). This text file was then imported into Matlab, where further data processing was carried out.
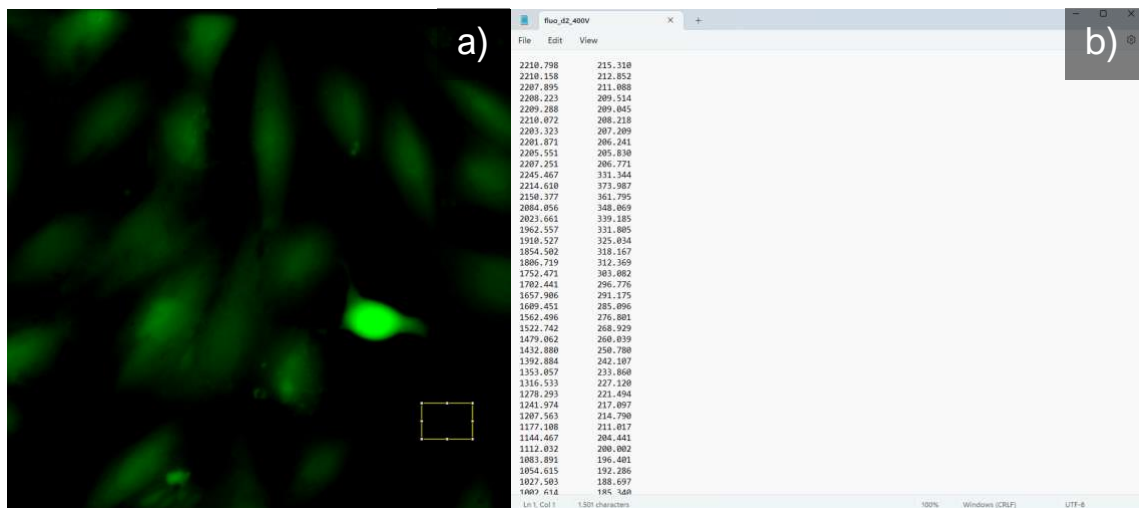
Figure 2.29: Example of a manually selected background region (a) and an example of the extracted values of average fluorescence (first column) and background (second column) intensity for each image in the time-lapse (b).

2.4.2. IDENTIFICATION OF GRANULARITY FEATURES WITH CELLPROFILER

In order to characterize the changes in the cell granularity, we utilized CellProfiler. We developed a pipeline that allowed for extraction of desired features from the fluorescence images, specifically their granularity.

To begin the process, we loaded one image per minute of acquisition, resulting in a total of 16 images for each experiment. These images were then renamed as the 'calcein' set, which facilitated their identification and organization within the pipeline.

The initial step in the pipeline involved the utilization of the 'IdentifyPrimaryObjects' function. This function played a crucial role as it enabled the identification and isolation of objects within the images. To focus solely on the objects of interest, we established a size range of 100 to 1000 pixels, effectively excluding any objects that fell outside of this range or were in contact with the edge of the image.

Following this, we proceeded to configure the 'Measure Granularity' function within the pipeline. By utilizing a 25% scaling (subsampling), this function performed vital tasks such as conducting granularity measurements and reducing background noise. The algorithm employed in the function would then generate a series of disc-shaped structuring elements that were

subsequently used to filter the images. These processes allowed us to obtain the values pertaining to the granularity of the cells.
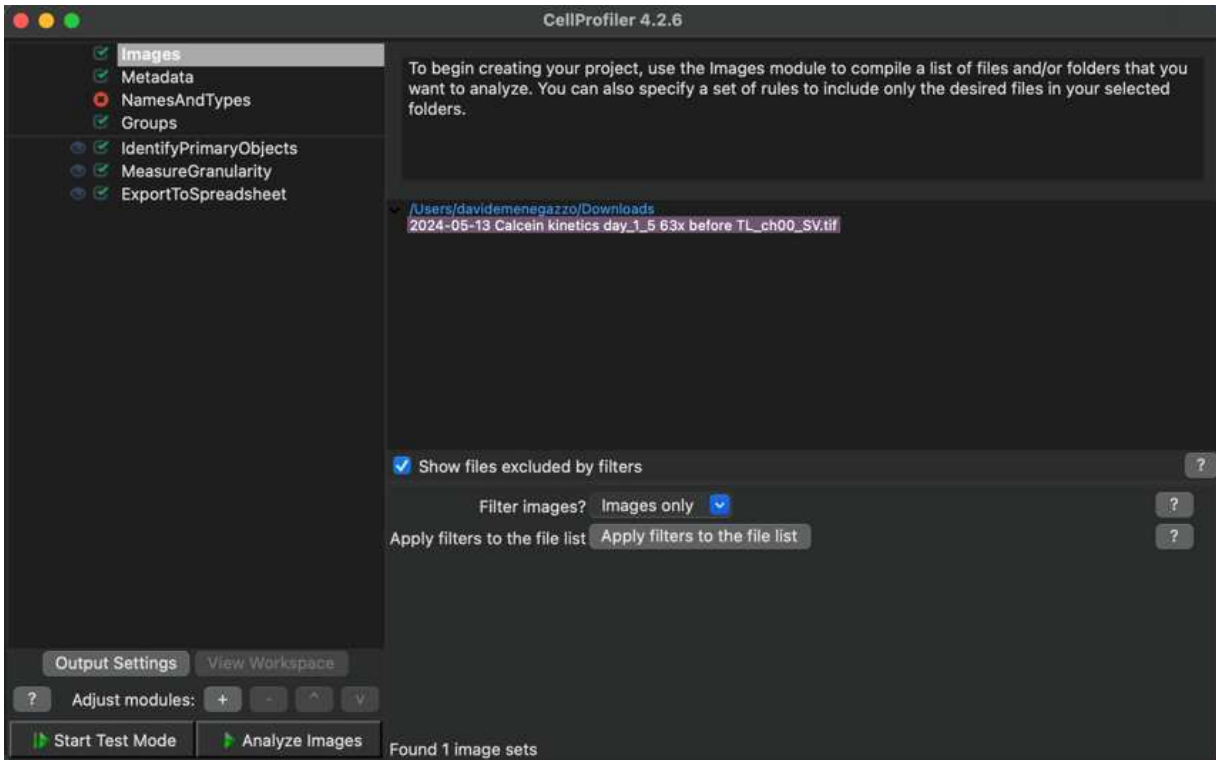

Figure 2.30: Pipeline used in the CellProfiler application.

CHAPTER 3: RESULTS AND DISCUSSION

This chapter will present and discuss the results obtained through the acquisitions. The section is divided into two macrocategories, each of which covers a specific aspect of the analyses conducted during the experimental days.

The first macrocategory is devoted to the analysis of the mean fluorescence of cell cultures subjected to electroporation for a period of 15 minutes. Analyses began with a control test at 0 V, followed by subsequent acquisitions in which the voltage was increased by 200 V for each experiment until the maximum applied voltage of 800 V. This approach allowed the behavior of the cells at various voltage levels to be observed and compared. The data obtained provided significant indications on the degree of permeabilization of the cell membrane in response to the different voltages applied.

The second macrocategory concerns the analysis of cell granularity and its change as a function of the gradual increase in voltage. Again, experiments were conducted by increasing the voltage by 200 V for each phase, until the final value of 800 V was reached. This analysis made it possible to assess the structural changes within the cells by correlating the level of granularity with the intensity of the applied electric field.
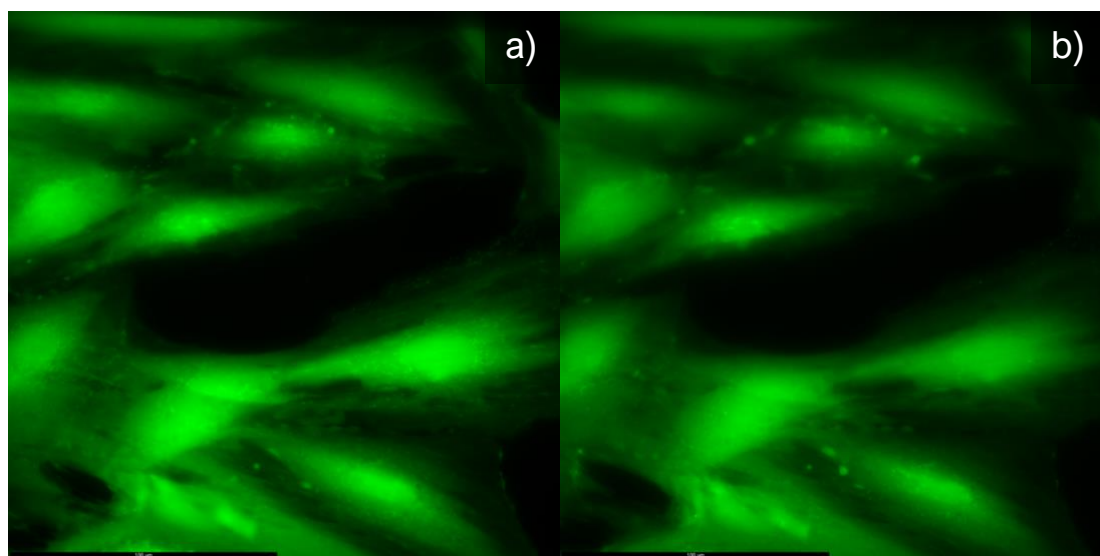
3.1. TIME COURSE OF THE AVERAGE FLUORESCENCE INTENSITY

After successfully acquiring all image sets corresponding to the time course of the change in calcein fluorescence within the cells, we move on to visualize and analyze the distinctive features of the 5 acquisitions at different applied voltages over the three days of experiments.

3.1.1. CONTROL SAMPLES (0 V)

In the acquisitions taken at 0 V (control acquisitions), as can be seen in Figures 3.1a and 3.1b, acquired at the beginning and end of the time-lapse, respectively, no significant differences in brightness and no signs of cell permeabilization are evident. These acquisitions were made to allow analysis of any abnormalities or divergent behavior from expectations in the samples subjected to electroporation. However, slight variations in average fluorescence intensity are noted, as illustrated in Figure 3.1c, where the x-axis represents time in seconds and the y-axis indicates fluorescence intensity, minus the extracted background value.

This phenomenon of slight and constant decrease in intensity, known as photobleaching, is present on all three days of acquisition (the red line represents day 1, the blue line day 2, and the green line day 3). The extracted data and analysis of these images do not present any unexpected results, providing a visual and graphical basis for how calcein fluorescence changes during a moderately long acquisition period.
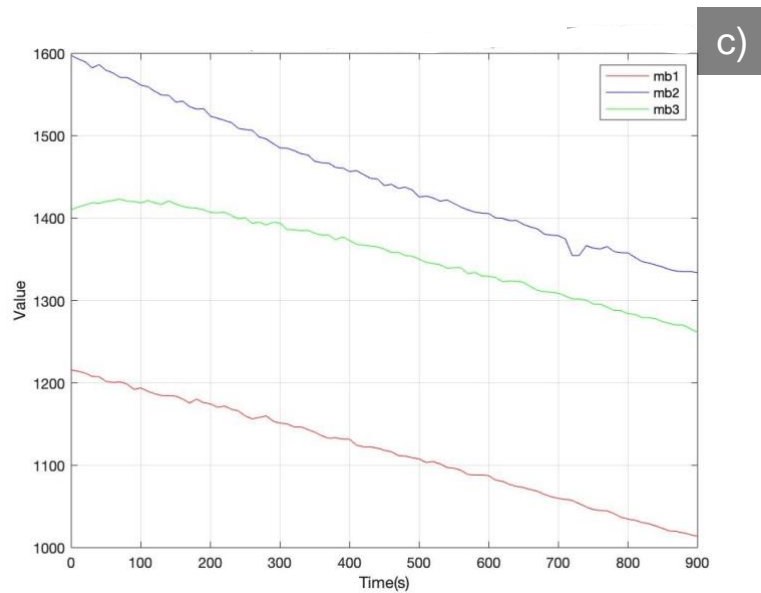
Figure 3.1: In images (a) and (b), captured during the first day of acquisition, we can see no considerable change between start and end of timelapse acquisition. In (c) we can see a minor decrease of the average fluorescence intensity over time (photobleaching).

With regard to the average fluorescence values obtained through analysis with ImageJ Fiji, it was noted on each day that the ROI acquisition algorithm worked with great precision and efficiency (Figures 3.2). This confirms that the images were successfully processed, thus resulting in high reliability.
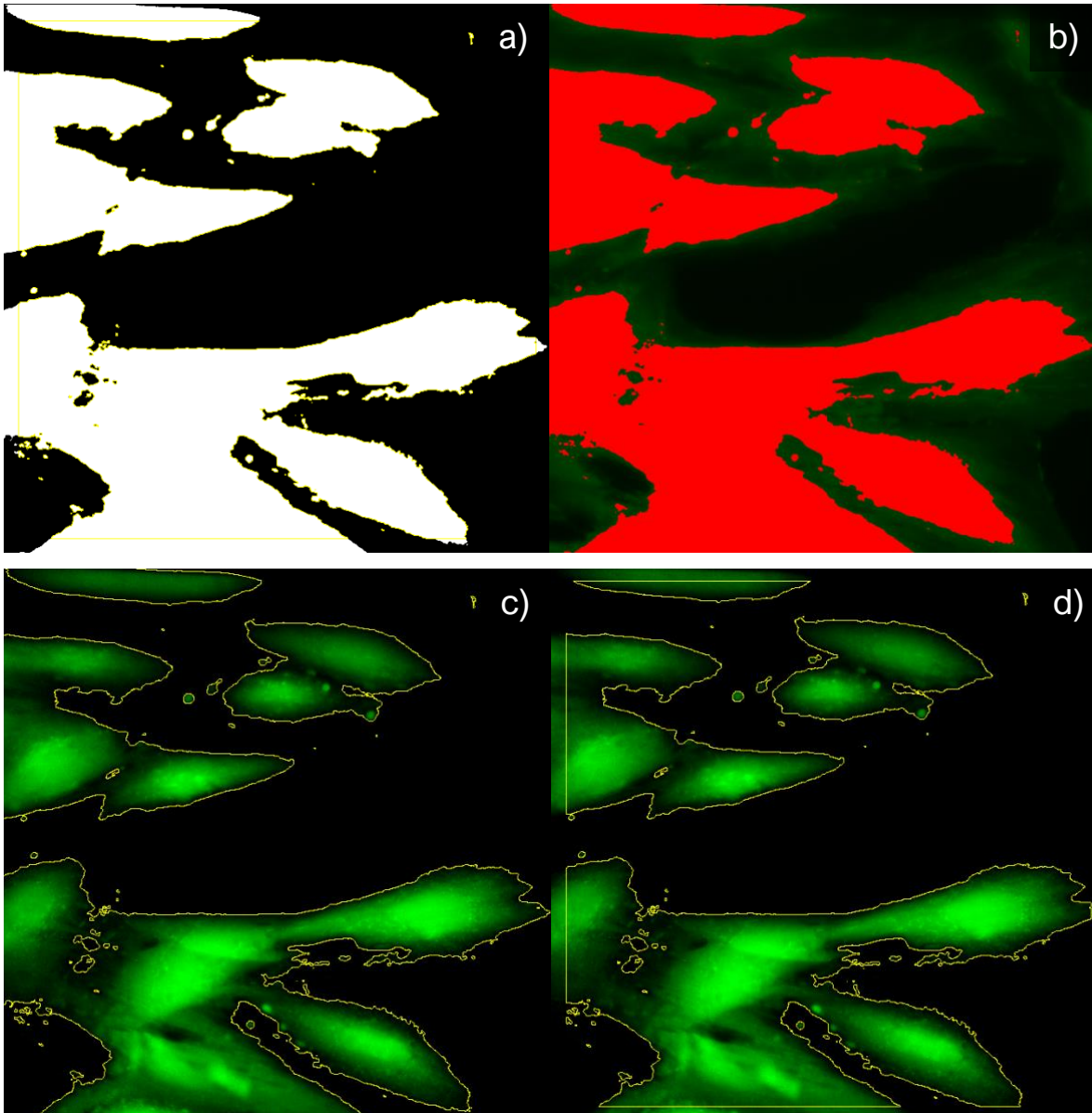

Figure 3.2: In this figure the automatic determination of the ROI in ImageJ Fiji is shown. The mask obtained after image thresholding (a), layed over the fluorescence image (b), the ROI determined based on the mask (c), and the final ROI with removed regions around the edges of the image, adapted to improve accuracy (d).

As can be seen from Figure 3.1, the initial fluorescence values varied notably between the three acquisitions. This can be related to expected variations in the way how individual samples became stained with calcein, as well as how much of the background in between the cells was captured within the ROI. The latter unavoidably varies between the samples, since each sample has cells that are positioned differently.

To correct for these variations, we subtracted the initial fluorescence value from all other values in the graph and consequently shifted all curves to 0 at time $t = 0$ s. The resulting graph is shown in Figure 3.3, where the fluorescence values obtained over the three days become much more comparable. All show a similar decreasing trend, and the slopes of the curves are consistent with each other, indicating a constancy in the results and confirming the reliability of the analysis conducted.
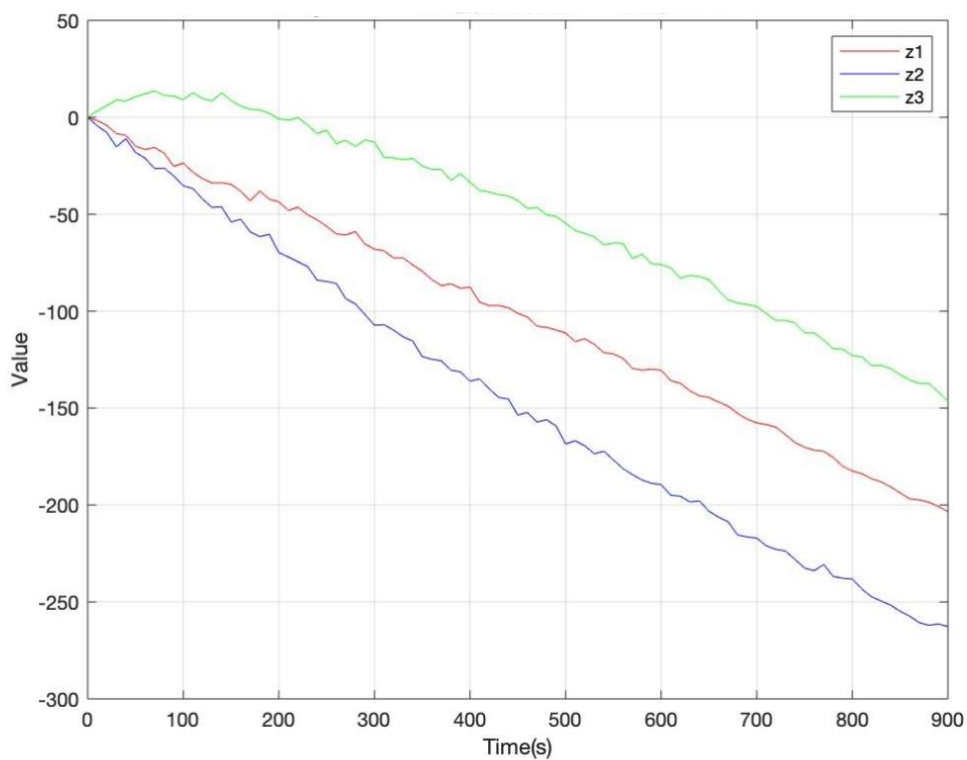

Figure 3.3: Plot of average intensity values from day 1 (red), day 2 (blue), and day 3 (green) in which the initial fluorescence value is subtracted from all other values, setting all graphs to 0 as starting point.

Figure 3.4 shows the graph of the average and standard deviation of the three curves from Figure 3.3. The graph clearly demonstrates good reproducibility of the experiments. This observation is crucial to confirm the validity of the acquisitions and the accuracy of the analysis process conducted. The small but gradual increase in the standard deviation observed over time is mainly the consequence of shifting all curves to zero at time $t = 0$ s, for which the differences between the curves are the smallest at the beginning.
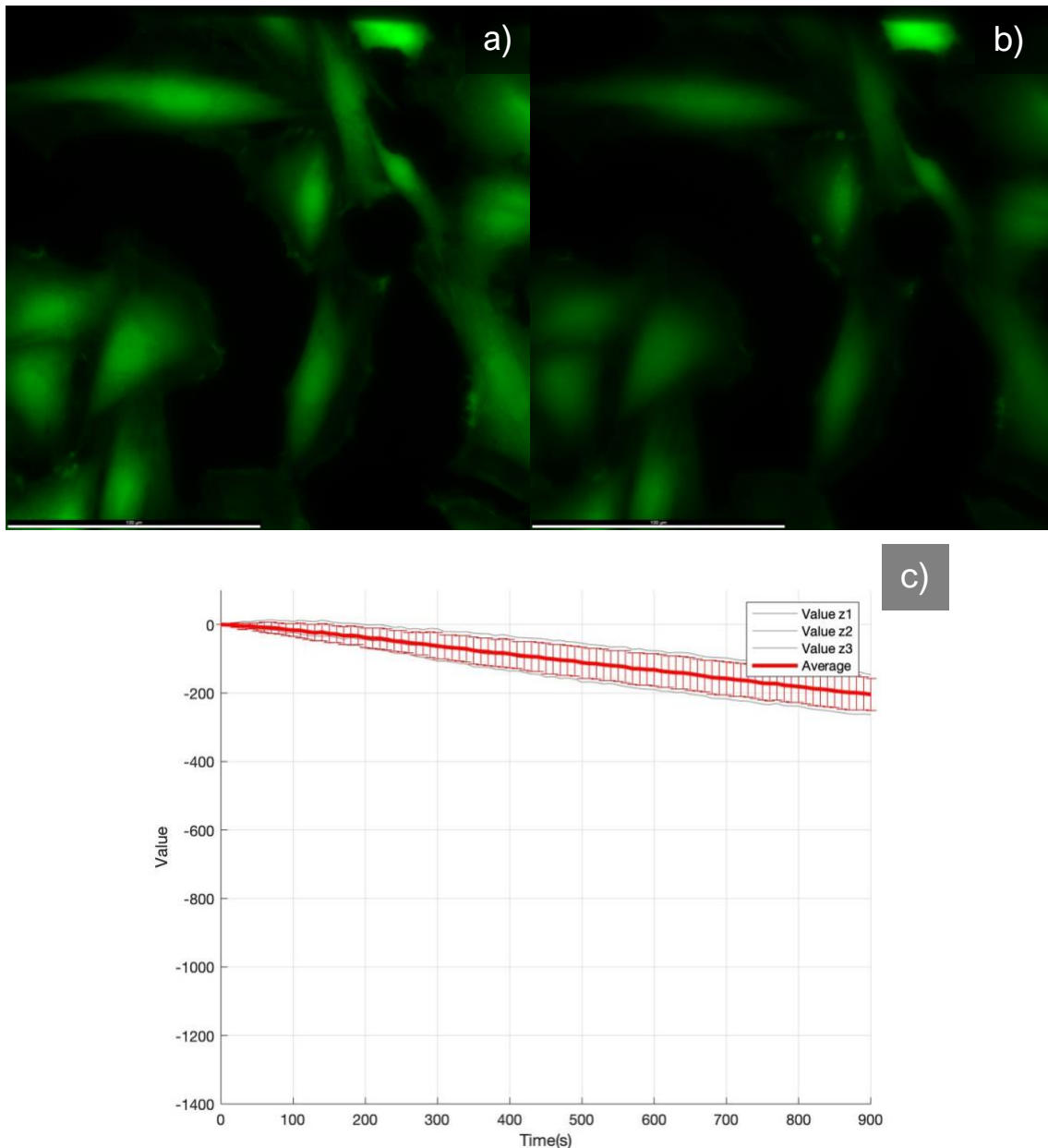

Figure 3.4: In figures (a) and (b) we can see day 2 of 0 V acquisition at start and at finish of acquisition and in (c) the graph of average value of acquisition performed on all three days and the corresponding standard deviation.

3.1.2. SAMPLES EXPOSED TO 200 V

In the acquisitions obtained at 200 V, as shown in Figures 3.5a and 3.5b, at the beginning and end of the timelapse respectively, the effects of electroporation-induced cell permeabilization begin to be observed. As the membranes become permeabilized, the calcein dye leaks out from the cells and the cell fluorescence decreases. The effect of electroporation is illustrated also in Figure 3.5c, which shows that the average fluorescence intensity curves have a steeper downward trend compared to control acquisitions at 0 V. The acquisition obtained on day 2 requires further attention, as it shows a considerably steeper decrease in fluorescence intensity values with respect to the values obtained on the other two days. It is essential to examine whether the image processing algorithm has introduced systematic errors or whether the experimental conditions have undergone uncontrolled changes that may have influenced the results.
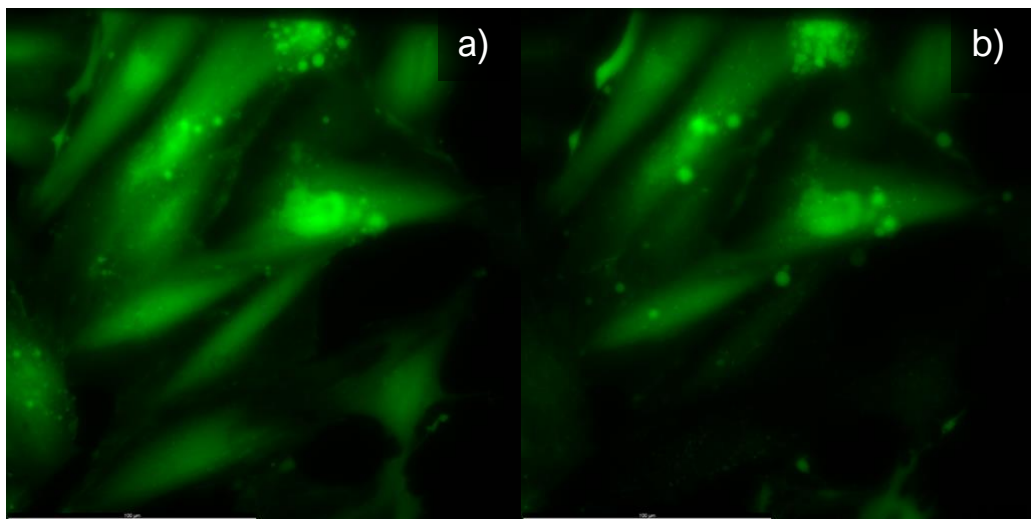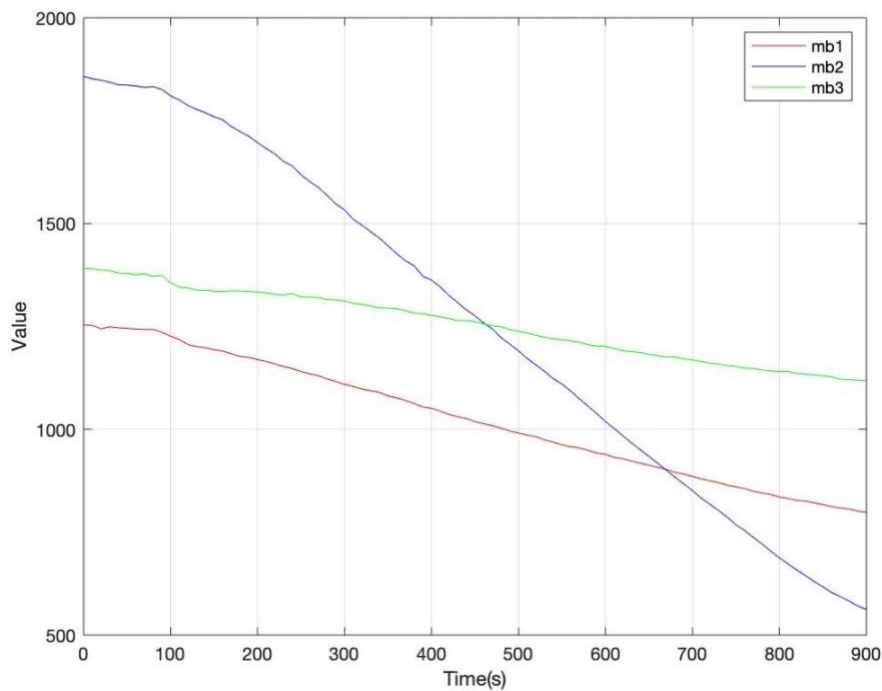
Figure 3.5: In acquisitions before (a) and after (b) electroporation we can start to see visually a decrease in intensity of fluorescence, while in (c) we can notice that intensity in day 2 is much higher compared to day 1 and day 3.

Visualizing the different frames of the time-lapse acquired on day 2, it can be clearly observed that the intensity in the frames shown in Figure 3.6a (before electroporation) and Figure 3.6b (two minutes after electroporation) is considerably higher than in the frames shown in Figure 3.6c and Figure 3.6d, acquired towards the end of the experiment.

This confirms a significant change in fluorescence intensity during the acquisition period. Additionally, the fluorescence imaged reveals formation of small bright spots after pulse application. These are most likely small vesicles that were formed due to electroporation and will be discussed in greater detail in subsequent sections.
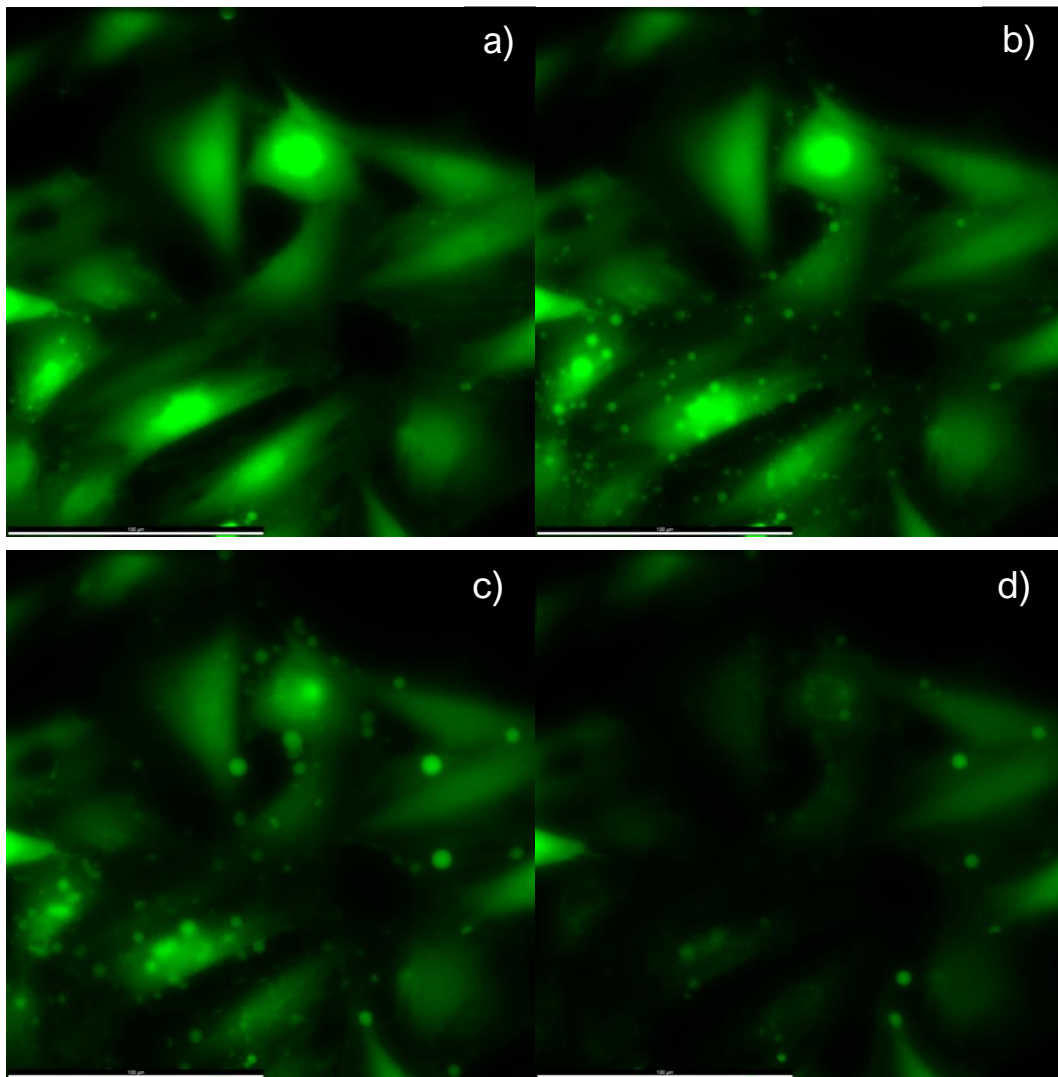
Figure 3.6: Different frames of the 200 V acquisition on day 2, respectively at t = 0 s (a), 2 minutes after electroporation (b), 8 minutes after electroporation (c), and at the end of acquisition (d).

Regarding the image processing algorithm, it can be stated with certainty that the images from day 2 were processed accurately. The masks shown in Figure 3.7a and 3.7b correctly identify the areas of interest, and the final ROI depicted in Figure 3.7d does not exclude any bright areas or any regions of potential interest. This confirms that the data extraction process had no errors. Therefore, the steeper decrease in fluorescence on day two can be attributed greater outflux of the calcein dye.

It is interesting to note that the cells in the sample from day 2 had a considerably higher initial florescence intensity compared with samples from day 1 and 3.

The reason for this could be, for example, slightly longer staining of the cells on day 2 and consequently greater intracellular calcein concentration. Greater calcein concentration within the cells means a greater concentration gradient across the membrane and consequently greater calcein outflux from the cells, explaining at least partially the greater decrease in fluorescence.

Additionally, the cells on day 2 might have become permeabilized more due to more extensive electroporation, further contributing to the greater calcein outflux. Whether greater intracellular calcein concentration is in any way connected to more extensive membrane permeabilization cannot be answered from our limited number of experiments but would be interesting to explore in the future.
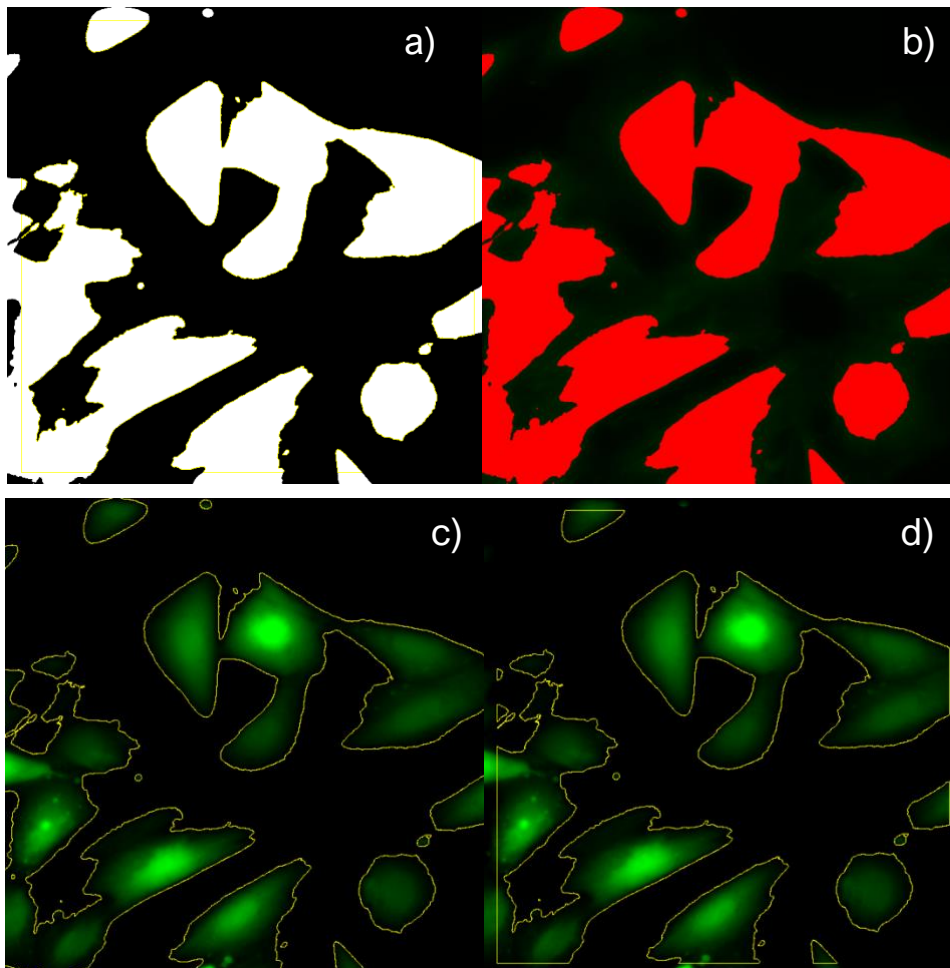

Figure 3.7: In this series of pictures, we can observe how the image processing algorithm worked on the timelapse from day 2 starting from the masks (a-b) to the identification of first ROI (c) and reduced ROI (d).

After ascertaining that the data from all three days is reliable, we proceeded with analyzing the results in a similar way as done above for control samples. We first shifted the initial point of each curve to 0 and (Figure 3.8), and then calculated the mean and standard deviation of all three curves (Figure 3.9). From Figure 3.8 it can be again clearly seen that the values acquired on day 2 show a more pronounced decrease in fluorescence values than on days 1 and 3.

Figure 3.8 thus further reveals the variation that can be observed from one experimental repetition to another. Such variation is quite common in experiments with biological cells including electroporation experiments. This variation is reflected in the large standard deviation from the mean of the three curves, shown in Figure 3.9. Nevertheless, the general behavior of all three curves is fully consistent.
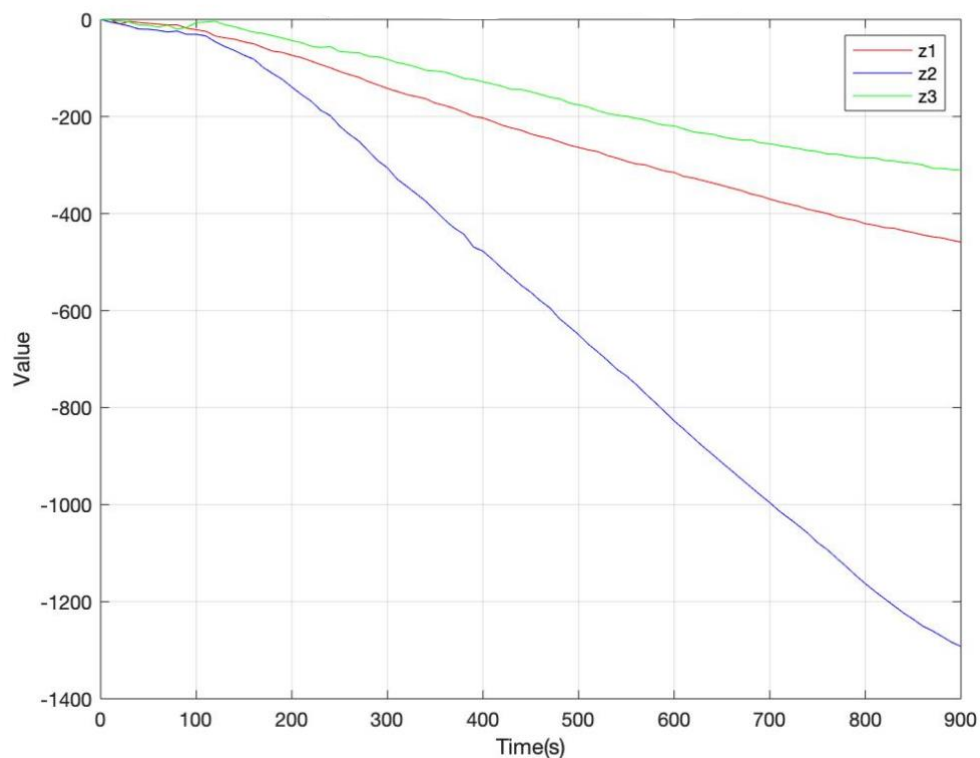

Figure 3.8: Plot of average intensity values from day 1 (red), day 2 (blue) and day 3 in which all values are subtracted by the first average intensity value acquired, setting all graphs to 0 as starting point.
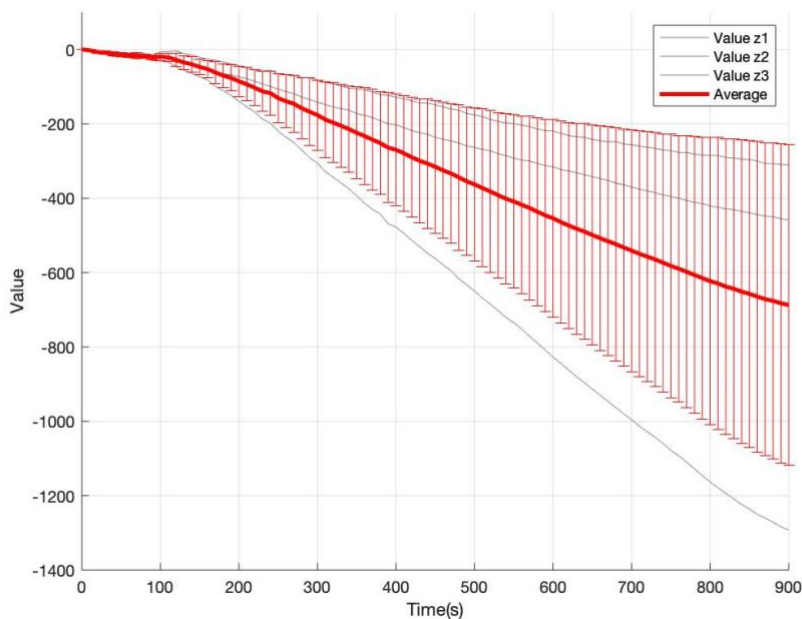
Figure 3.9: Graph of the average and standard deviation of all 3 curves obtained at 200 V on different days of acquisition.

3.1.3. SAMPLES EXPOSED TO 400 V

The acquisitions obtained when exposing the cells to 400 V resemble that acquired when exposing the cells to 200 V on day 2. As shown in Figure 3.10, the pulse not only evoked a visible and marked decrease in fluorescence intensity, but also the formation of small vesicles. Prior to conducting these experiments, the phenomenon of vesiculation had not been considered, as a gradual decrease in intensity due to the escape of calcein dye from the cells was simply expected.

Vesiculation can, for example, be induced using specific reagents that affect the cell membrane and cause the formation of blisters and vesicles [61]. In the present case, we are dealing with an example of stress-induced vesiculation[62], where the stress is caused by the exposure to electric pulses and electroporation. Already two minutes after the pulse exposure (Figure 3.10b), a considerable number of vesicles is observed. This suggests that the integrity of the membrane was rapidly compromised, leading to the leakage of calcium as well as other intracellular substances and the formation of vesicles.
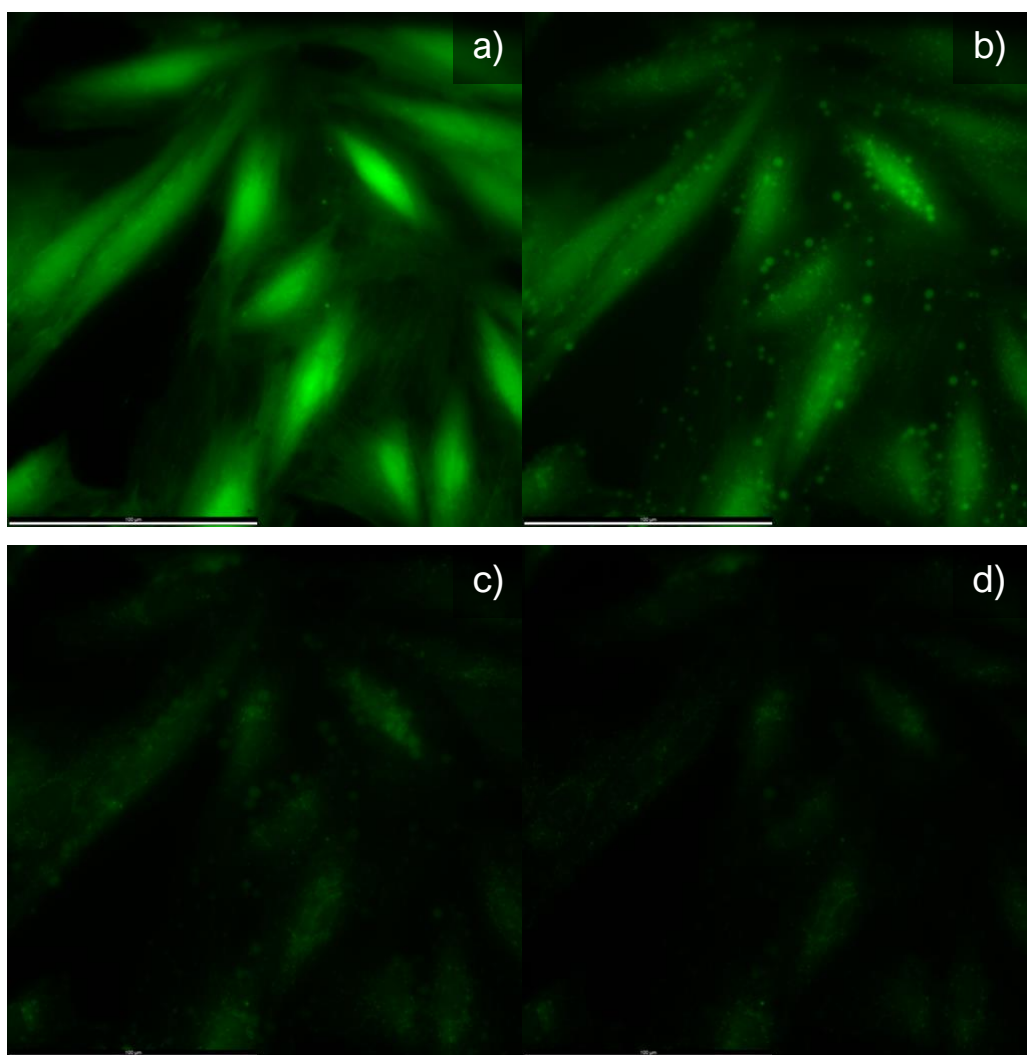
Figure 3.10: Different frames of the day 1 acquisition at 400 V, respectively at t = 0 s (a), 2 minutes after electroporation (b), 8 minutes after electroporation (c) and at the end of acquisition (d).

As can be deduced from the graph in Figure 3.11c, even in the case of the 400 V acquisitions, the acquisition on day 2 shows higher fluorescence intensity compared to days 1 and 3.

After a check of the feature extraction algorithm and an examination of the images in Figure 3.11a (before electroporation) and Figure 3.11b (after electroporation), it can be concluded that, as in the previous case, the cells simply had a grater intracellular calcein concentration.

Of particular interest is Figure 3.11b, where it is possible to observe the specific distribution of vesicles and how their presence also highlights the nuclei of the cells themselves.
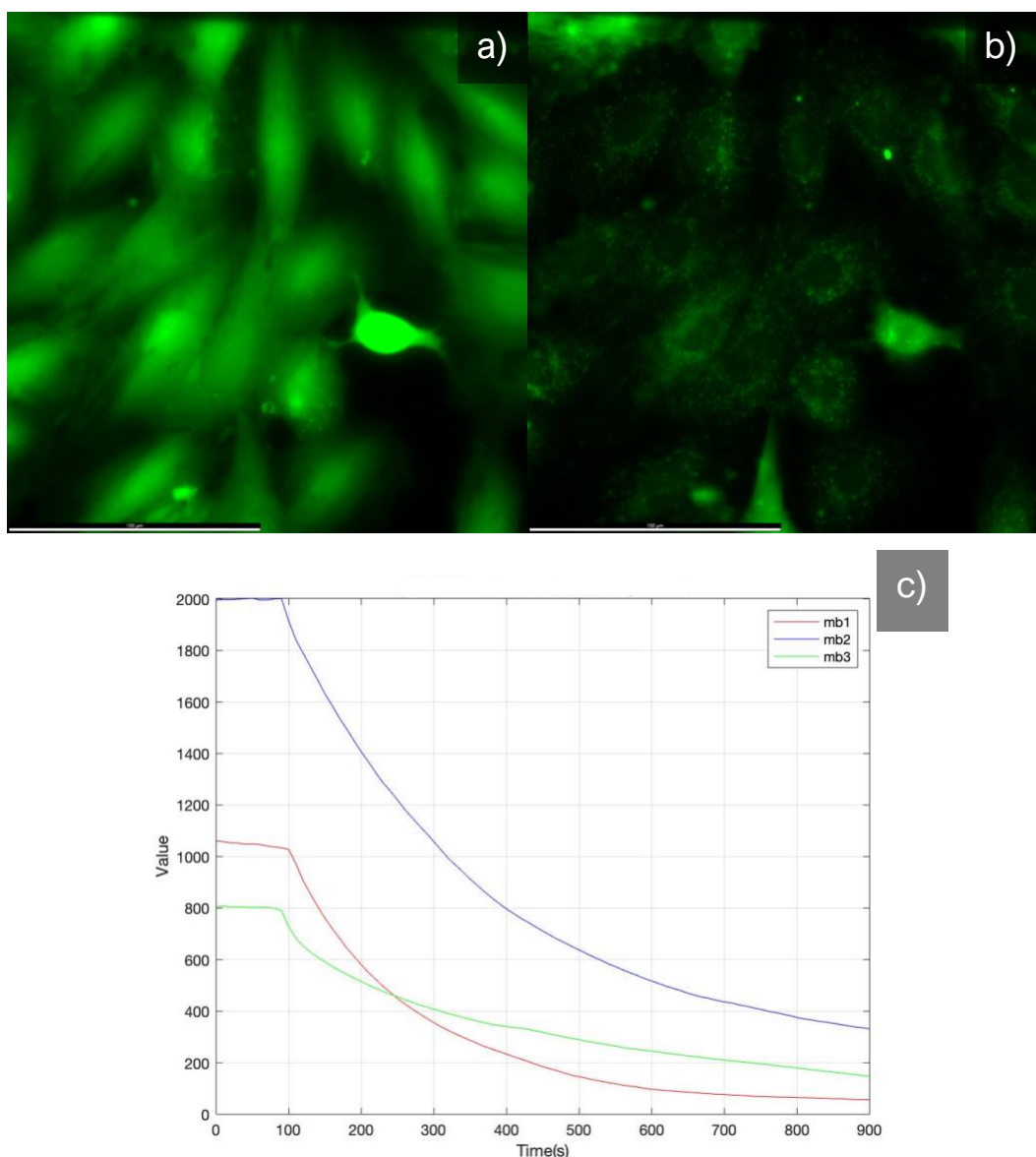
Figure 3.11: Frames before electroporation (a) and after (b) electroporation of day 2 acquisition and graph of average intensity value in day 1 (red), day 2 (blue) and day 3 (green).

The graph showing the fluorescence intensity curves obtained on each of three days after shifting the initial point of each curve to 0 is shown in Figure 3.12, whereas the mean and standard deviation of all three curves is shown in Figure 3.13. Similar trends and characteristics as in the 200 V acquisitions can be observed. However, in both figures, just after the pulse exposure (t = 90 s) there is a small peak in intensity.

This peak can be explained by the rapid formation of numerous very bright vesicles immediately after electroporation, which temporarily bring the average intensity to higher values than the initial ones, and then continue with the normal decay.
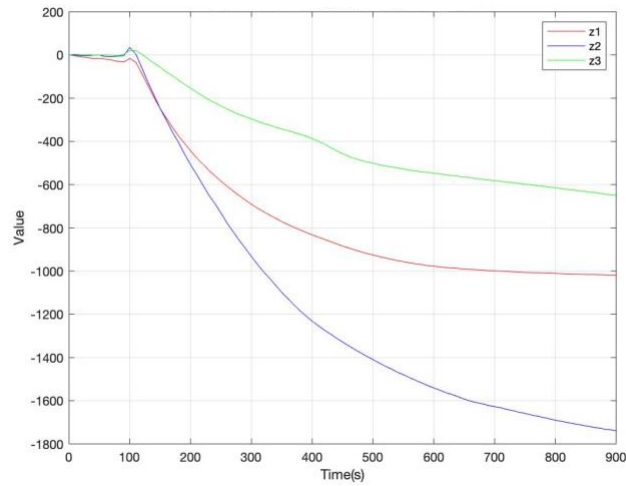
Figure 3.12: Average intensity of fluorescence after being set to zero in day one (red), day 2 (blue) and day 3 (green).
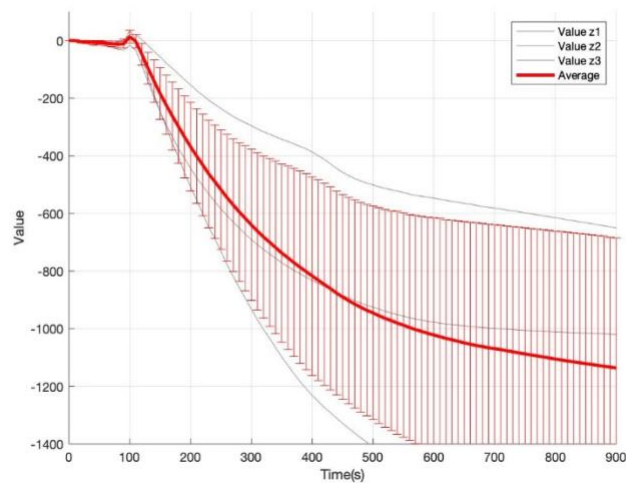
Figure 3.13: Graph of the average and standard deviation of all 3 curves obtained at 400 V on different days of acquisition.

3.1.4. SAMPLES EXPOSED TO 600 V

Analyzing the results obtained at 600 V, vesiculation, already observed at 400 V, is further accentuated with increasing voltage. As shown in Figures 3.14a to 3.14d, this phenomenon leads, in the time following the pulse exposure, to the reveal of vesicles of different sizes. After observing this phenomenon in the previous experiment at 400 V, this observation could suggest

that vesicles are naturally present in the cells, in which they are stained like all the rest of the cell, but following the pulse exposure all the calcein inside the cells gets out of the cell themselves, meanwhile vesicles remain intact and are successively shown.

However, this conclusion is partial as the images acquired are two-dimensional and do not consider the thickness of the cell, but only its length and height. In the specific case of a cell such as H9c2, which has an elongated shape and increased thickness around the nucleus, the tendency to observe vesicles around the nucleus can lead to different interpretations.
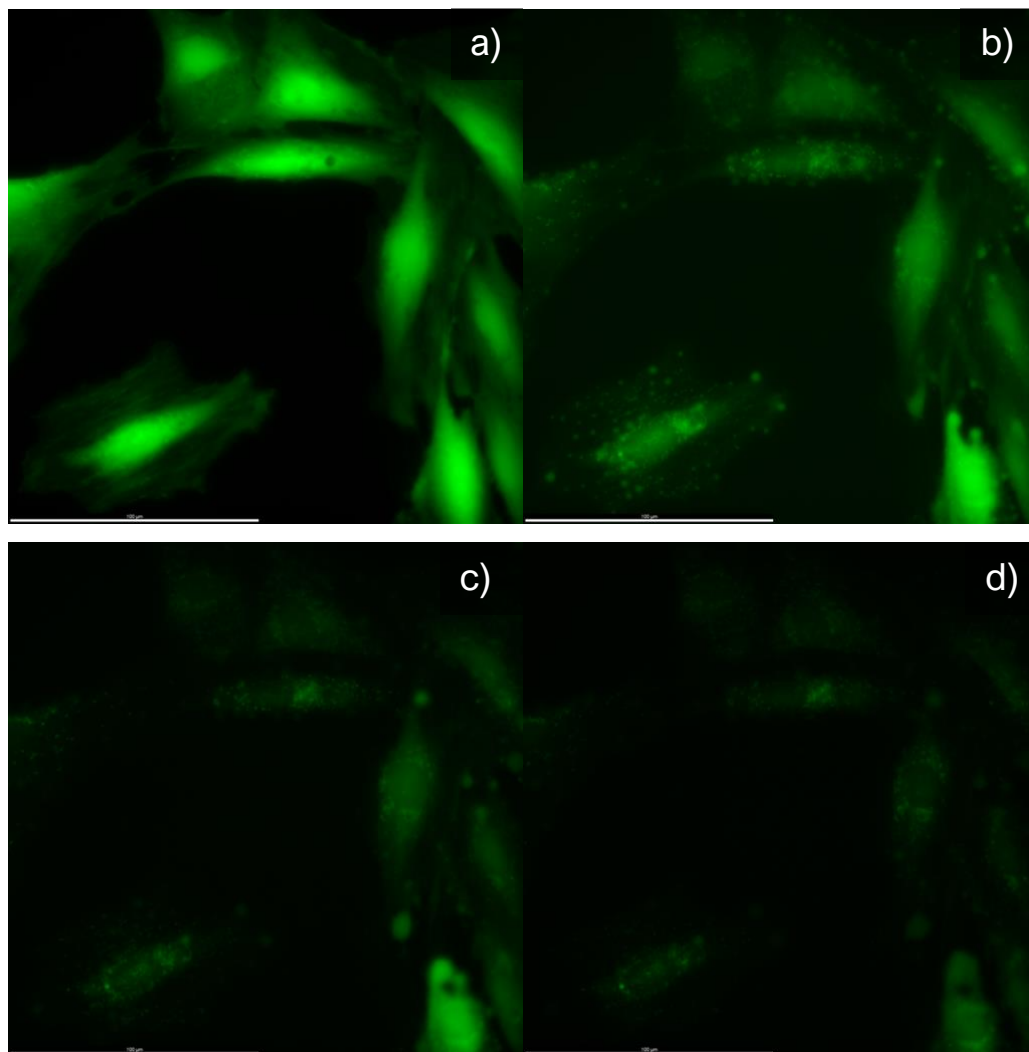

Figure 3.14: Different frames of 600V acquisition on the day 2, respectively at t = 0 s (a), 2 minutes after electroporation (b), 8 minutes after electroporation (c) and at the end of acquisition at 13 minutes and 30 second after electroporation (d).

It is useful to examine the effect of electroporation on the cells on day 3. In Figures 3.15a and 3.15b, it appears that some cells completely excrete calcein after discharge, while others appear to be only slightly affected, i.e. they exhibit vesicles and maintain a high fluorescence intensity. This phenomenon can be explained by considering that all cells were subjected to electroporation under the same conditions, but their different sizes, orientation, and proximity to other cells led to different electroporation outcomes.

After setting the initial value of the curves to zero (Figure 3.16a) and calculating the mean and standard deviation of all three curves (Figure 3.16b), a similar behavior is observed as with 400 V, but with lower standard deviation indicating greater reproducibility of the results at higher applied voltage (Figure 3.16b).

Figure 3.15: Frames before (a) and after (b) electroporation of acquisition at 600 V on day 3 and graph of average intensity value in day 1 (red), day 2 (blue) and day 3 (green).

69
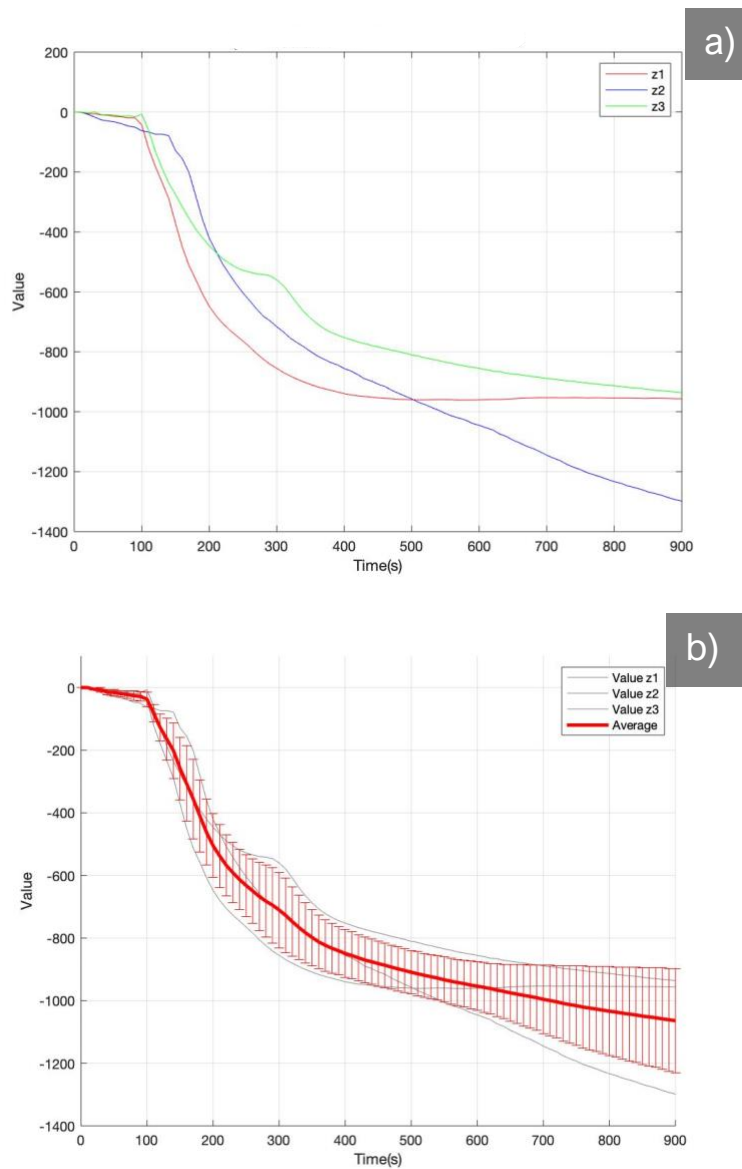
Figure 3.16: Average intensity of fluorescence after being set to zero in day one (red), day 2 (blue) and day 3 (green) and graph of all three curved averaged with their standard deviation (b).

3.1.5. SAMPLES EXPOSED TO 800 V

Finally, the results obtained with 800 V were consistent with those obtained with lower voltages. A highly consistent response to the pulse exposure is observed, followed by a rapid decrease in fluorescence intensity. In addition to that, as seen in previous acquisitions, there is a clear revelation of the vesicles inside the cell in the moment after the electroporation phase 2 minutes after pulse exposure (Figure 3.17b), leading to almost an absence of calcein inside the cells and

to an even stronger revelation of vesicles present inside the cells. This almost complete leak out of calcein is most likely due to the increased voltage, which caused more damage to the cell membrane and faster leakage.
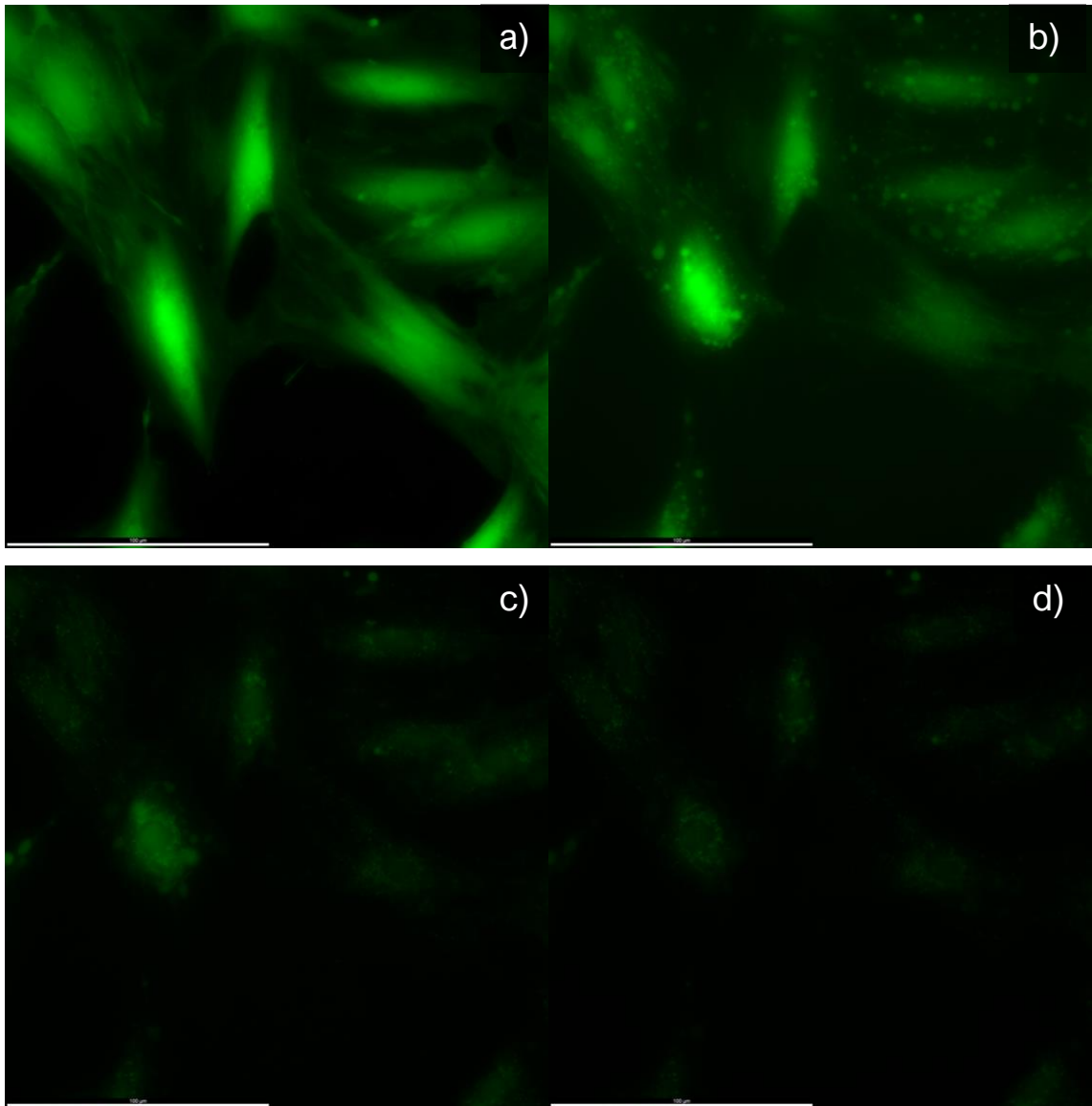
Figure 3.17: Different frames of the acquisition at 800 V on day 3, respectively at t = 0 s (a), 2 minutes after electroporation (b), 8 minutes after electroporation (c) and at the end of acquisition at 13 minutes and 30 seconds after electroporation (d).
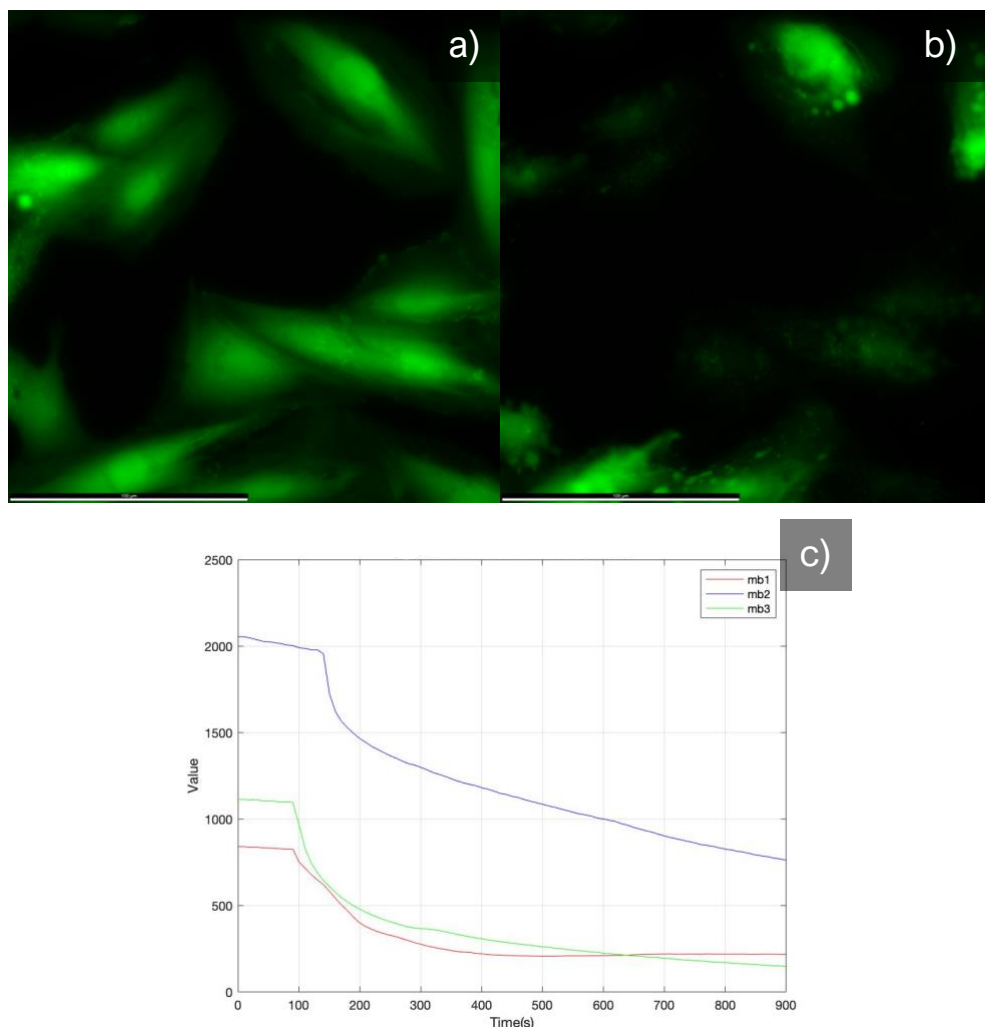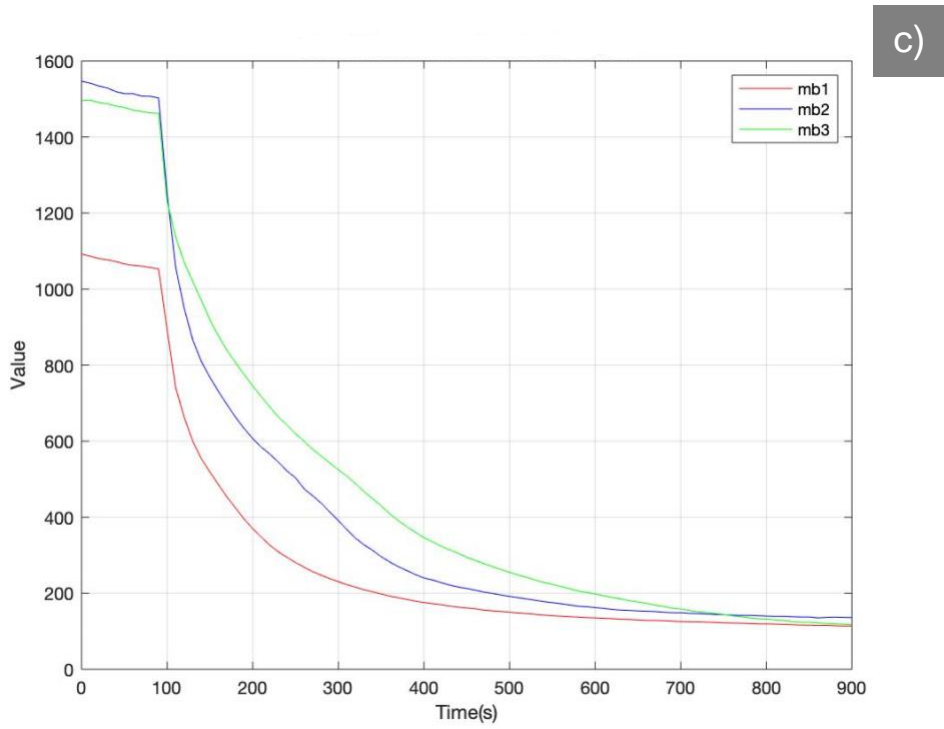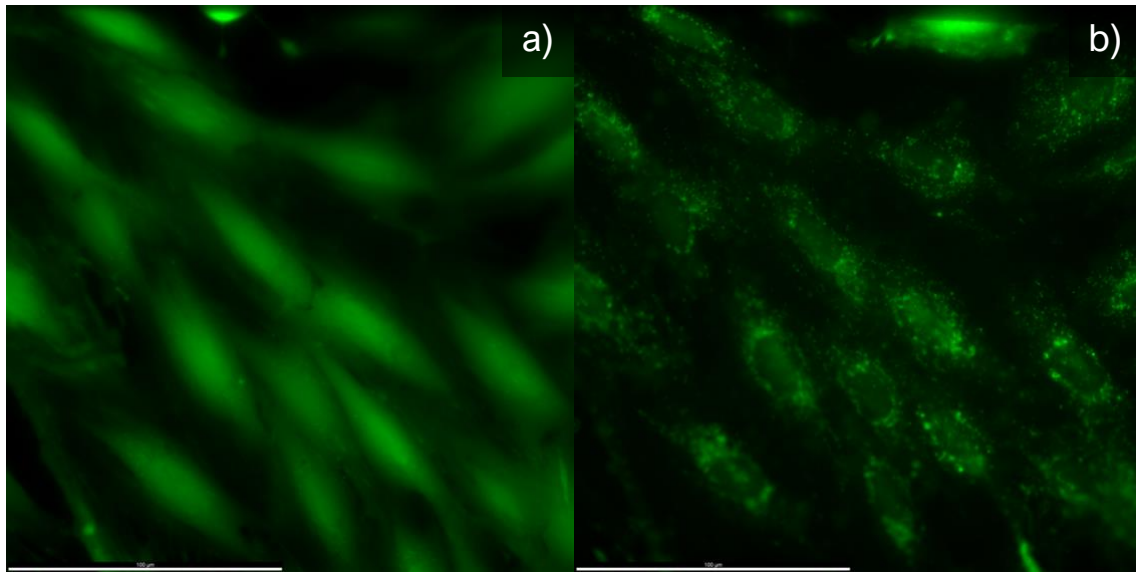
Figure 3.18: Frames before (a) and after (b) electroporation of day 3 acquisition and graph of average intensity value in day 1 (red), day 2 (blue) and day 3 (green).

When setting their initial point to zero, the curves in Figure 3.19 show comparable values and behavior with a clearly delineated and defined trend, with small standard deviation.
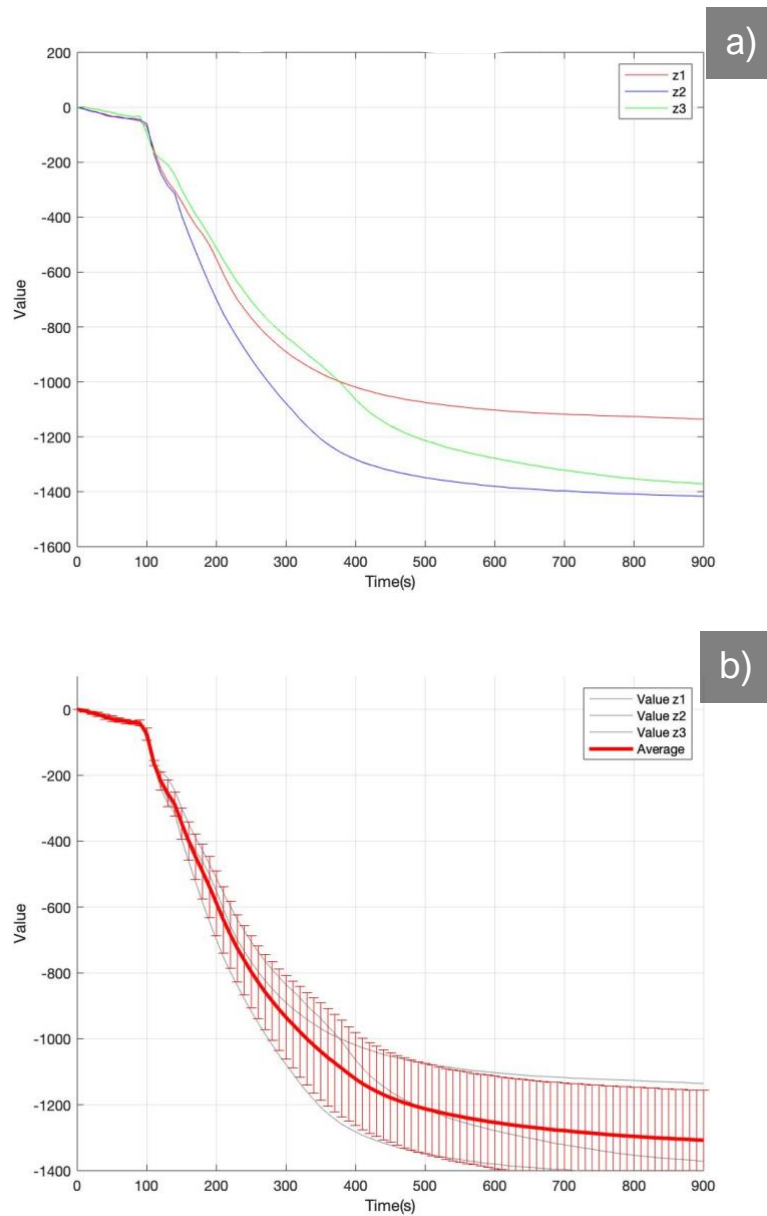
Figure 3.19: Average intensity of fluorescence after being set to zero in day one (red), day 2 (blue) and day 3 (green) (a) and graph of all three curves averaged with their standard deviation (b).

3.2. ANALYSIS OF GRANULATION

After analyzing the average intensity and fluorescence and evaluating some of the consequences of electroporation, we continued with the analysis of the granularity characteristics of the cells during the acquisition period. Of all 16 available granularity spectra, only the first three were selected and sampled, as they provide more information on the revelation of small vesicles in the form of granules.

3.2.1 OVERVIEW OF DATA OBTAINED

We start with the first granularity spectrum (GS1) values obtained with the control sample at 0 V, to provide an important reference for future analyses at various voltages (Figure 3.20). After plotting these results, we started with the analysis of the data obtained from GS1 at various voltages. The values shown in Figure 3.21 are illustrative of a gradual increase as the timelapse progresses. Some features of the curve can be observed in Figures 3.21c and 3.21d, where, at approximately the time point at which electroporation occurs, a significant peak in the GS1 value is observed.

This is evidently because, with pulses of higher voltages, vesicles revelation occurs much more rapidly, as calcein leaks out of the cell faster, leading to peaks in the measured values. In the case of Figure 3.21c, this also leads to a plateau phenomenon towards the end of the acquisitions, which is understandable if nearly all the calcein went out from the cells.
In general, we can say that all the GS1 values are comparable both in terms of absolute values, showing a general increase in the spectrum as the intensity of the discharge increases, and in terms of similar values with the same pulse exposure, but on different days.

This suggests consistency and repeatability of the results obtained, confirming the effectiveness of the analysis method adopted.

Figure 3.20: Control acquisition of GS1 values in time (0 V acquisition).

Figure 3.21: GS1 values in time at different voltages for 200 V (a), 400 V(b), 600 V(c) and 800 V (d) delivery.
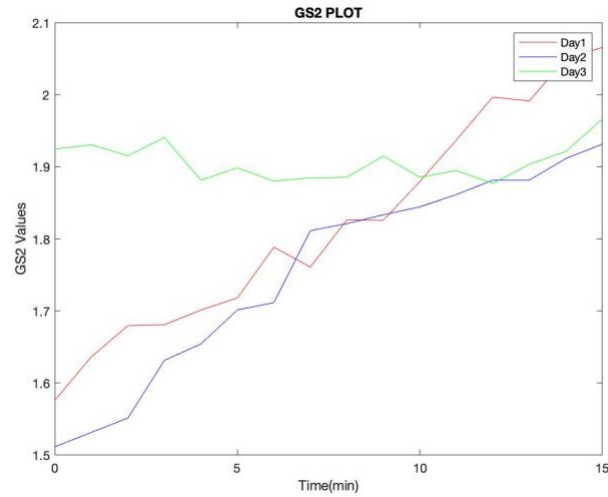
Figure 3.22: Control acquisition for GS2 values in time (0 V acquisition).

While analyzing the GS2 values, a trend emerges in the curves from the different days which, although similar, is less aligned than in the case of GS1. However, all GS2 values show a positive trend, which is most profound at the highest applied voltages. Again, a plateau is observed in the GS2 values for 600 V (Figure 3.23c) and 800 V (Figure 3.23d) towards the end of acquisition.
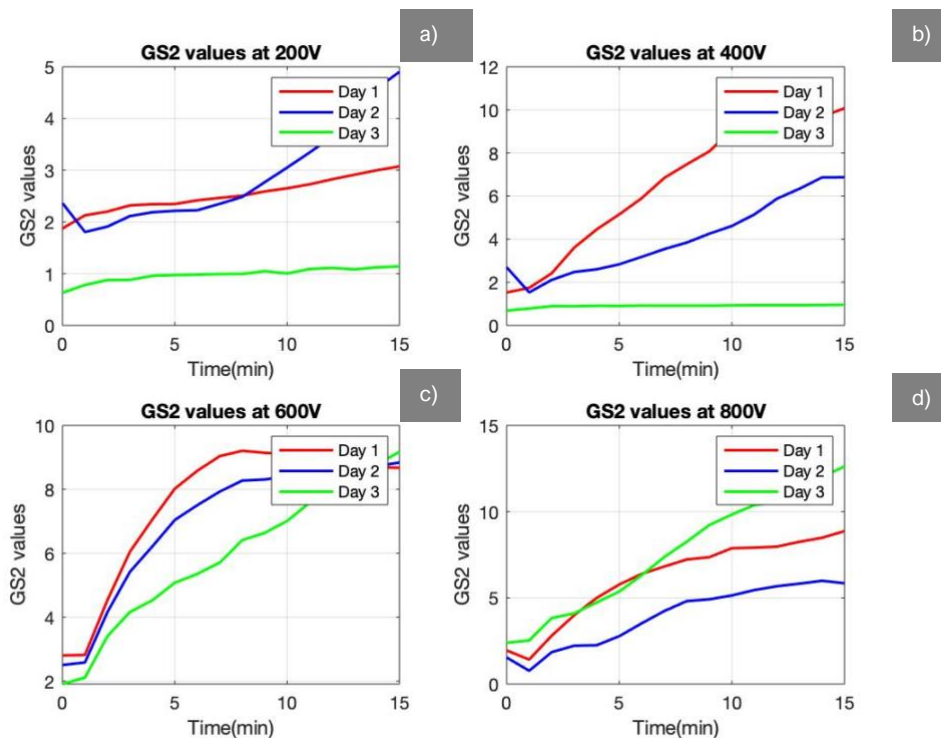
Figure 3.23: GS2 values in time at different voltages for 200 V (a), 400 V(b), 600 V(c) and 800 V (d) delivery.

Finally, we analyze the last granularity spectrum considered, namely GS3. In this case, the GS3 values show a different trend to that observed in the previous GS1 and GS2 spectra. While 600 V and 800 V the value of GS3 increases with time, at 200 V and one curve at 400 V (on day 3) we first see an increase followed by decrease. This possibly reflects the formation of larger vesicles that appear shortly after the pulse exposure and then disappear as the time progresses (see Figure 3.6).

Such transient appearance of larger vesicles, that probably form as a consequence of the stress response to electric pulses, can be seen by visual inspection of the captured image sequences. At higher voltages, when most of the calcein leaks out from the cells, vesicles that have likely been present within the cells even before the pulse application become revealed in addition to the vesicles formed as stress response. Since all these vesicles can have comparable sizes, the granularity spectrum GS3 ends up monotonically increasing. Nevertheless, it should be stressed that this interpretation is speculative and will require further analysis using different methods.
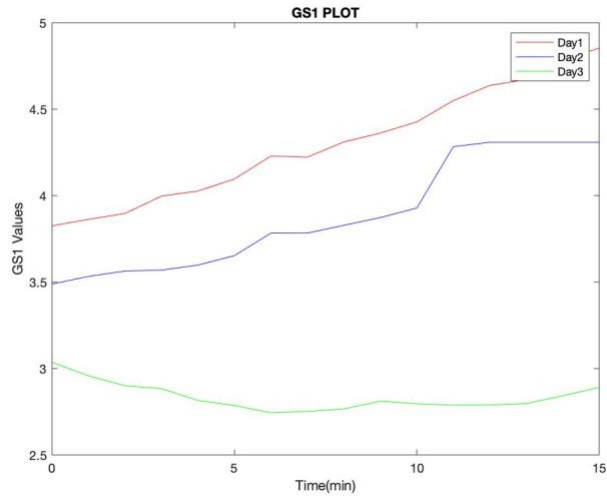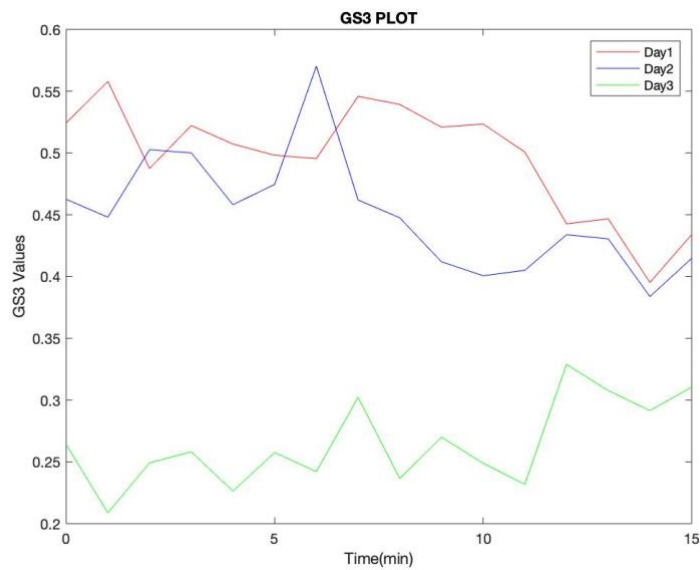

Figure 3.24: Control acquisition for GS3 values in time (0 V acquisition)
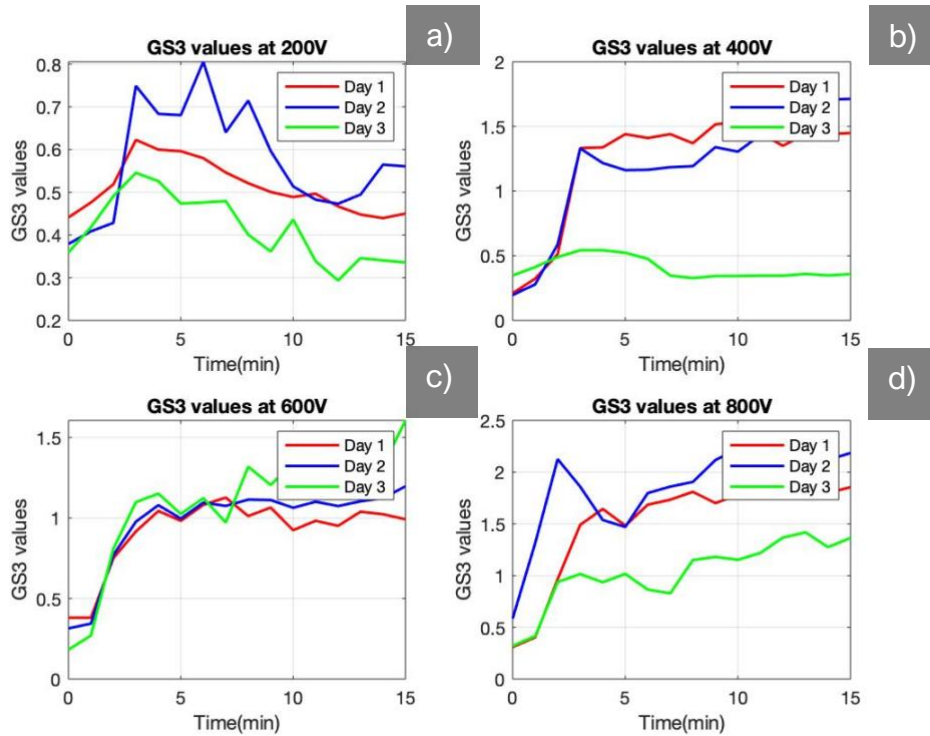
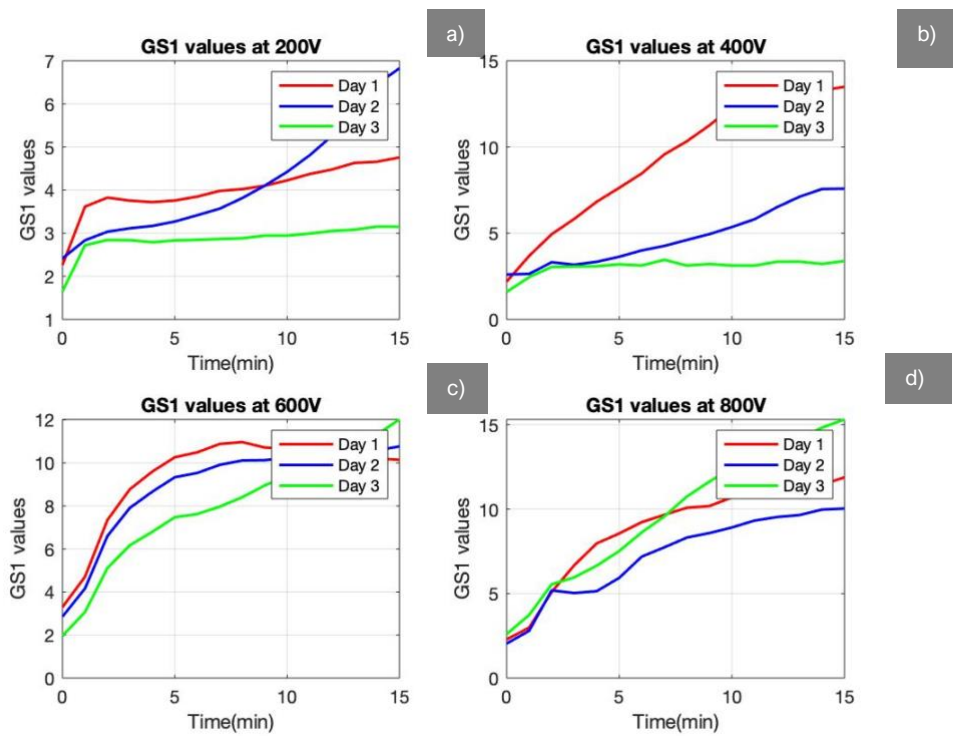**Figure 3.25:** GS3 values in time at different voltages for 200 V (a), 400 V(b), 600 V(c) and 800 V (d) delivery.

3.2.2. SAMPLES EXPOSED TO 200 V

This section will analyze the average granularity spectra of the three acquisition days (avg GS1, avg GS2 and avg GS3) at the same voltage.

Beginning with the analysis of the 200 V, Figure 3.26 shows how the curves of the mean GS1 and GS2 show a very linear trend and a progressive increase in the mean value over time. Furthermore, it is important to note that for both GS1 and GS2, the standard deviation is within acceptable values for a successful analysis.

The situation is different for GS3: the average curve shows a bimodal behavior with acceptable standard deviation, corroborating the interpretation discussed in the preceding section.
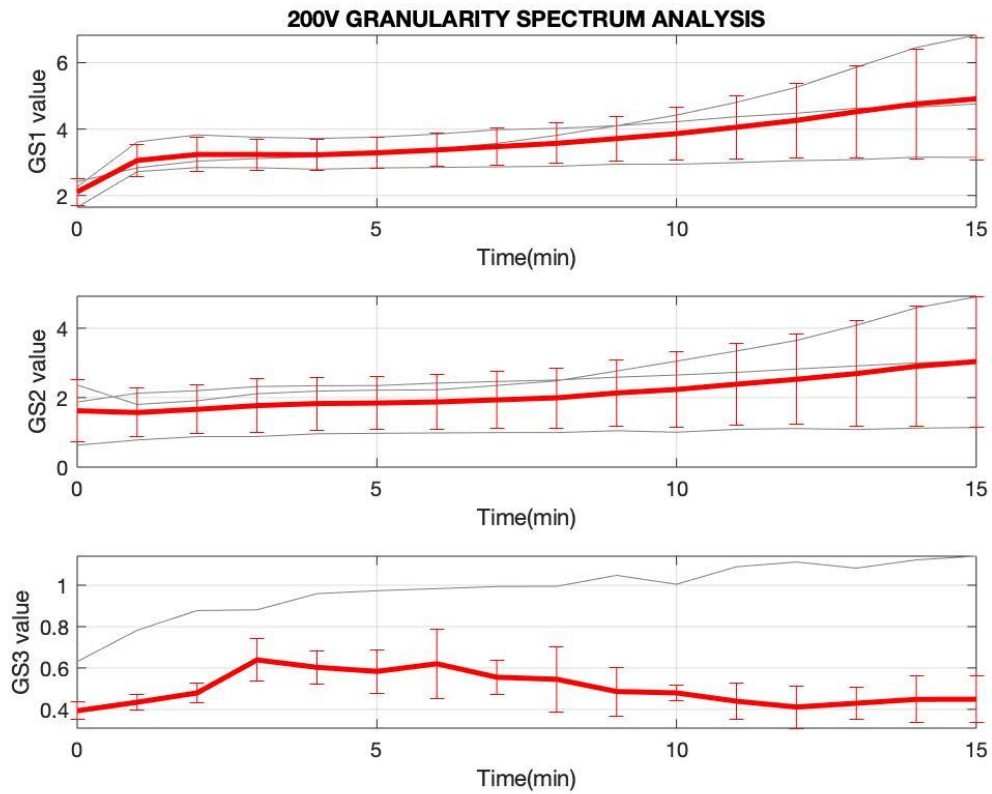
Figure 3.26: Analysis of average values of granularity spectrum at 200 V.

3.2.3. SAMPLES EXPOSED TO 400 V

Proceeding to the analysis of the average spectrum at 400 V, it can be seen that, similarly to the case at 200 V, the averages of GS1 and GS2 show a positive trend, with a standard deviation that is well within the acceptable range for these analyses. On the other hand, the trend of the average GS3 spectrum is different: after the application of the electric pulses, there is a significant increase in the values, followed by plateau after a few minutes. At 400 V, the averaged behavior of GS3 becomes more similar to that observed at higher voltages.
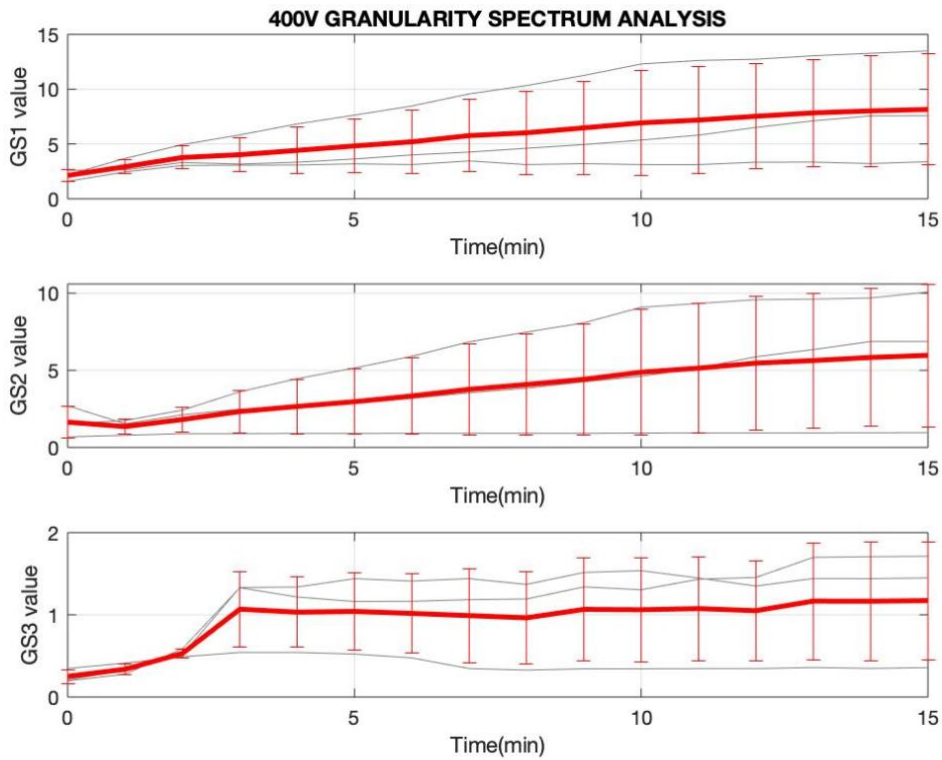
Figure 3.27: Analysis of average values of granularity spectrum at 400 V.

3.2.4 SAMPLES EXPOSED TO 600 V

As far as the analysis of the average granularity spectrum at 600 V is concerned, the trends of the averages of the GS1 and GS2 curves can be clearly delineated. They show low standard deviations, indicating good consistency between the different days of acquisition. The average of GS3 e also shows low standard deviation but its behavior is notably different from GS1 and GS2; it increases within the first few minutes after pulse exposure and then plateaus.
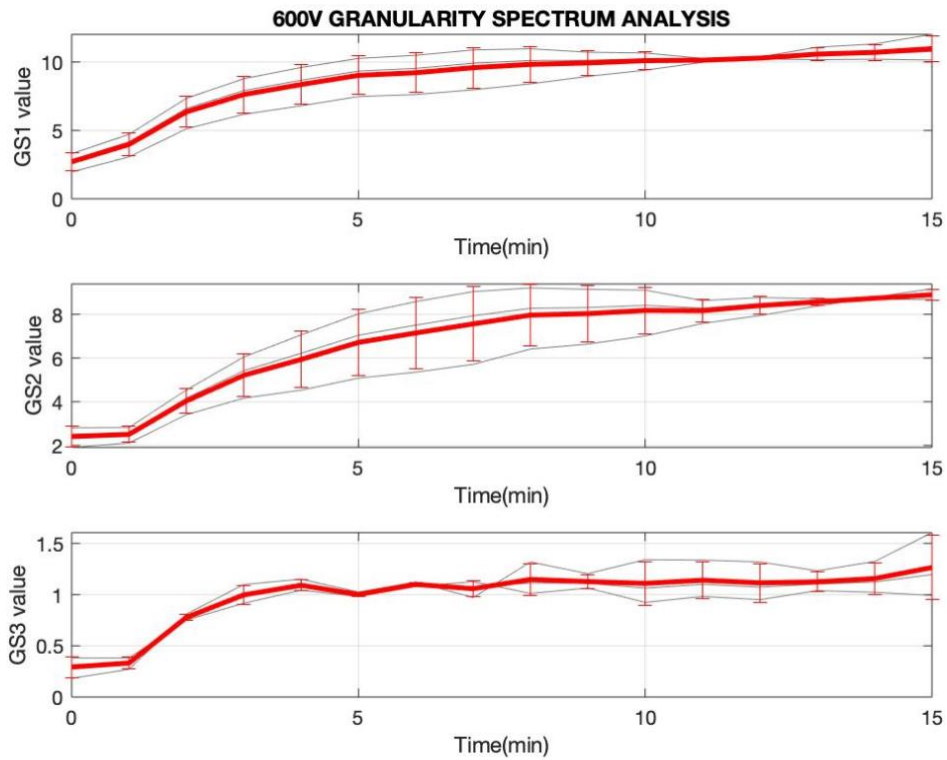
Figure 3.28: Analysis of average values of granularity spectrum at 600 V.

3.2.5 SAMPLES EXPOSED TO 800 V

Finally, we proceed to analyze the last granularity spectrum at the highest voltage delivered. Also, in this case we can see how avg GS1 and avg GS2 are in line with all we have seen precedingly and GS3 again increases in the first few minutes after the pulse exposure followed at then plateaus.
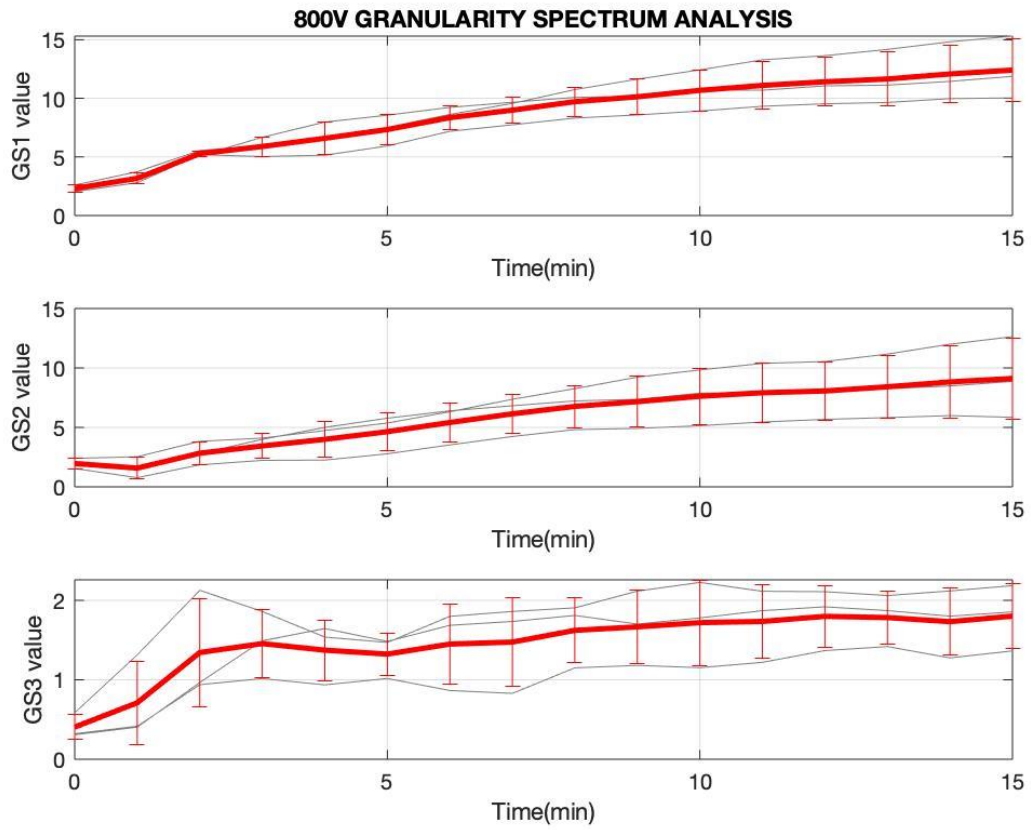
Figure 3.29: Analysis of average values of granularity spectrum at 800 V.

4 RECOMMENDATIONS FOR FURTHER INVESTIGATIONS

4.1. PRELIMINARY IMAGING WITH SUPER-RESOLUTION MICROSCOPE

In addition to the experiments conducted with the Leica Thunder fluorescence microscope, an experiment was performed using a Zeiss super-resolution microscope Elyra 7 SIM[2] to obtain a more detailed and clear view of the structures and behavior of H9c2 cells at the moments before, during and after electroporation. The aim was to validate and deepen the results of previous experiments, focusing particularly on visualizing the actual presence of the vesicles in three dimensions before pulse delivery using z-stack capabilities that can visualize everything inside the cell.

Samples for Zeiss super-resolution analysis were prepared similarly to previous experiments to ensure consistency and comparability of results. After trypsinization of the cells, a cell suspension with a density of 2.7×10^5 cells/ml was prepared. From this suspension, 7 µl (approx. 1900 cells) were pipetted into each well, ensuring an even distribution of cells for imaging and a cell confluency of 50% on the day of imaging.

High-resolution imaging with the Zeiss microscope provided important information on the intracellular dynamics and detection of vesicles after undergoing electroporation. By analyzing the z-axis of the cells, it was observed that some vesicles were already present inside the cells before the application of the electric pulses. This observation suggests that some of the vesicles are not formed solely because of electroporation but are pre-existing structures that become more prominent and detectable as the calcein leaves the cells. Super-resolution imaging also allowed a better view of the three-dimensional distribution of vesicles within the cells (Figure 4.2), providing a more detailed understanding of what is present within them and what a simple two-dimensional analysis cannot see.

However, the resolution of the images was not optimal, and we were unable to resolve larger transient vesicles formed due to the pulse exposure that were visible under the wide-field

fluorescence microscope, indicating that more efforts need to be made to adapt the sample preparation and imaging protocol. This a recommended next step for further studies.
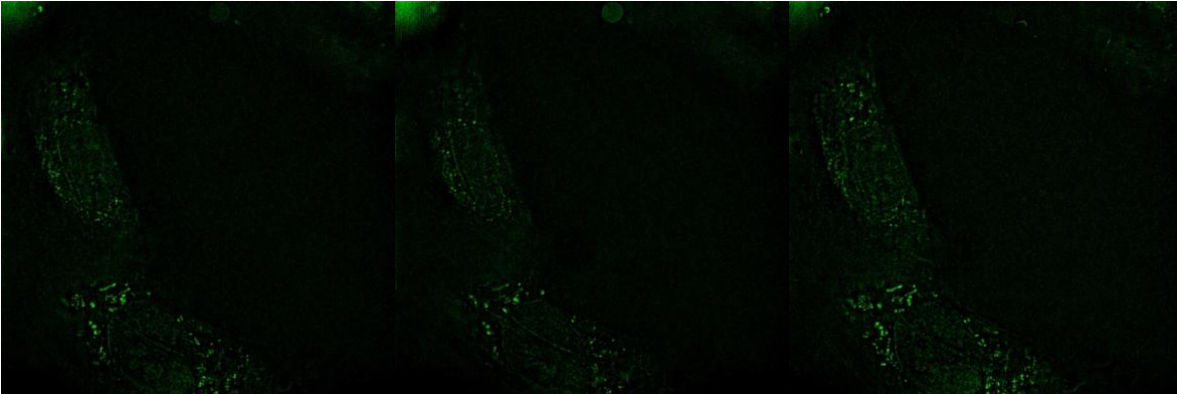

Figure 4.1: Images of 3 slices of two cells at minute 0 (a), minute 3 (b) and minute 5 (c) of a time-lapse acquisition, whereby the cells were electroporated with 800 V at 30 seconds.
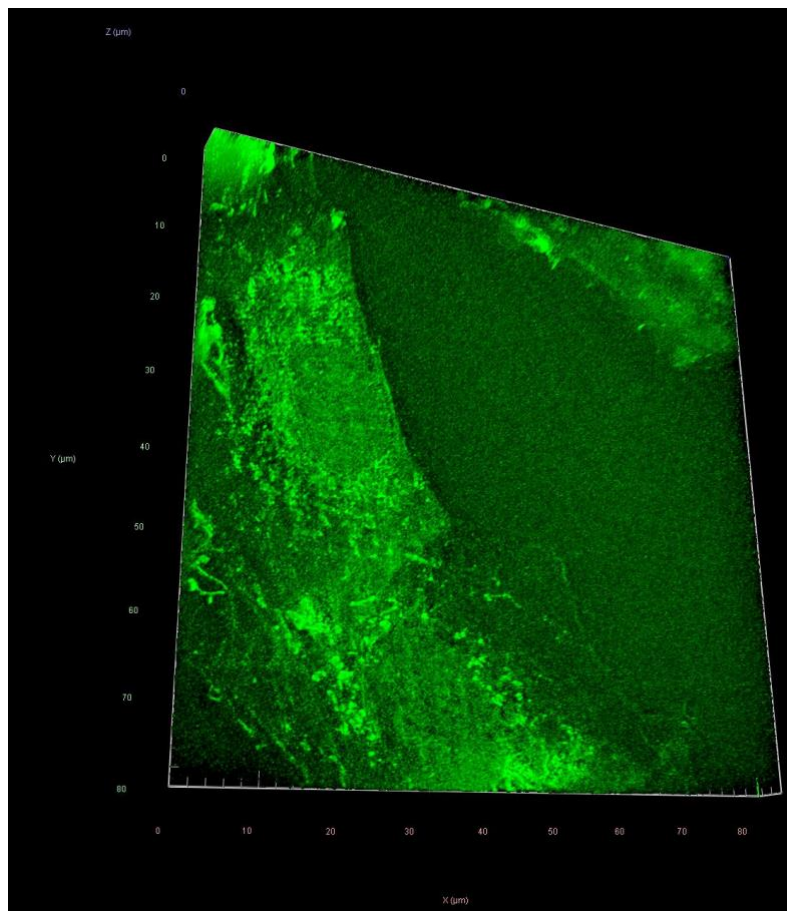

Figure 4.2: 3D acquisition of the cells in Figure 4.1

4.2 FUTURE EXPERIMENTAL DIRECTIONS

The information obtained from Zeiss super-resolution microscopy highlights several key points for future research and experimental refinement. Future experiments should focus on understanding the identity of the preexisting vesicles and discerning them from those that are formed anew as a consequence of electric pulse exposure. The preexisting vesicles might be intracellular organelles that have a high concentration of calcium. Calcein, also used in complexometric calcium titration, shows an increase in fluorescence in the presence of this ion [63]. Studies in literature confirm that calcium is a constant and fundamental component in mitochondria as well as endoplasmic reticulum [64]. This interaction suggests a connection between calcein and these organelles. Therefore, observations with super-resolution microscopic support the hypothesis that the resolved intracellular fluorescent structures were indeed mitochondria, endoplasmic reticulum and other calcium-containing intracellular structures which were stained with calcein along with the cytosol. During electroporation, the cell membrane permeabilizes, facilitating the emptying of calcein and making these vesicles increasingly visible.

Using high-resolution imaging techniques such as super-resolution microscopy can provide deeper insights into cellular responses and structural changes, suggesting a potential standard practice for future electroporation studies. Implementing z-axis analysis as a routine part of imaging can help to accurately characterize the three-dimensional organization of intracellular structures, leading to more robust and detailed data. Systematically studying variations in electroporation parameters (e.g. pulse duration and voltage) is crucial to understanding their effects on vesicle visibility and calcein efflux, providing a clearer picture of the electroporation mechanism.

The results of the experiment with the Zeiss super-resolution microscope underline the importance of using advanced imaging techniques to complement standard fluorescence microscopy. These approaches can significantly improve the understanding of cellular behavior and increase the accuracy and reliability of experimental results.

4.3. FUTURE DIRECTIONS FOR IMAGE ANALYSIS

Turning to the conclusions regarding the granulation analysis, they provide excellent backing to the discussions previously made when discussing fluorescence averaging and the detection of vesicles. The analyses and processing carried out using the algorithms on Cell Profiler have allowed us to gain a clearer picture of some of the details that had previously been overshadowed. The GS1 values showed significant consistency both in terms of absolute values and repeatability over several days of acquisition. This indicates that the analysis method adopted is effective to identify granularity. The repeatability of the results, especially for GS1, confirms the validity of the experimental protocol used. The data from GS1 and GS2 indicate that increasing the applied voltage leads to a gradual increase in granularity values.

This behavior suggests that high voltages facilitate the detection of vesicles, probably due to the accelerated release of calcein from the cells. The GS1 and GS2 values show a positive and linear trend over time, with a standard deviation within acceptable values, especially for the 200 V and 400 V voltages. Despite the low standard deviation, GS3 curves did not follow a clear trend and showed inconsistent and small variations over time. This suggests that GS3 may not be a reliable parameter to assess cell granularity in this specific context.

Nevertheless, granularity analysis using CellProfiler was difficult for a number of reasons. First, the insufficient documentation provided for the granularity analysis by CellProfiler made it hard to fully understand how the granularity spectrum is obtained and what it represents. This gave additional challenges to clearly explain the results. Despite a thorough search for what the GS1, GS2 and GS3 granularity spectra meaning, no clear interpretation could be found to the extent that their true meaning could be understood.

Aside from granularity analysis we also tried another approach, where we added various modules into the pipeline to recognize vesicles as secondary objects. However, we were unsuccessful in this approach; the analysis did not behave as expected, i.e. it did not identify all vesicles in the cells and did not determine their size and number. Therefore, further investments into developing the image processing approach should be made to better characterize and quantify the vesicles that are observed in the acquired images.

CHAPTER 5: CONCLUSIONS

This work explored the response of the cardiac cell line H9c2 to electroporation by exposing the cells to eight electric pulses of 100 μs duration and different voltages. The cells were stained with calcein dye and monitored under a fluorescence microscope. As expected, we observed that exposure to electric pulses of sufficient amplitude increases the permeability of the cell membranes due to electroporation, which can be observed through leak out of the calcein dye from the cells and the concomitant decrease of the cell fluorescence. The higher was the applied voltage, the more profound and faster was the decrease in cell fluorescence, indicating stronger electroporation.

An unexpected result was the appearance of bright vesicles in response to the pulse exposure. Analysis of the acquired images suggested that some of these vesicles form anew, probably as a stress response of the cells to electric pulse exposure. Additional experiments using a super-resolution microscope, however, demonstrated that some these vesicles were already present within the cells before the pulse application and became more evident due to the gradual depletion of calcein from the cell. These intracellular structures are most likely calcium-containing organelles including mitochondria and endoplasmic reticulum. Further studies are needed to identify the identity of both the newly formed and continuously present calcium-stained structures within the cells. For these studies, super-resolution microscopy is suggested.

Furthermore, it would be interesting to verify whether similar responses can be observed in primary cardiac muscle cells, which are a better model for cardiac tissue than H9c2 cell line. Such studies are important for understanding the mechanisms by which cardiac cells respond to electric pulses in evolving medical applications, including cardiac tissue ablation by irreversible electroporation for treatment of arrhythmias and gene therapy.

BIBLIOGRAPHY

[1] 'Cell Structure and Function', Biology LibreTexts. Accessed: Jun. 21, 2024. [Online]. Available: https://bio.libretexts.org/Learning_Objects/Worksheets/Biology_Tutorials/Cell_Structure_and_Function

[2] 'Cell | Definition, Types, Functions, Diagram, Division, Theory, & Facts | Britannica'. Accessed: Jun. 21, 2024. [Online]. Available: https://www.britannica.com/science/cell-biology

[3] B. Alberts, Ed., *Molecular biology of the cell. Hauptbd.*, 4. ed. New York: Garland, 2002.

[4] 'Britannica, The Editors of Encyclopaedia. "cell membrane". Encyclopedia Britannica, 10 May. 2024, https://www.britannica.com/science/cell-membrane. Accessed 26 June 2024.'

[5] M. Yang and W. J. Brackenbury, 'Membrane potential and cancer progression', *Front. Physiol.*, vol. 4, p. 185, 2013, doi: 10.3389/fphys.2013.00185.

[6] C. Brosseau and E. Sabri, 'Resistor–capacitor modeling of the cell membrane: A multiphysics analysis', *J. Appl. Phys.*, vol. 129, no. 1, p. 011101, Jan. 2021, doi: 10.1063/5.0033608.

[7] L. A. Dunbar and M. J. Caplan, 'Ion Pumps in Polarized Cells: Sorting and Regulation of the Na+,K+- and H+,K+-ATPases', *J. Biol. Chem.*, vol. 276, no. 32, pp. 29617–29620, Aug. 2001, doi: 10.1074/jbc.R100023200.

[8] L. A. Dunbar and M. J. Caplan, 'The cell biology of ion pumps: sorting and regulation', *Eur. J. Cell Biol.*, vol. 79, no. 8, pp. 557–563, Aug. 2000, doi: 10.1078/0171-9335-00079.

[9] P. Marszalek, D. S. Liu, and T. Y. Tsong, 'Schwan equation and transmembrane potential induced by alternating electric field', *Biophys. J.*, vol. 58, no. 4, pp. 1053–1058, Oct. 1990, doi: 10.1016/S0006-3495(90)82447-4.

[10] S. M. Chrysafides, S. J. Bordes, and S. Sharma, 'Physiology, Resting Potential', in *StatPearls*, Treasure Island (FL): StatPearls Publishing, 2024. Accessed: Jun. 26, 2024. [Online]. Available: http://www.ncbi.nlm.nih.gov/books/NBK538338/

[11] 'Membrane potential (resting membrane potential) (article) | Khan Academy."'.

[12] T. Kotnik, F. Bobanović, and D. Miklavčič, 'Sensitivity of transmembrane voltage induced by applied electric fields—A theoretical analysis', *Bioelectrochem. Bioenerg.*, vol. 43, no. 2, pp. 285–291, Aug. 1997, doi: 10.1016/S0302-4598(97)00023-8.

[13] 'https://www.cytion.com/CHO-K1-Cells/603480'.

[14] M. Hibino, M. Shigemori, H. Itoh, K. Nagayama, and K. Kinosita, 'Membrane conductance of an electroporated cell analyzed by submicrosecond imaging of transmembrane potential', *Biophys. J.*, vol. 59, no. 1, pp. 209–220, Jan. 1991, doi: 10.1016/S0006-3495(91)82212-3.

[15]   G. Pucihar, T. Kotnik, D. Miklavčič, and J. Teissié, 'Kinetics of Transmembrane Transport of Small Molecules into Electropermeabilized Cells', *Biophys. J.*, vol. 95, no. 6, pp. 2837–2848, Sep. 2008, doi: 10.1529/biophysj.108.135541.

[16]   T. Kotnik, L. Rems, M. Tarek, and D. Miklavčič, 'Membrane Electroporation and Electropermeabilization: Mechanisms and Models', *Annu. Rev. Biophys.*, vol. 48, no. 1, pp. 63–91, May 2019, doi: 10.1146/annurev-biophys-052118-115451.

[17]   J. C. Weaver and Yu. A. Chizmadzhev, 'Theory of electroporation: A review', *Bioelectrochem. Bioenerg.*, vol. 41, no. 2, pp. 135–160, Dec. 1996, doi: 10.1016/S0302-4598(96)05062-3.

[18]   A. Vižintin and D. Miklavčič, 'Elektropermeom: celični odgovor na elektroporacijo', *Slov. Med. J.*, pp. 1–13, Sep. 2022, doi: 10.6016/ZdravVestn.3267.

[19]   A. R. Deipolyi, A. Golberg, M. L. Yarmush, R. S. Arellano, and R. Oklu, 'Irreversible electroporation: the evolution of a laboratory technique to be used in interventional oncology', *Diagn. Interv. Radiol.*, Jan. 2014, doi: 10.5152/dir.2013.13304.

[20]   H. M. Noad, *Lectures on Electricity: Comprising Galvanism, Magnetism, Electro-Magnetism, Magneto- and Thermo-Electricity*, 1st ed. Cambridge University Press, 2012. doi: 10.1017/CBO9781139380584.

[21]   I. G. Abidor, L. H. Li, and S. W. Hui, 'Studies of cell pellets: II. Osmotic properties, electroporation, and related phenomena: membrane interactions', *Biophys. J.*, vol. 67, no. 1, pp. 427–435, Jul. 1994, doi: 10.1016/S0006-3495(94)80498-9.

[22]   R. Stampflj, 'Reversible electrical breakdown of the excitable membrane of a Ranvier node', *An. Acad. Bras. Cienc.*, vol. 30, no. 1, pp. 57–61, 1958.

[23]   A. Sale and W. Hamilton, 'Effects of high electric fields on microorganismsI. Killing of bacteria and yeasts', *Biochim. Biophys. Acta BBA - Gen. Subj.*, vol. 148, no. 3, pp. 781–788, Dec. 1967, doi: 10.1016/0304-4165(67)90052-9.

[24]   U. Zimmermann, G. Pilwat, and F. Riemann, 'Dielectric Breakdown of Cell Membranes', *Biophys. J.*, vol. 14, no. 11, pp. 881–899, Nov. 1974, doi: 10.1016/S0006-3495(74)85956-4.

[25]   E. Neumann, M. Schaefer-Ridder, Y. Wang, and P. H. Hofschneider, 'Gene transfer into mouse lyoma cells by electroporation in high electric fields.', *EMBO J.*, vol. 1, no. 7, pp. 841–845, Jul. 1982, doi: 10.1002/j.1460-2075.1982.tb01257.x.

[26]   T. Kotnik, W. Frey, M. Sack, S. Haberl Meglič, M. Peterka, and D. Miklavčič, 'Electroporation-based applications in biotechnology', *Trends Biotechnol.*, vol. 33, no. 8, pp. 480–488, Aug. 2015, doi: 10.1016/j.tibtech.2015.06.002.

[27]   B. Geboers *et al.*, 'High-Voltage Electrical Pulses in Oncology: Irreversible Electroporation, Electrochemotherapy, Gene Electrotransfer, Electrofusion, and Electroimmunotherapy', *Radiology*, vol. 295, no. 2, pp. 254–272, May 2020, doi: 10.1148/radiol.2020192190.

[28]   S. Sachdev, T. Potočnik, L. Rems, and D. Miklavčič, 'Revisiting the role of pulsed electric fields in overcoming the barriers to in vivo gene electrotransfer', *Bioelectrochemistry*, vol. 144, p. 107994, Apr. 2022, doi:

10.1016/j.bioelechem.2021.107994.

[29]   Y. Wang *et al.*, 'Transdermal microarrayed electroporation for enhanced cancer immunotherapy based on DNA vaccination', *Proc. Natl. Acad. Sci.*, vol. 121, no. 25, p. e2322264121, Jun. 2024, doi: 10.1073/pnas.2322264121.

[30]   A. Verma *et al.*, 'Pulsed Field Ablation for the Treatment of Atrial Fibrillation: PULSED AF Pivotal Trial', *Circulation*, vol. 147, no. 19, pp. 1422–1432, May 2023, doi: 10.1161/CIRCULATIONAHA.123.063988.

[31]   A. A. Bulysheva, B. Hargrave, N. Burcus, C. G. Lundberg, L. Murray, and R. Heller, 'Vascular endothelial growth factor-A gene electrotransfer promotes angiogenesis in a porcine model of cardiac ischemia', *Gene Ther.*, vol. 23, no. 8–9, pp. 649–656, Aug. 2016, doi: 10.1038/gt.2016.35.

[32]   M. K. Chung *et al.*, 'Atrial Fibrillation', *J. Am. Coll. Cardiol.*, vol. 75, no. 14, pp. 1689–1713, Apr. 2020, doi: 10.1016/j.jacc.2020.02.025.

[33]   J. G. Andrade *et al.*, 'Efficacy and safety of cryoballoon ablation for atrial fibrillation: A systematic review of published studies', *Heart Rhythm*, vol. 8, no. 9, pp. 1444–1451, Sep. 2011, doi: 10.1016/j.hrthm.2011.03.050.

[34]   D. W. Hunter, G. Kostecki, J. M. Fish, J. A. Jensen, and H. Tandri, 'In Vitro Cell Selectivity of Reversible and Irreversible: Electroporation in Cardiac Tissue', *Circ. Arrhythm. Electrophysiol.*, vol. 14, no. 4, Apr. 2021, doi: 10.1161/CIRCEP.120.008817.

[35]   O. Tovar and L. Tung, 'Electroporation and recovery of cardiac cell membrane with rectangular voltage pulses', *Am. J. Physiol.-Heart Circ. Physiol.*, vol. 263, no. 4, pp. H1128–H1136, Oct. 1992, doi: 10.1152/ajpheart.1992.263.4.H1128.

[36]   J. Koruth *et al.*, 'Preclinical Evaluation of Pulsed Field Ablation: Electrophysiological and Histological Assessment of Thoracic Vein Isolation', *Circ. Arrhythm. Electrophysiol.*, vol. 12, no. 12, p. e007781, Dec. 2019, doi: 10.1161/CIRCEP.119.007781.

[37]   S. Chaigne *et al.*, 'Reversible and Irreversible Effects of Electroporation on Contractility and Calcium Homeostasis in Isolated Cardiac Ventricular Myocytes', *Circ. Arrhythm. Electrophysiol.*, vol. 15, no. 11, Nov. 2022, doi: 10.1161/CIRCEP.122.011131.

[38]   R. M. Blaese *et al.*, 'T Lymphocyte-Directed Gene Therapy for ADA ⁻ SCID: Initial Trial Results After 4 Years', *Science*, vol. 270, no. 5235, pp. 475–480, Oct. 1995, doi: 10.1126/science.270.5235.475.

[39]   C.-X. He, Y. Tabata, and J.-Q. Gao, 'Non-viral gene delivery carrier and its three-dimensional transfection system', *Int. J. Pharm.*, vol. 386, no. 1–2, pp. 232–242, Feb. 2010, doi: 10.1016/j.ijpharm.2009.11.006.

[40]   M. R. Prausnitz, J. A. Mikszta, M. Cormier, and A. K. Andrianov, 'Microneedle-Based Vaccines', in *Vaccines for Pandemic Influenza*, vol. 333, R. W. Compans and W. A. Orenstein, Eds., in Current Topics in Microbiology and Immunology, vol. 333. , Berlin, Heidelberg: Springer Berlin Heidelberg, 2009, pp. 369–393. doi: 10.1007/978-3-540-92165-3_18.

[41] P. E. Huber, J. Jenne, J. Debus, M. F. Wannenmacher, and P. Pfisterer, 'A comparison of shock wave and sinusoidal-focused ultrasound-induced localized transfection of HeLa cells', *Ultrasound Med. Biol.*, vol. 25, no. 9, pp. 1451–1457, Nov. 1999, doi: 10.1016/S0301-5629(99)00099-X.

[42] S. Nimesh, S. Halappanavar, N. K. Kaushik, and P. Kumar, 'Advances in Gene Delivery Systems', *BioMed Res. Int.*, vol. 2015, pp. 1–2, 2015, doi: 10.1155/2015/610342.

[43] P. Singh *et al.*, 'Transdermal delivery for gene therapy', *Drug Deliv. Transl. Res.*, vol. 12, no. 11, pp. 2613–2633, Nov. 2022, doi: 10.1007/s13346-022-01138-1.

[44] N. Sayed *et al.*, 'Gene therapy: Comprehensive overview and therapeutic applications', *Life Sci.*, vol. 294, p. 120375, Apr. 2022, doi: 10.1016/j.lfs.2022.120375.

[45] S. Pagant and R. A. Liberatore, 'In Vivo Electroporation of Plasmid DNA: A Promising Strategy for Rapid, Inexpensive, and Flexible Delivery of Anti-Viral Monoclonal Antibodies', *Pharmaceutics*, vol. 13, no. 11, p. 1882, Nov. 2021, doi: 10.3390/pharmaceutics13111882.

[46]
    'https://clinicaltrials.gov/ct2/results?cond=&term=electroporation+DNA+&cntry=&state=&city=&dist='.

[47] C. Boye *et al.*, 'Cardioporation enhances myocardial gene expression in rat heart', *Bioelectrochemistry*, vol. 142, p. 107892, Dec. 2021, doi: 10.1016/j.bioelechem.2021.107892.

[48] B. Hargrave *et al.*, 'Electroporation-mediated gene transfer directly to the swine heart', *Gene Ther.*, vol. 20, no. 2, pp. 151–157, Feb. 2013, doi: 10.1038/gt.2012.15.

[49] A. A. Bulysheva, N. Burcus, C. G. Lundberg, M. P. Francis, and R. Heller, 'VEGF-B electrotransfer mediated gene therapy induces cardiomyogenesis in a rat model of cardiac ischemia', *Bioelectrochemistry*, vol. 124, pp. 105–111, Dec. 2018, doi: 10.1016/j.bioelechem.2018.07.007.

[50] C. Boye *et al.*, 'Reduction of plasmid vector backbone length enhances reporter gene expression', *Bioelectrochemistry*, vol. 144, p. 107981, Apr. 2022, doi: 10.1016/j.bioelechem.2021.107981.

[51] T. Batista Napotnik and D. Miklavčič, 'Pulse Duration Dependent Asymmetry in Molecular Transmembrane Transport Due to Electroporation in H9c2 Rat Cardiac Myoblast Cells In Vitro', *Molecules*, vol. 26, no. 21, p. 6571, Oct. 2021, doi: 10.3390/molecules26216571.

[52] S. J. Watkins, G. M. Borthwick, and H. M. Arthur, 'The H9C2 cell line and primary neonatal cardiomyocyte cells show similar hypertrophic responses in vitro', *Vitro Cell. Dev. Biol. - Anim.*, vol. 47, no. 2, pp. 125–131, Feb. 2011, doi: 10.1007/s11626-010-9368-1.

[53] T. Batista Napotnik and D. Miklavčič, 'In vitro electroporation detection methods - An overview', *Bioelectrochemistry Amst. Neth.*, vol. 120, pp. 166–182, Apr. 2018, doi: 10.1016/j.bioelechem.2017.12.005.

[54] F. Miles, J. Lynch, and R. Sikes, 'Cell-based assays using calcein acetoxymethyl ester show variation in fluorescence with treatment conditions', *J. Biol. Methods*, vol. 2, no. 3, p. e29, Oct. 2015, doi: 10.14440/jbm.2015.73.

[55] 'https://pubchem.ncbi.nlm.nih.gov/compound/Calcein'.

[56] 'https://www.leica-microsystems.com/products/thunder-imaging-systems/'.

[57] 'https://lbk.fe.uni-lj.si/ic/wp-content/uploads/2018/03/ELECTROcell-B10-HV-LV-EN.pdf'.

[58] 'https://www.broadinstitute.org/blog/cellprofiler%E2%80%99s-identifying-features'.

[59] J. Schindelin *et al.*, 'Fiji: an open-source platform for biological-image analysis', *Nat. Methods*, vol. 9, no. 7, pp. 676–682, Jul. 2012, doi: 10.1038/nmeth.2019.

[60] C. A. Schneider, W. S. Rasband, and K. W. Eliceiri, 'NIH Image to ImageJ: 25 years of image analysis', *Nat. Methods*, vol. 9, no. 7, pp. 671–675, Jul. 2012, doi: 10.1038/nmeth.2089.

[61] P.-C. Chiang, K. Tanady, L.-T. Huang, and L. Chao, 'Rupturing Giant Plasma Membrane Vesicles to Form Micron-sized Supported Cell Plasma Membranes with Native Transmembrane Proteins', *Sci. Rep.*, vol. 7, no. 1, p. 15139, Nov. 2017, doi: 10.1038/s41598-017-15103-3.

[62] J. Sudnitsyna, E. Skverchinskaya, I. Dobrylko, E. Nikitina, S. Gambaryan, and I. Mindukshev, 'Microvesicle Formation Induced by Oxidative Stress in Human Erythrocytes', *Antioxidants*, vol. 9, no. 10, p. 929, Sep. 2020, doi: 10.3390/antiox9100929.

[63] F. Hausig-Punke, F. Richter, M. Hoernke, J. C. Brendel, and A. Traeger, 'Tracking the Endosomal Escape: A Closer Look at Calcein and Related Reporters', *Macromol. Biosci.*, vol. 22, no. 10, p. 2200167, Oct. 2022, doi: 10.1002/mabi.202200167.

[64] D. G. Nicholls, 'Mitochondria and calcium signaling', *Cell Calcium*, vol. 38, no. 3–4, pp. 311–317, Sep. 2005, doi: 10.1016/j.ceca.2005.06.011.

[65] T. Y. Tsong, 'Electroporation of cell membranes', *Biophys. J.*, vol. 60, no. 2, pp. 297–306, Aug. 1991, doi: 10.1016/S0006-3495(91)82054-9.